Investigation of the Geometric Effects of Corrosion Pits on the Tensile Behaviour of Structural Steel

A thesis

submitted in fulfilment

of the requirements for the degree

of

Master of Engineering with endorsement in Civil Engineering

at

The University of Waikato

by

Kaung Myat Thu

THE UNIVERSITY OF

WAIKATO

Te Whare Wānanga o Waikato

Submission: July 2026

Abstract

Pitting corrosion removes parts of the structural steel's cross section in a localised manner, therefore introducing localised stress concentrations which can cause decreased tensile and deformation capacity in a more pronounced effect than uniform cross sectional mass loss.

With aging infrastructures using structural steel used in chloride environments, there is a growing need for reliable assessment of corroded steel. Therefore, a methodology that can provide insights with the linkage of measurable corrosion parameter such as mass loss to mechanical response of the corroded steel material can prove to be a clear contribution for corrosion analysis. The methodology should also consider the localised and stochastic nature of pit formations. This thesis develops and applies a reproducible numerical workflow for this purpose and evaluates it against an experimental tensile programme on low-carbon structural steel coupons immersed in a 5% sodium-chloride solution for up to 42 days.

Flat dog-bone coupons conforming to ISO 6892-1 were corroded for 0, 14, 21, 28, 35 and 42 days, cleaned and weighed gravimetrically, and tested in uniaxial tension. The coupons were protection wrapped for the grip and shoulder regions and only the gauge section were exposed to the chloride immersion. Measured average effective mass losses ranged from 1.29% to 2.49%, with a power-law mass-loss-time relationship indicative of a diffusion-controlled process.

Finite element analyses were conducted with a stochastic pit-generation algorithm developed in MATLAB which was used to create randomised distributions of flat-bottomed cylindrical pits, with the total pit volume matched to the measured mass loss. The resulting pit fields were then converted into discrete cavities in an Abaqus/Explicit coupon model using a Python script that conducts automated pit insertion through reading the MATLAB pit generation output data. The material model was calibrated once using a representative lab-tested experimental uncorroded Day-0 tensile response and was subsequently kept unchanged, thereby isolating the simulated influence of corrosion to geometrical material loss. This calibrated geometry-isolated workflow was subsequently applied to a numerical mass-loss projection study, extending the corrosion severity beyond the experimental range to 12% gauge-section mass loss. At this higher severity,

the ultimate tensile strength showed a more pronounced decrease compared to lower mass-loss levels, while the ductility loss obtained from the FE simulations remained strongly influenced by the pit geometry and spatial distribution of each stochastic realisation.

The uncorroded finite-element model reproduced the experimental ultimate tensile strength to within approximately 0.4% and was shown to be mesh-converged and quasi-static through an energy-balance study. Across the corroded cases, the experimental coupons showed no statistically clear monotonic reduction in either ultimate strength or fracture strain at the studied mass-loss levels. It was observed that the corrosion-induced change was smaller than the coupon-to-coupon scatter. On the other hand, geometry-isolated finite-element model, resolved a small reduction in ultimate strength (of order 2% over the exposure range) and a substantially larger reduction in fracture strain and toughness (of order 7-14%). This suggests that ductility is the corrosion-sensitive quantity and that strain localisation at pits are key factors of the loss of deformation capacity. Based on these findings, simple normalised predictive relationships are proposed in which the residual strength, fracture-strain and toughness factors decrease approximately linearly with mass loss, the ductility coefficient being about an order of magnitude larger than the strength coefficient. These relationships come with limitations which are discussed in the later section.

The principal contribution of the thesis is a single, seed-controlled, mass-loss-verified workflow combining stochastic pit generation, idealised-pit finite-element realisation and quasi-static tensile simulation, together with a quantified experimental demonstration which shows that at low-to-moderate mass loss, the geometric effect of pitting on steel coupons is concentrated in ductility rather than strength. The cylindrical pit idealisation, the fixed material card and the coupon scale are acknowledged as part of the limitations of this study.

Acknowledgements

I would like to sincerely thank my supervisor, Dr. Arthur Fang, for his guidance, critical feedback and encouragement throughout this project, as well as the support from Kimi Wang.

Special thanks to Avitesh Singh also for the usage of his experimental test results.

Table of Contents

Nomenclature and Abbreviations

The principal symbols and abbreviations used in this thesis are listed below.

Symbol / abbreviation	**Meaning**
FE / FEA	Finite element / finite-element analysis
F	Tensile force
RF_2	Abaqus reaction force in the axial loading direction
U_2	Abaqus displacement output in the axial loading direction; denoted as ΔL_{FE} during post-processing to avoid confusion with toughness U
ΔL	Axial elongation / displacement of the gauge length
ΔL_f	Axial elongation at fracture
ΔL_{FE}	Axial elongation extracted from the FE model
L_0	Original gauge length used for engineering strain calculation
L, W, t	Gauge length, gauge width and coupon thickness
A_0	Original cross-sectional area of the gauge section
σ	Engineering stress
σ_{true}	True stress
σ_{FE}	Engineering stress calculated from FE reaction force
f_u / UTS	Ultimate tensile strength
f_y	Yield stress
ε	Engineering strain
ε_{true}	True strain
ε_f	Fracture strain, defined as engineering strain at fracture / failure

Symbol / abbreviation	**Meaning**
ε_{UTS}	Engineering strain at ultimate tensile strength
U	Tensile toughness, calculated as the area under the engineering stress-strain curve up to fracture, reported in MJ/m^3
Δm	Absolute mass loss, usually in grams
Δm (%)	Percentage mass loss relative to the uncorroded mass
M_0	Initial uncorroded specimen mass
m_1	Final corroded and cleaned specimen mass
ρ	Material density
V_{target} or V_{loss}	Target equivalent volume of steel removed to represent a prescribed mass-loss level
V_{pit}	Volume removed by a single pit
r	Pit radius
h	Pit depth
h/t or d/t	Pit depth-to-thickness ratio; h/t is preferred when h is used as the pit-depth symbol
C3D10	Second-order quadratic tetrahedral element
C3D10M	Modified second-order tetrahedral element
C3D8	Linear hexahedral element
ALLIE	Internal energy in Abaqus
ALLKE	Kinetic energy in Abaqus
ALLAE	Artificial strain energy in Abaqus
ETOTAL	Total energy in Abaqus

Symbol / abbreviation	**Meaning**
DMASS	Added mass fraction due to mass scaling in Abaqus
R_{σ}	Residual strength factor
R_{ε}	Residual fracture-strain factor
R_{U}	Residual toughness factor
$\bar{x}$	Mean value of a group of specimens or FE realisations
s	Sample standard deviation used to quantify scatter
n	Number of specimens or FE realisations in a group
$S_{a,eq}$	Area-weighted average pit depression over the gauge surface
$S_{q,eq}$	Root-mean-square pit depression over the gauge surface

1. Introduction

1.1 Background

Steel is widely used as a structural component for bridges, offshore and coastal structures, underwater pipelines, where they are exposed to environments with chloride contents present. In such environments, the steel typically breaks down as localised corrosion rather than uniform thinning of section and form pits across the surface that grow and coalesce on the exposed surface.

Pitting is more detrimental than uniform thinning of the steel. Each pit induces a localized reduction of load-bearing area and acts as the point of stress concentration in the steel. This leading to the concentration of strain, early necking, and lower deformation capacity, even with minimal overall mass loss [2], [14], [15]. Ductility and toughness dictate a structure's capacity to redistribute load and signal distress prior to fracture; thus, corrosion that diminishes deformation capacity poses both a safety and serviceability concern.

Important engineering parameters such as tensile strength, ductility, toughness determines the structural capacity of the steel before fracturing. Localised corrosion heavily impacts them thus it is a concern of safety and serviceability with prolonged exposure periods.

As the infrastructure ages, there is a growing need for routine engineering assessments and maintenance. Thus, the quantitative assessment of corroded steel is vital. Engineering asset managers must make professional judgment to determine the structural integrity of the corroded steel components and determine the necessary interventions. These decisions rest on a relationship between an inspectable measure of corrosion damage, most commonly mass loss, sometimes supplemented by pit-depth or pit-density measurements, and the residual mechanical properties of the steel. Establishing such a relationship and doing so in a way that reflects how pitting realistically degrades steel, is the broad motivation for this work.

For the present thesis, this distinction is important because the measured experimental mass losses are low. At low mass loss, the remaining cross-section can still carry a load close to that of the uncorroded coupon, while local pits can still influence where plastic strain starts to concentrate. The numerical model is therefore used to study the geometric mechanism of pitting, rather than to force a large strength reduction that is not supported by the experimental data.

The use of a reproducible finite element workflow also responds to a practical limitation in corrosion assessment. Field inspection commonly provides global indicators such as mass loss, thickness reduction or visual pitting severity, but the tensile response depends on local features such as pit depth, pit spacing and the location of the most severe section. A model that links mass loss to a controlled pit population is therefore useful because it connects a measurable corrosion descriptor with a local damage mechanism.

1.2 Problem Statement

There are two common methods of simplifying the assessment of corroded steel. Each of the two methods have their own set of limitations. The first method represents corrosion as a uniform reduction of thickness and applies an empirical knockdown to the nominal capacity. It is a convenient method, but it is unable to capture the local stress concentration that pitting introduces, and it implicitly assumes that the only effect of corrosion is to reduce area.

The other method represents corrosion by a single idealised defect of fixed size and shape. This captures stress concentration but not the spatial randomness of real corrosion, in which many pits of varying size and depth are distributed irregularly over the surface.

The implication of the two simplification methods is that it is unable to capture that two members with identical mass loss may behave differently if their pits differ in depth, size, density or arrangement, and a deterministic, uniform or single-pit model cannot represent that variability [1], [16], [17].

There is therefore a need for an assessment method that (i) represents corrosion as a population of discrete, randomly distributed pits rather than as a uniform loss or a single defect, ties the generated geometry quantitatively to a measurable corrosion descriptor such as mass loss, is reproducible, so that a given corrosion condition can be regenerated and re-analysed, and is calibrated against experiment.

This thesis study provides some insights into this need with a numerical workflow that generates stochastic pit fields controlled by a designated mass loss quantity. It is then carried out through pit insertion in Abaqus of a tensile coupon and realised as a stochastically pitted corrosion models. An experimental corrosion study is also carried out up to 42 days of corrosion exposure in immersed chloride environment.

1.3 Aim and Objectives

The aim of this thesis is to develop a reproducible numerical workflow for representing pitting corrosion in structural-steel tensile coupons, and to use it to quantify how mass loss and pit morphology affect tensile capacity and ductility. The specific objectives are:

(1) to develop a reproducible, seed-controlled stochastic pit-generation workflow whose generated mass loss can be verified against measurement;

(2) to build a three-dimensional explicit finite-element tensile model and verify its numerical quality through mesh-convergence and quasi-static (energy-balance) checks;

(3) to calibrate the material model once against the uncorroded (Day 0) tensile response and the workflow against the corroded coupon data from Day 14 to Day 42;

(4) to quantify, in a controlled numerical setting in which only geometry changes, the influence of mass loss and pit morphology on ultimate strength, fracture strain and toughness; and

(5) to propose simple, predictive relationships linking residual mechanical properties to mass loss, with stated fit quality and range of validity.

1.4 Scope and Limitations

The corrosion morphology is idealised in each pit is modelled as a flat-bottomed right circular cylinder. Conical pits were also explored, but they proved numerically far less robust. The sharp conical apex produced severe local element distortion, and of the conical simulations attempted across the exposure schedule only a single case ran to completion. Conical pits were therefore excluded from the production workflow in favour of the more robust and reproducible cylindrical idealisation. The cylindrical pit is treated throughout as an idealisation that is convenient and reproducible. It is important to note that it is not as a faithful reproduction of natural pit shape, and the simplification is acknowledged as a limitation.

In the experimental setup, only the gauge section was exposed on all surfaces. The shoulder and clamping regions were tape wrapped with a waterproofing tape to prevent any ion exchanges occurring on these surfaces. The experiments allowed corrosion to develop on all exposed gauge-section surfaces. The mass loss measured after the usage of rust remover accounts for the mass loss on all surfaces of the exposed gauge sections. However, the FE model idealised the corrosion as stochastic pits mainly on one gauge surface. This difference is treated as a modelling simplification, and the numerical results are interpreted as a controlled geometry-isolated representation of localised pitting rather than a direct reconstruction of the experimental corrosion morphology. The numerical component of the study idealises corrosion pits on one main surface and pits are generated as volume loss in correspondence to designated mass loss to represent selected mass-loss levels. Therefore, the FE results are interpreted as a controlled investigation of corrosion severity and localised pitting effects purely based on geometrical effects.

Additionally, the cylindrical pit idealisation may affect the simulated strain localisation. The flat base and sharp rim can produce stronger local stress and strain concentrations than smoother rounded pits. However, real corrosion pits may also contain irregular sharp features that are not captured by the idealised geometry. Thus, it is more prudent to interpret the results derived from a controlled cylindrical-pit representation as opposed to a naturally occurring corrosion pit morphology.

Another limitation of the FE modelling approach is that corrosion was represented only through geometric material loss. Any changes in the steel surface condition, microstructure, local ductility, corrosion-product effects or corrosion-induced material degradation were not considered. Thus, it should also not be considered as a complete corrosion material degradation model.

A single steel grade and a single coupon geometry are considered; the analysis is at coupon scale rather than member scale; and loading is quasi-static and monotonic. The material model is calibrated once and held constant across all corrosion stages, so that the simulated corrosion effect is purely geometric. The modelled corrosion range is also extended beyond the experimental severities through a numerical projection study, which carries the same geometry-isolated workflow up to 12% gauge-section mass loss.

1.5 Thesis Structure

Chapter 2 reviews pitting corrosion of steel, its effect on tensile behaviour, and the modelling approaches available, and states the research gap.

Chapter 3 sets out the experimental programme: the material and specimen geometry, the accelerated-corrosion exposure procedure, and the tensile-testing procedure.

Chapter 4 reports the test results and discussion: the measured mass loss and pit characterisation, the tensile response, the corrosion kinetics, and the scatter in the measured data.

Chapter 5 presents the numerical analysis: it sets out the finite-element methodology (the MATLAB pit-generation workflow, the mass-loss basis, the geometry and material model, the element and mesh selection, the loading and boundary conditions, and the quasi-static verification), then validates the workflow against the experimental data and interprets the simulations as a parametric study of mass loss and morphology.

Chapter 6 derives the proposed predictive relationships.

Chapter 7 discusses the results and their limitations.

Chapter 8 states the conclusions and outlines future work.

1.6 Contribution and Novelty of Study

The novelty of this thesis is methodological rather than material. It does not present a new corrosion environment or a new constitutive law but instead, it assembles a set of individually established techniques.

The individual parts include stochastic pit generation with idealised pit finite-element realisation that is mass-loss-controlled to produce a randomised pit fields for insertion into a corrosion tensile coupon model. It is then subjected to a quasi-static explicit tensile simulation which has a seed-control for reproducibility and mass-loss verified. This workflow demonstrates what various stochastic pitting scenarios produce varying tensile behaviour of pitted structural steel at different corrosion levels and geometrical effects. The contribution is therefore best stated as a capability together with a quantified finding.

The pipeline begins by converting a measured mass loss into a target volume of removed material. A pit population, randomised yet constrained by defined rules, is then generated to reproduce this volume. Each realisation's achieved mass loss is subsequently recorded and audited against the intended target, after which the population undergoes automated sectioning and analysis. Given that every realisation is tied to a specific seed, the corresponding corrosion condition can be reproduced exactly on demand.

This process responds to a gap identified within the screened literature. Although the individual elements comprising this pipeline are well established [1]–[6], they are typically reported as isolated procedures rather than as an integrated whole. Consequently, the relationship between generated geometry and a measured severity is frequently taken for granted, with verification rarely provided.

The quantified finding shows that, at the severities examined, the geometric influence of pitting concentrates primarily on ductility rather than on strength. This differential sensitivity as such can be expressed through simple residual property relationships anchored physically in mass loss. The workflow yields provisional predictive expressions for residual strength, fracture strain and toughness, which should allow an engineer to have an estimate for the mechanical behaviour of corroded steel from a known mass loss.

As the results indicate, the ductility coefficient is approximately an order of magnitude larger than the strength coefficient, a finding that suggests ductility responds more sensitively to pitting corrosion than tensile strength does. These relationships are presented as an initial and transparent modelling outcome rather than a finalised one. Their coefficients should therefore be re-fitted and calibrated against additional steel grades and independent datasets before broader application, in keeping with the requirement that any proposed predictive model be demonstrated beyond a single material grade.

1.7 List of Formulas Used

The percentage mass loss of each specimen was calculated as:

$$\Delta m(\%) = \frac{m_0 - m_c}{m_0} \times 100 \tag{1.1}$$

where m_0 is the initial mass before corrosion exposure, m_c is the mass after corrosion exposure, and Δm is the percentage mass loss. This value was used to quantify the corrosion severity of each specimen.

For the FE models, the prescribed mass loss was converted into an equivalent removed volume using:

$$V_{\text{loss}} = \frac{\Delta m}{\rho} \tag{1.2}$$

where V_{loss} is the equivalent volume of removed steel, Δm is the target mass loss in grams, and ρ is the density of steel. This allowed the numerical corrosion severity to be controlled through the total removed material volume.

Engineering stress

Engineering stress was calculated using the tensile force divided by the original cross-sectional area of the reduced gauge section:

$$\sigma = \frac{F}{A_0} \tag{1.3}$$

where σ is the engineering stress, F is the tensile force, and A_0 is the original cross-sectional area.

For the FE results, the reaction force extracted from Abaqus was converted into engineering stress using the same original area:

$$\sigma_{\mathrm{FE}} = \frac{RF}{A_0} \tag{1.4}$$

where RF is the reaction force obtained from the FE model.

Engineering strain

Engineering strain was calculated from the axial elongation divided by the original gauge length:

$$\varepsilon = \frac{\Delta L}{L_0} \tag{1.5}$$

where ε is the engineering strain, ΔL is the axial elongation, and L_0 is the original gauge length.

For the FE results, the corresponding engineering strain was calculated as:

$$\varepsilon_{\mathrm{FE}} = \frac{\Delta L_{\mathrm{FE}}}{L_0} \tag{1.6}$$

where ΔL_{FE} is the axial elongation extracted from the FE model. Although Abaqus reports displacement using the notation U, the symbol ΔL is used in this thesis to avoid confusion with the toughness symbol U.

Fracture strain

The fracture strain was taken as the engineering strain at the final extracted fracture point:

$$\varepsilon_f = \frac{\Delta L_f}{L_0} \tag{1.7}$$

where ε_f is the engineering fracture strain and ΔL_f is the axial elongation at fracture.

Ultimate tensile strength

The ultimate tensile strength was taken as the maximum engineering stress reached during the tensile response:

$$\sigma_{\mathrm{UTS}} = \max(\sigma) \tag{1.8}$$

where σ_{UTS} is the ultimate tensile strength and σ is the engineering stress throughout the loading history.

Engineering-to-true stress and strain conversion

For tensile data, the engineering stress and engineering strain can be converted to true stress and true strain using:

$$\sigma_{\mathrm{true}} = \sigma(1 + \varepsilon) \tag{1.9}$$

$$\varepsilon_{\mathrm{true}} = \ln(1 + \varepsilon) \tag{1.10}$$

where σ_{true} is the true stress, $\varepsilon_{\mathrm{true}}$ is the true strain, σ is the engineering stress, and ε is the engineering strain.

Tensile toughness

Tensile toughness was calculated as the area under the engineering stress–strain curve up to fracture:

$$U = \int_0^{\varepsilon_f} \sigma \, d\varepsilon \qquad (1.11)$$

where U is the tensile toughness, σ is the engineering stress, and ε_f is the fracture strain.

Since the stress–strain data were obtained as discrete points, the toughness was evaluated numerically using the trapezoidal rule:

$$U \approx \sum_{i=1}^{n-1} \frac{\sigma_i + \sigma_{i+1}}{2} (\varepsilon_{i+1} - \varepsilon_i) \qquad (1.12)$$

where σ_i and σ_{i+1} are two consecutive stress values, ε_i and ε_{i+1} are the corresponding strain values, and n is the total number of data points.

Because strain is dimensionless and stress is expressed in MPa, the integrated area is numerically equivalent to:

$$1 \text{ MPa} = 1 \text{ MJ/m}^3$$

Therefore, the tensile toughness values were reported in MJ/m^3.

Mean value

For each exposure group or FE simulation group, the mean value was calculated as:

$$\bar{x} = \frac{1}{n} \sum_{i=1}^{n} x_i \qquad (1.13)$$

where $\bar{x}$ is the group mean, x_i is an individual result from one specimen or numerical realisation, and n is the number of specimens or realisations in the group.

This was applied to quantities such as mass loss, ultimate tensile strength, fracture strain, and tensile toughness.

Standard deviation and scatter

The scatter within each group was quantified using the sample standard deviation:

$$s = \sqrt{\frac{\sum_{i=1}^{n}(x_i - \bar{x})^2}{n-1}} \tag{1.14}$$

where s is the sample standard deviation, x_i is an individual value, $\bar{x}$ is the group mean, and n is the number of specimens or simulations.

The results were reported in the form:

$$\bar{x} \pm s$$

This format was used to show both the average response and the variability within each exposure or simulation group.

In addition to pit depth, pit density and pit-area ratio, two equivalent roughness-type indicators were calculated from the idealised FE pit field. These parameters were not obtained from direct surface roughness measurements, such as profilometry or laser scanning. Instead, they were derived from the generated cylindrical pit geometry to provide additional descriptors of the average and root-mean-square surface depression caused by the pits.

For each generated pit, the projected pit area is:

$$A_i = \pi r_i^2 \tag{1.15}$$

where A_i is the projected area of pit i, and r_i is the pit radius.

The equivalent arithmetic mean surface depression is defined as:

$$S_{a,eq} = \frac{\sum_{i=1}^{n} A_i \, h_i}{A_{\text{surface}}} \tag{1.16}$$

where h_i is the depth of pit i, n is the total number of pits, and A_{surface} is the reference gauge surface area. The parameter $S_{a,eq}$ represents the area-weighted average pit depression over the gauge surface.

The equivalent root-mean-square surface depression is defined as:

$$S_{q,eq} = \sqrt{\frac{\sum_{i=1}^{n} A_i \, h_i^2}{A_{\text{surface}}}} \tag{1.17}$$

Compared with $S_{a,eq}$, $S_{q,eq}$ gives greater weighting to deeper pits and is therefore more sensitive to severe localised pitting.

These equivalent roughness-type indicators were used only as FE-derived morphology descriptors. They should not be interpreted as measured surface roughness values, but as post-processed quantities calculated from the idealised cylindrical pit population.

2. Literature Review

2.1 Pitting Corrosion and its Morphology

Pitting represents a localised form of corrosion whereby material loss becomes concentrated at discrete areas of the steel surface rather than being distributed evenly across it. Chloride ions present in environments such as seawater or the 5% sodium-chloride solution employed in this study promote this localised attack. Consequently, corrosion pits develop at discrete local sites and, over time, may deepen, widen and coalesce, giving rise to an irregular surface topography.

Several measurable parameters allow pitting to be described for engineering assessment purposes, including overall mass loss, equivalent average thickness loss, pit depth, pit diameter or width, pit density and pitting factor.

Standard guidance for examining and evaluating pitting corrosion, including the measurement and reporting of pit characteristics, is provided by ASTM G46 [22]. Descriptors consistent with this type of assessment have also been applied through automated techniques such as micro-computed tomography, which has been used to quantify pit density, size and depth on tensile specimens [23].

Previous surface-morphology studies have shown that pit depth and pit aspect ratio are statistically distributed rather than uniform [1], [20]. Depending on the material, environment and corrosion severity, pit-depth data have been represented using distributions such as normal, lognormal, Weibull, Fréchet and Gumbel forms [1], [4], [20], [21]. For this reason, the present study treats pitting corrosion as a stochastic morphology rather than as uniform thickness loss, and the generated pit fields are checked through radius, depth and aspect-ratio distributions.

Marine and chloride environments are relevant to this study because chloride ions can promote localised corrosion on steel surfaces.

Long-term corrosion studies also show that corrosion rate is not usually constant with time. As corrosion products accumulate on the steel surface, they can reduce the transport of oxygen and ions to the steel surface. This is consistent with the power-law trend used in this thesis to describe the immersion results. The purpose of the short laboratory exposure is not to reproduce decades of field exposure exactly. Instead, it provides a controlled chloride corrosion condition that produces measurable mass loss and surface damage for numerical modelling.

Several studies [1]-[6] on corroded structural steel also show that surface morphology provides useful information beyond mass loss alone.

2.2 Effect of Corrosion on Tensile Behaviour of Steel

Pitting affects the tensile behaviour of steel in two main ways. It removes load-bearing area, and it creates local stress and strain concentration. Experimental and numerical studies on steel plates with artificial pits show that pit depth and pit diameter influence the elastic stress concentration factor and the loss of deformation capacity. These studies also show that pits located near an edge can produce more severe stress concentration than pits located away from the edge [14]. Therefore, the effect of pitting cannot be explained by area loss alone.

This point is important for the present study because localised corrosion can be more damaging than uniform corrosion at the same mass-loss ratio. When material loss is concentrated in pits, the local stress increases around the damaged region and failure may occur earlier or more suddenly [15]. The mass-loss ratio is therefore useful as an average corrosion measure, but it does not fully describe the effect of pit depth, pit size, pit spacing and pit arrangement. Two specimens with the same mass loss may still show different tensile behaviour if their pit morphology is different [16].

Previous studies also show that corrosion affects ductility more strongly than strength. Refined finite-element models of corroded steel have shown that ultimate tensile strength is mainly controlled by the most critical pits and the remaining section, while ductility is more strongly affected by residual thickness and strain localisation [3]. Damage-mechanics simulations of corroded reinforcing steel have also shown reduced ductility and a shortened yield plateau as mass loss increases [6]. Fracture strain and toughness are also considered because they are more sensitive indicators of pitting damage.

This distinction is relevant to the present dataset because the measured UTS values do not show a clear monotonic reduction with exposure. However, the finite element results can still show earlier strain localisation and reduced deformation capacity.

The cylindrical pits used in this thesis are not treated as exact natural corrosion pits but as a controlled idealisation that isolates the geometric effect of localised material removal.

Pit topography is relevant to the flatter post-yield response observed in some of the pitted finite element curves. The stress and strain fields around a pit are not uniform because the pit root and pit edge act as local stress concentration regions. This is consistent with the reduced apparent hardening observed in the pitted models, even though the same material hardening curve was used.

2.3 Modelling Approaches for Corroded Steel

Corroded steel can be modelled using different levels of detail. The simplest approach is to use analytical net-section reduction or empirical knockdown factors. These methods estimate residual capacity directly from mass loss or thickness loss. They are simple and efficient, but they cannot represent local stress concentration or the actual morphology of pitting corrosion.

Finite element models with one or a few idealised pits provide more detail because they can represent local stress concentration. However, these models still do not capture the spatial randomness of real corrosion damage. At the highest level of detail, the actual corroded surface can be reconstructed using three-dimensional laser scanning or micro-computed tomography and then analysed directly in a finite element model. These morphology-based models have been shown to predict ultimate strength and fracture location with good accuracy when checked against tensile tests [7], [13]. Micromechanical ductile fracture criteria, such as void-growth models and stress-modified critical strain models, have also been used in finite element analysis to predict crack initiation in mild structural steels [8].

Reverse-engineered surface models offer high geometric fidelity, yet they remain specimen-specific and demanding to obtain. While useful for analysing a particular corroded specimen, such models do not readily offer a practical means of generating new, statistically representative corrosion fields. The present study therefore adopts a stochastic pit-generation approach, positioned between simple net-section models and full surface reconstruction. This approach represents pitting morphology while remaining reproducible and suitable for repeated finite element simulations.

Within this stochastic pit-generation approach, a population of pits or a random corrosion-depth field is generated using statistical information drawn from corroded surfaces. The resulting geometry is subsequently analysed through finite element analysis to examine how corrosion morphology influences mechanical behaviour. Random-pit and random-field models have been developed in Abaqus and LS-DYNA and validated against tensile tests on corroded steel plates. Such studies demonstrate that stochastic corrosion models can reproduce reductions in mechanical properties, the scatter arising from corrosion morphology, and in some cases, shifts in failure mode relative to uniform corrosion idealisations [1], [2], [11], [12], [17].

Monte Carlo studies extend this concept further, generating numerous independent corroded surfaces and analysing each through finite element analysis. The resulting data are then used to develop probabilistic models of the mechanical properties of corroded steel [18], [19]. A full Monte Carlo simulation is not attempted in the present study. Rather, a seed-controlled stochastic pit-generation workflow is adopted, in which random pit fields are generated under defined radius, spacing, depth and mass-loss constraints. Reproducibility of the generated morphology is thereby achieved, allowing it to be checked against the target corrosion severity.

Generating pitted geometry through a dedicated program offers the practical advantage of allowing pit morphology indicators to be recorded directly, including pit radius, pit depth, pit density, depth-to-width ratio and achieved mass loss. This information can then be transferred into the finite element model efficiently and repeatably [3]. Idealised pit shapes, such as hemispherical, semi-ellipsoidal, conical and cylindrical forms, are commonly used within this type of modelling approach to keep the analysis practical. Such shapes are typically described by radius or diameter, depth, and ratios including depth-to-width or depth-to-thickness [5], [24].

Direct surface reconstruction represents the highest-fidelity numerical approach, as the finite element model is created directly from the measured corroded surface. Laser-scan-based and surface-profile-based models have demonstrated that local thickness fields can improve predictions of residual tensile strength and fracture location [7]. This approach, however, is specific to the measured specimen and requires the actual corroded surface to be scanned prior to modelling. It is therefore less suited to studies aiming to run repeated parametric models with controlled mass loss and controlled pit statistics.

A practical middle ground between uniform thickness reduction and full surface reconstruction is offered by random field and stochastic pitting approaches, in which the corroded surface is represented through statistically generated pits or corrosion-depth fields. The finite element analysis can then be repeated to examine how morphology scatter affects the mechanical response [1], [11], [12]. Such a modelling approach suits the present thesis well, given that the aim is not to reproduce one exact pit pattern but rather to establish a repeatable workflow linking mass loss, pit morphology and tensile response.

2.4 Research Gap and Reference Study

The experimental and methodological basis of this thesis is a laboratory and modelling programme on low-carbon structural steel coupons immersed in 5% sodium chloride solution. In that programme, coupons were tested in tension from Day 0 to Day 42. Gravimetric mass loss was measured, pit morphology was characterised, and random pit fields generated in MATLAB were realised in Abaqus to simulate the corroded tensile response. This dataset provides the experimental basis for the present study and supports the use of a cylindrical-pit, mass-loss-controlled modelling workflow.

The main modelling components used in this workflow are consistent with approaches reported in the corroded steel literature. These include stochastic generation of pit populations, statistical description of pit dimensions, use of idealised pit geometry, pit sizing based on mass loss, and geometry-based finite element modelling. Therefore, the contribution of this thesis is not that each individual modelling component is new. Rather, the contribution is in combining these components into a clear and reproducible workflow for the present tensile coupon dataset.

The research gap addressed in this thesis is the need for a workflow that links generated pit geometry directly to a measured corrosion severity for each model realisation. In many studies, random pits, idealised pit shapes and finite element simulations are used as separate modelling steps. However, the achieved corrosion severity of each generated geometry is not always explicitly checked against the target mass loss. In this study, each pit field is generated under defined geometric rules, including edge clearance, non-overlap, pit radius limits and pit depth limits. The total removed pit volume is then converted back into mass loss and compared with the target measured mass loss.

2.5 Quantitative Findings from Literature Review

The qualitative discussion above finds support in specific findings from the screened literature. These findings are useful for interpreting the finite element curves and benchmarking the predictive relationships proposed later in this thesis.

Finite element studies of single idealised pits generally show that pit aspect ratio is an important geometric parameter governing stress concentration. For semi-elliptical pits, the stress concentration factor depends mainly on the depth-to-width ratio rather than on absolute pit size [13].

Long-term and atmospheric exposure studies report that corrosion depth or mass-loss depth can often be represented using an approximately normal distribution; pit depth and aspect ratio, however, may be better described using a lognormal distribution for more developed pitting [20]. The Gaussian preferred-radius assumption used in this thesis is therefore reasonable for the low-to-moderate corrosion severity considered. At the same time, the generator also reports lognormal and Weibull fits, so that the assumed distribution can be checked and modified for more developed pitting cases if required.

2.6 Positioning of the Study

The present study can be positioned by considering what is kept constant and what is allowed to vary. The material model is kept constant, while the corroded geometry is varied.

The present study also represents the corroded region as a population of discrete pits rather than as a continuous corrosion-depth field. Each pit has a recorded position, radius, depth and volume. This differs from random-field models, where corrosion is represented as a spatially varying depth field [11], [12], [18]. It also differs from single-pit stress concentration studies, where the response is controlled by one idealised defect rather than by a random pit population [13]. In this thesis, the pit population can be regenerated using the recorded random seed, which makes the workflow repeatable.

A further distinction lies in how the generated pit population is linked to measured mass loss through a volume constraint. The total volume removed by the generated pits is converted back into mass loss and compared against the target value for each realisation. This step matters because it checks how closely the generated geometry represents the intended corrosion severity, not merely whether it does so at all. The workflow therefore provides an auditable connection between measured mass loss, generated pit morphology and finite element geometry.

The remaining chapters are organised, based on this positioning, around the main requirements of the study.

3. Experimental Programme

This chapter describes the experimental programme that provides the dataset against which the numerical workflow is calibrated. The programme comprised uniaxial tensile tests on low-carbon structural-steel coupons in the uncorroded condition and after accelerated corrosion in a chloride solution for several exposure periods. The experimental method follows established tensile-testing and corrosion standards; the emphasis here is on those features of the programme that are relevant to the modelling, namely the coupon geometry, the corrosion exposure procedure and the tensile-testing procedure. The resulting measurements, comprising the mass loss and pit characterisation, the tensile response, and the scatter of that response between nominally identical coupons, are reported and discussed in Chapter 4.

The experimental data used in this thesis were obtained from a concurrent study conducted by another student within the same research group. As the present work focuses on the numerical and predictive aspects of pitting corrosion, the experimental methodology is summarised only to the extent necessary to contextualise the data, and a detailed literature review of experimental corrosion testing techniques is not undertaken here.

3.1 Material and Specimen Geometry

The material used in this study was a low-carbon structural steel supplied as thin plate. Flat dog-bone tensile coupons were machined with the longitudinal axis aligned with the plate rolling direction. The coupon geometry followed the proportional flat-specimen requirements of ISO 6892-1 [S1]. The reduced section had a parallel length of 65 mm, a width of 12.5 mm and a thickness of 2.0 mm, giving a nominal original cross-sectional area of 25 mm^2.

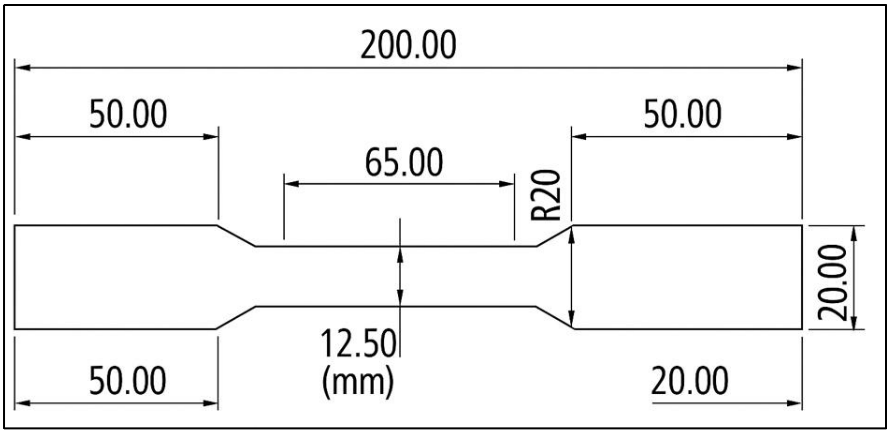

Figure 3.1 - Dimensions of a typical dog-bone steel coupon specimen

Engineering stress was calculated using the original cross-sectional area of the reduced section. Engineering strain was calculated using the original gauge length adopted for the tensile test measurement. In the experimental tests, this gauge length was 50 mm and was located centrally within the 65 mm parallel section. The nominal volume of the reduced section was approximately 1.625×10^3 mm³. Wider shoulders and gripping ends were included so that yielding and fracture would occur within the reduced section rather than at the grips. The same nominal coupon geometry was used for all exposure groups, so that differences in tensile response could be attributed to corrosion effects rather than specimen size.

A total of twenty-four coupons were prepared and divided into six exposure groups. These were Day 0, Day 14, Day 21, Day 28, Day 35 and Day 42, with four coupons in each group. The Day 0 coupons were left uncorroded and were used to define the baseline material response for finite element calibration in Section 5.8.

Before immersion, the steel coupons were manually abraded to remove the original coating, oxide layer and loose surface contaminants. A progressive grit sequence of P120, P240, P320 and P800 abrasive papers was used, following the general surface-preparation approach adopted in previous corrosion studies. The purpose of this step was to produce a consistent exposed steel surface before chloride immersion. Visual inspection and microscope observation confirmed that the dark surface layer had been removed after the final P800 preparation stage, leaving a brighter metallic steel surface.

Figure 3.2 - Gradual Sanding to P800, top to bottom

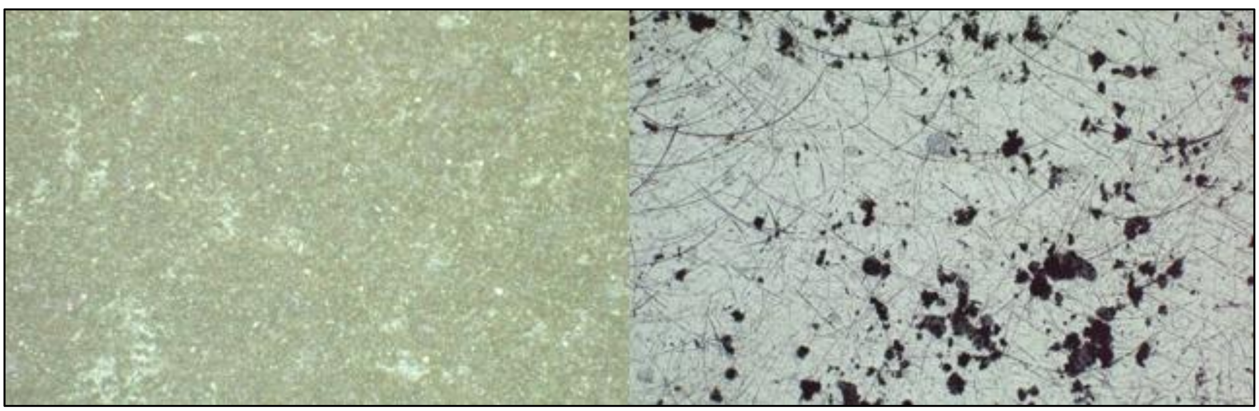

Figure 3.3 - *Microscopic view of coated (left) and coating-removed steel surface (right)*

Each coupon was then labelled according to its exposure group and specimen number. The shoulder and gripping regions were protected with waterproofing tape so that corrosion was concentrated on the reduced gauge section only.

Figure 3.4 – *Preparation of 4 nos. of steel coupons for testing at Day 14 to 42 at 7-day intervals for immersion corrosion of the samples.*

Figure 3.5 – *Side view of the testing coupons depicting that the gauge section is lifted off the container to ensure corrosion occurred on all unwrapped exposed surfaces.*

This was done to minimise corrosion in the clamping regions, which could otherwise promote premature failure near the grips or affect the reliability of the tensile test. Part of the assumption in FE modelling is that there is no corrosion occurred outside of the exposed gauge section surfaces.

The coupons were weighed after preparation and before immersion to obtain the initial mass. After the assigned immersion period and corrosion-product removal, the cleaned coupons were weighed again. The difference between the initial and cleaned masses was used to determine the absolute metal loss. For consistency with the finite element model, this mass loss was later expressed as a percentage of the exposed gauge-section mass rather than the full coupon mass.

The use of four coupons per exposure group is important because the corrosion effects at the measured mass-loss range are expected to be small. With replicate specimens, the mean response and the within-group scatter can be calculated. This makes it possible to judge whether differences between exposure groups are physically meaningful or whether they fall within normal coupon-to-coupon variability. If only one coupon were tested at each exposure period, it would be difficult to separate corrosion-induced degradation from material scatter, gripping variation or local surface differences between specimens.

3.2 Corrosion Exposure Procedure

Corrosion was introduced by immersion in a 5% sodium-chloride solution, providing an accelerated chloride environment representative of marine and de-icing exposure and consistent with the immersion procedure of ASTM G31 for laboratory immersion corrosion testing [S2]. The coupons of each exposure group were immersed for the nominal period of their group, from 14 to 42 days, so that a range of corrosion severities was produced. During immersion exposure, corrosion was able to develop on all exposed surfaces of the gauge section. This differs from the later finite-element idealisation, where pits were introduced on one main gauge surface for numerical control and mesh stability.

The gripping ends and shoulders were protected during immersion so that corrosion was concentrated on the reduced gauge section. This is important for the interpretation of mass loss in this thesis. Although the full coupon was weighed before and after corrosion exposure, the corrosion-relevant mass-loss percentage was referenced to the exposed gauge-section mass. This basis was adopted because the gauge section was the region intentionally exposed to the sodium-chloride solution and the region represented as the corroded zone in the finite element model. Because the unmasked gauge section was fully immersed in the solution, corrosion developed on all its exposed surfaces which is on both flat faces and on the two machined edges of the gauge length, rather than on a single face only.

The gauge-section mass-loss calculation assumes that essentially all of the measured metal loss occurred within this exposed gauge region and that the taped shoulders and gripping ends lost a negligible amount of metal and any imperfection in the masking would transfer a small part of the measured loss to the protected regions and is treated as a source of uncertainty in the reported severity.

Following immersion, corrosion products were removed by chemical cleaning in accordance with ISO 8407 [S3], using a proprietary chelating de-rusting agent that dissolves iron oxides while minimising removal of the parent steel. Each coupon was weighed before immersion and after cleaning, and the absolute metal loss was calculated from the difference between the initial and cleaned masses.

The cleaned absolute mass loss was normalised by the exposed gauge-section mass to obtain the corrosion severity used in the thesis. This approach yields a higher percentage mass loss than normalising by the full coupon mass, since the full coupon includes protected shoulders and gripping regions not intended to corrode; the same absolute mass loss is described in both cases, and only the reference mass changes. The gauge-section basis is used throughout the modelling chapters because it provides a consistent link between the measured metal loss and the volume removed from the exposed gauge region in the numerical pit-generation workflow.

The cleaning procedure matters because it affects the measured metal loss. Mass loss may be underestimated if corrosion products are not fully removed, and overestimated if the cleaning process removes a small amount of parent metal. The gravimetric mass loss used in the numerical model should therefore be interpreted as cleaned metal loss, not simply the visible amount of rust on the coupon surface.

3.3 Tensile Testing Procedure

Uniaxial tensile tests were carried out using an Instron 5982 universal testing machine with a 100 kN capacity under displacement control at a quasi-static loading rate, in accordance with ISO 6892-1 [S1]. Load was recorded from the machine load cell. Elongation was recorded from the crosshead displacement and, where available, from an extensometer over the gauge length.

Figure 3.6 - Instron 5982 machine and tensile testing software

Engineering stress was calculated by dividing the measured load by the original cross-sectional area of the reduced section. Engineering strain was calculated by dividing the measured elongation by the original gauge length used for the tensile measurement. From each engineering stress-strain curve, the main quantities extracted were ultimate tensile strength, strain at ultimate tensile strength, fracture strain and toughness. Ultimate tensile strength was taken as the maximum engineering stress. Fracture strain was taken as the engineering strain at the final load drop. Toughness was calculated as the area under the engineering stress-strain curve up to fracture and expressed in $MJ \cdot m^{-3}$.

These quantities were used because the tensile response of corroded steel cannot be described by maximum stress alone. As discussed in Chapter 2 and Section 5.8, corrosion can have a stronger effect on deformation-related properties such as fracture strain and toughness than on ultimate tensile strength [3], [4]. Therefore, the experimental results are interpreted using both strength and ductility-related measures.

4. Experimental Test Results and Discussion

This chapter presents and interprets the findings from the experimental programme outlined in Chapter 3. The discussion first considers the gravimetric mass-loss results and the observed pit morphology, followed by the tensile behaviour of the uncorroded and corroded coupons. The corrosion progression associated with the exposure durations and the scatter between nominally similar specimens are then examined. Attention is given to the key descriptors that connect the experimental work with the numerical modelling: corrosion severity expressed through mass loss, the measured tensile properties, and the variability within each specimen group. These results provide the experimental basis for assessing the finite-element workflow presented in Chapter 5.

4.1 Mass Loss Measurement and Pit Characterisation

The gravimetric mass loss is the primary corrosion descriptor used throughout this thesis. The absolute mass loss was obtained from the measured difference between the initial coupon mass and the cleaned post-corrosion mass.

For mechanical interpretation and numerical modelling, this absolute loss was expressed as a percentage of the exposed gauge-section mass, because the reduced gauge section was the region intentionally exposed to corrosion and the region represented by the generated pitted geometry.

The experimentally measured mass loss was used as the basis for defining equivalent target volume loss levels in the numerical model, rather than as a direct map of individual pit locations.

Sample	Initial Coupon Weight (g)	Coupon Weight After Corrosion Loss (g)	Calculated Initial Mass of Gauge Length Area (g)	Mass Loss (g)	Remaining Mass (g)	Mass Loss	Representative Mass Loss (%)
D0-1	52.88	52.88	12.75625	0	12.756	0.00%	0.00 ± 0.00
D0-2	51.68	51.68	12.75625	0	12.756	0.00%	
D0-3	52.62	52.62	12.75625	0	12.756	0.00%	
D0-4	52.43	52.43	12.75625	0	12.756	0.00%	
D14-1	52.8	52.57	12.75625	0.23	12.526	1.80%	1.29 ± 0.36
D14-2	52.82	52.66	12.75625	0.16	12.596	1.25%	
D14-3	52.62	52.5	12.75625	0.12	12.636	0.94%	
D14-4	52.79	52.64	12.75625	0.15	12.606	1.18%	
D21-1	52.31	52.11	12.75625	0.2	12.556	1.57%	1.74 ± 0.13
D21-2	52.69	52.46	12.75625	0.23	12.526	1.80%	
D21-3	51.99	51.77	12.75625	0.22	12.536	1.72%	
D21-4	52.5	52.26	12.75625	0.24	12.516	1.88%	
D28-1	52.77	52.45	12.75625	0.32	12.436	2.51%	1.94 ± 0.41
D28-2	52.63	52.43	12.75625	0.2	12.556	1.57%	
D28-3	52.62	52.4	12.75625	0.22	12.536	1.72%	
D28-4	52.48	52.23	12.75625	0.25	12.506	1.96%	
D35-1	52.84	52.56	12.75625	0.28	12.476	2.20%	2.20 ± 0.11
D35-2	52.82	52.55	12.75625	0.27	12.486	2.12%	
D35-3	51.73	51.46	12.75625	0.27	12.486	2.12%	
D35-4	52.15	51.85	12.75625	0.3	12.456	2.35%	
D42-1	52.79	52.49	12.75625	0.3	12.456	2.35%	2.49 ± 0.21
D42-2	52.54	52.2	12.75625	0.34	12.416	2.67%	
D42-3	52.91	52.62	12.75625	0.29	12.466	2.27%	
D42-4	52.4	52.06	12.75625	0.34	12.416	2.67%	

Table 4.1 – *Mass Loss Calculation of Experimental Corrosion Dog-bone Steel Specimen from Day 0 to Day 42. Assumed mass loss only occurs at gauge length sections*

On this gauge-section basis, the mean mass loss increased from approximately 1.29% at Day 14 to approximately 2.49% at Day 42. These values correspond to the same absolute metal losses measured during the experimental programme, but they are normalised by the exposed gauge-section mass rather than by the full coupon mass. The gauge-section normalisation is therefore more appropriate for linking the experiment to the finite element model, where material is removed only from the exposed gauge surface. Consistent with the scatter emphasised elsewhere in this thesis, the mass loss also varies within each exposure group. The within-group standard deviation of the gauge-section mass loss (from the four coupons in the table above) is approximately ±0.36% at Day 14, ±0.13% at Day 21, ±0.41% at Day 28, ±0.11% at Day 35 and ±0.21% at Day 42. The scatter is largest at Day 28, where one coupon (D28-1) lost 2.51% while another lost only 1.57%, so the group means should be read together with this spread rather than as exact severity levels. The individual per-coupon values and group mean in the table above were cross-checked for internal arithmetic and normalisation consistency; they should also be verified against the original weighing records.

The low absolute corrosion severity remains important context for the mechanical results. Even when expressed on the gauge-section basis, the mass losses remain within a low-severity range. The corresponding reduction in net section is small, so a large reduction in UTS is not expected from the experimental results alone. Instead, any mechanical effect of pitting is expected to appear more clearly through local strain concentration, fracture strain and toughness.

Exposure	Nominal mass loss Δm (%)	Approx. mean pit diameter (µm)
Day 0	0 (uncorroded baseline)	-
Day 14	1.29	Smaller early-stage pits, not quantitatively measured

Exposure	Nominal mass loss Δm (%)	Approx. mean pit diameter (μm)
Day 21	1.74	Smaller early-stage pits, not quantitatively measured
Day 28	1.94	Transitional pit development, not quantitatively measured
Day 35	2.20	~80–120 (qualitative only)
Day 42	2.49	~150–200 (qualitative only)

Table 4.2. *Gauge-section mass loss and representative pit size by exposure period. The mass-loss values are referenced to the exposed gauge-section mass, rather than the full coupon mass, because the reduced gauge section was the region intentionally exposed to the sodium-chloride solution and modelled as the corroded region in Abaqus. Pit diameters are indicative ranges from scanning-electron-microscopy examination for qualitative purpose only and are not quantitative.*

Scanning Electron Microscopy (SEM) imaging indicated a progressive increase in characteristic pit diameter with exposure duration. The observed pit sizes increased from smaller early-stage pits at lower exposure durations to approximately 80–120 μm by Day 35 and further increased to approximately 150–200 μm by Day 42. This suggests progressive pit growth, pit coalescence, and surface deterioration with continued immersion exposure. This observation provides the physical justification for representing corrosion as a population of discrete pits in the finite element model and for examining descriptors beyond mass loss alone [1], [16], [22].

In the present programme the pit-morphology evidence is primarily qualitative. It consists of the scanning-electron-microscope images and the approximate pit-diameter ranges reported in Table 4.2. Pit depth, pit density, pit-area ratio and surface roughness were not measured quantitatively. The statistical pit-radius, pit-depth and aspect-ratio assumptions used in the generator (Chapter 5) are therefore informed by the literature rather than calibrated against measured morphology for these specimens; the fitted normal, lognormal, truncated-normal and Weibull forms are retained so that they can be compared with measured pit statistics if such data are obtained in future work

(Section 8.2). The quantitative link between the experiment and the finite-element model is consequently made through the measured mass loss, not through a measured pit population.

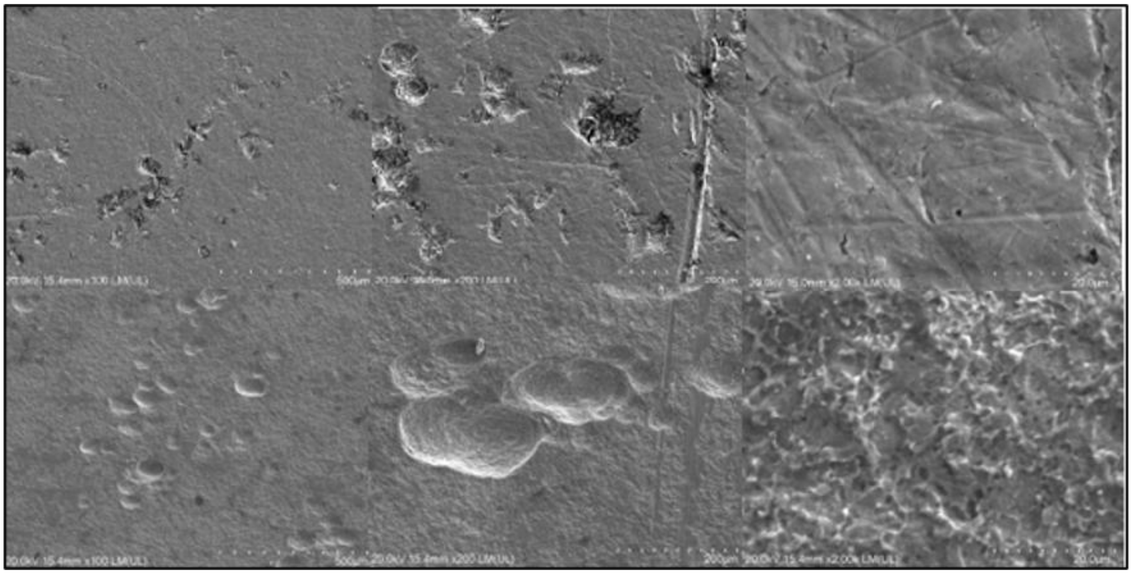

Figure 4.1 - SEM microscopy of pitted specimen from Day 0 to Day 42

4.2 Tensile Test Results

The measured tensile properties are summarised in Table 4.3 as the group mean and standard deviation of the four coupons in each exposure group. The mass-loss values are reported on the exposed gauge-section basis to remain consistent with the finite element pit-generation workflow.

Three features of the experimental data are central to the remainder of the thesis. First, the UTS does not show a clear monotonic reduction with exposure over the range studied. The group-mean UTS varies by only a few percent across the exposure periods and increases slightly at the longer exposure durations; this upward variation is not interpreted as corrosion-induced strengthening but is instead attributed to normal coupon-to-coupon material scatter and testing variability. The Day 14 group, for example, has a standard deviation of approximately 32.6 MPa, comparable to the difference between several group means. Within the measured mass-loss range, therefore, the experimental UTS data do not show a corrosion knockdown that can be clearly separated from scatter.

Second, the fracture strain and toughness also do not show a statistically clear monotonic reduction with exposure. The group-mean fracture strain remains close to 0.12 across the exposure groups, and the group standard deviations are of similar order to the differences between group means; the toughness values follow the same general pattern and remain affected by scatter.

Third, the dominant feature of the dataset is the scatter between nominally identical coupons rather than a clear exposure-time trend. This should not be interpreted as a failed corrosion experiment; it is the expected outcome of testing at low corrosion severity, where corrosion-induced changes in global tensile properties are small and can be masked by ordinary material and testing variability.

This observation determines how the assessment must be framed. The experimental programme provides the uncorroded baseline, the measured material response and the realistic scatter of the tensile data. The experiment alone, however, cannot resolve the small geometric effect of pitting against its own scatter. The finite element model is therefore used in Chapter 5 as a controlled numerical tool in which the material properties are held constant and only the pitted geometry changes, allowing the geometric effect of pitting to be isolated without forcing a corrosion knockdown onto experimental data that do not support one.

For each exposure group or FE realisation group, the results were reported using the mean value and standard deviation. The mean was calculated as $\bar{x} = n^{-1}\sum x_i$, while the scatter was quantified using the sample standard deviation, $s = [\sum(x_i - \bar{x})^2/(n-1)]^{1/2}$. The results are therefore presented in the form $\bar{x} \pm s$, where $x_i$represents the individual value of mass loss, UTS, fracture strain, or toughness within the same group. Toughness was obtained by numerically integrating the engineering stress–strain curve up to fracture using the trapezoidal rule.

Exposure	Gauge section Mass Loss Δm (%)	UTS (MPa)	Fracture strain ε_f (-)	Toughness U (MJ/m³)
Day 0	0	723.8 ± 10.9	0.120 ± 0.002	82.0 ± 1.6
Day 14	1.29	713.0 ± 32.6	0.123 ± 0.004	82.9 ± 4.2
Day 21	1.74	738.3 ± 15.8	0.125 ± 0.005	87.7 ± 6.0
Day 28	1.94	750.4 ± 13.8	0.124 ± 0.003	88.9 ± 4.0
Day 35	2.20	746.6 ± 11.4	0.123 ± 0.004	87.2 ± 3.9
Day 42	2.49	756.2 ± 12.2	0.128 ± 0.006	92.1 ± 6.6

Table 4.3. *Measured tensile properties by exposure group, reported as mean ± standard deviation of four coupons. Mass loss is expressed as a percentage of the exposed gauge-section mass. The data show no monotonic corrosion knockdown in UTS, fracture strain or toughness that exceeds the coupon-to-coupon scatter at the studied corrosion severities.*

The absence of a monotonic experimental UTS reduction in the present dataset should not be treated as evidence that corrosion has no mechanical effect. It indicates that the corrosion severity is low enough for material scatter and local specimen variation to mask the global strength effect. Table 4.4 presents the post-processed true tensile properties obtained from the experimental engineering stress–strain curves. Each engineering stress–strain data point was converted using Equations 1.9 and 1.10 respectively:

$$\sigma_{\text{true}} = \sigma_{\text{eng}}\left(1 + \varepsilon_{\text{eng}}\right)$$

$$\varepsilon_{\text{true}} = \ln(1 + \varepsilon_{\text{eng}})$$

The true toughness was then calculated by numerical integration of the converted true stress–true strain curve using the trapezoidal rule. In this study, the engineering-to-true conversion was assumed to remain applicable over the full tensile response, and the resulting true quantities were used as post-processed comparative tensile measures. Although the stress and strain values change after conversion from engineering to true quantities, the calculated toughness remains effectively unchanged because the standard engineering-to-true transformation preserves the area under the stress–strain curve as the effects of the change in strain and stress effectively cancels each other.

Exposure	Gauge section Δm (%)	True UTS (MPa)	True Fracture strain	True Toughness U (MJ/m³)
Day 0	0	810.7 ± 12.3	0.113 ± 0.002	82.0 ± 1.6
Day 14	1.29	800.7 ± 36.7	0.116 ± 0.004	82.9 ± 4.2
Day 21	1.74	830.6 ± 18.2	0.118 ± 0.004	87.7 ± 6.0
Day 28	1.94	843.4 ± 15.7	0.117 ± 0.003	88.9 ± 4.0
Day 35	2.2	838.4 ± 13.1	0.116 ± 0.004	87.2 ± 3.9
Day 42	2.49	853.0 ± 14.5	0.120 ± 0.005	92.1 ± 6.6

Table 4.4. *Post-processed true tensile properties obtained from the experimental engineering stress–strain curves.*

4.3 Corrosion Kinetics and Surface-Characterisation

The interpretation of the experimental corrosion results depends on two related aspects: the development of mass loss with exposure time and the statistical character of the corroded surface. These aspects together provide the experimental basis for linking the measured corrosion severity to the numerical pit-generation workflow.

The corrosion severity used for modelling in this thesis is expressed as the mass-loss percentage referenced to the exposed gauge-section mass. This reference basis is appropriate because the gauge section was the region intentionally exposed to the sodium-chloride solution and the region represented by the pitted finite element geometry. Using the gauge-section basis changes the numerical percentage values relative to a full-coupon mass reference, though it does not change the absolute cleaned metal loss measured during the experiment.

Surface characterisation matters as well, since the numerical generator represents corrosion as a population of discrete pits rather than as uniform thinning. Corrosion depth and mass loss, according to the literature, can often be described using approximately normal distributions, while individual pit depths and aspect ratios for developed pitting are frequently represented by lognormal or extreme-value distributions [20], [21].

Both an average corrosion descriptor and a morphology descriptor are therefore required for the experimental and modelling interpretation. Mass loss provides the average severity and allows the removed pit volume to be controlled. The tensile response, however, also depends on local features such as pit depth, spacing and spatial arrangement.

4.4 Experimental Scatter and Interpretation

The experimental results show that the corrosion effect at the measured severity range is small relative to the scatter between nominally identical coupons. It is therefore important to identify the likely sources of variability so that the experimental trends are interpreted appropriately.

Part of the scatter is associated with normal material and testing variability. Even coupons cut from the same plate may show small differences in chemistry, rolling history, surface condition and through-thickness properties. These differences can produce variation in strength and ductility even before corrosion is introduced. Additional scatter may arise from specimen preparation, gripping alignment, grip condition and the measurement of elongation during tensile testing.

Corrosion introduces further variability. The cleaned gravimetric mass loss depends on the effectiveness and repeatability of the cleaning procedure. Incomplete removal of corrosion products may underestimate the true metal loss, while excessive cleaning may remove a small amount of parent steel and overestimate the loss. In addition, pitting corrosion is inherently localised and irregular. Two coupons with similar average mass loss may have different deepest pits, pit spacings and critical pit locations. These differences can affect fracture strain and toughness even when the global corrosion severity is similar.

For this reason, the four replicate coupons in each exposure group are used to report both the mean response and the within-group standard deviation. The analysis in later chapters is therefore based on group trends and mechanical interpretation, rather than on any single coupon result. This is particularly important at the low corrosion severities considered here, where the expected reduction in global tensile properties may be smaller than the natural experimental scatter.

The experimental mass-loss range obtained in this study was relatively small, with the measured corrosion severity remaining within a low effective gauge-section mass-loss range. As a result, the influence of corrosion on ultimate tensile strength was difficult to separate from the natural scatter of the tensile test results. Although variations in UTS were observed between exposure durations, the trend was not monotonic with increasing mass loss. Therefore, these small changes should not be interpreted as definitive evidence of corrosion-induced strength degradation.

The absence of a clear monotonic reduction in experimental UTS is considered reasonable for the corrosion severity examined. At low mass loss, the reduction in net cross-sectional area is limited, and the mechanical response may still be strongly affected by coupon-to-coupon material variability, local corrosion non-uniformity, specimen preparation, measurement uncertainty and tensile testing scatter. In some cases, these sources of variability may be larger than the actual strength reduction caused by corrosion. Therefore, the experimental UTS results are interpreted cautiously as scatter-dominated within the investigated mass-loss range.

This does not mean that pitting corrosion has no mechanical effect. Rather, it indicates that the experimental corrosion severity was too low for a clear monotonic strength reduction to be resolved reliably from the available test data. For this reason, the FE study was used to provide a controlled geometry-isolated assessment of the effect of pitting. By keeping the material model constant and introducing mass-loss-matched pit geometries, the numerical model allowed the influence of geometric material loss and local strain concentration to be examined separately from experimental scatter. The FE results are therefore interpreted as controlled numerical evidence of the geometric effect of pitting, while the experimental results provide the physical corrosion basis and reference tensile response.

5. Numerical Analysis

This chapter presents the numerical analysis. It first describes the finite element workflow developed in this study, then validates that workflow against the experimental results of Chapter 4 and finally interprets the simulations as a parametric study of mass loss and pit morphology.

In this study, corrosion severity was defined using the effective mass-loss ratio of the exposed gauge section rather than the full coupon. This basis was adopted because the reduced gauge section was the region intentionally exposed to corrosion and subsequently represented in the pit-generation and finite-element modelling workflow. The shoulder and grip regions were not modelled as corroded regions in the numerical analysis. Therefore, the measured mass loss was converted to an equivalent gauge-section mass-loss ratio for consistency with the region in which pits were generated.

The workflow consists of two linked stages. The first stage is a stochastic pit-generation process implemented in MATLAB. This stage produces a randomised population of pits that is constrained to reproduce a measured mass loss. The second stage is a finite element modelling process implemented in Abaqus using a coupon template and running a custom Python script to read the outputs of the MATLAB generated pit Excel file and cut into the coupon specimen. This stage converts the generated pit population into discrete cavities in the tensile coupon model and simulates the tensile response. The simulation is then run on ABAQUS with the completed modelling with appropriate properties, loading, boundary conditions and mesh setup.

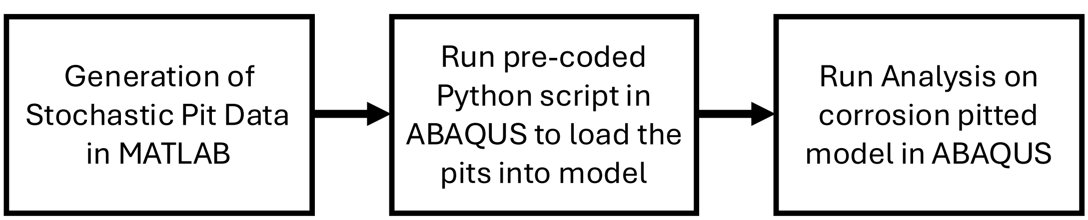

Figure 5.1- Simplified 3-step modelling process for analysing stochastically pitted steel coupon models

The chapter first explains the modelling rationale behind the main decisions. It then describes the pit-generation method, the mass-loss basis for pit sizing, the Abaqus pit realisation, the geometry and material model, the element and mesh selection, the loading and boundary conditions, and the quasi-static verification.

All successful finite-element simulations from the final adopted modelling workflow were included in the results and subsequent interpretation. No completed production run was removed simply because its response was less favourable or showed greater scatter than the other realisations. The reported results therefore represent the full set of accepted simulations generated using the final material model, damage settings, mesh strategy, boundary conditions and pit-generation procedure described in this chapter.

Abaqus/Explicit was adopted for the pitted coupon simulations because the stochastic pit fields produced complex local geometry and mesh distortion around the cavities, conditions that can be difficult to solve robustly using an implicit formulation. Although the experimental tensile test is quasi-static, an explicit formulation can still be used provided that inertial effects remain small. The simulations were accordingly assessed using energy-balance checks to confirm that the response was quasi-static.

The kinetic energy was monitored relative to the internal energy throughout the analysis. A low kinetic-energy-to-internal-energy ratio indicates that the deformation response is governed primarily by strain energy rather than inertial effects. Artificial energy was also monitored to ensure that hourglass control and numerical stabilisation did not contribute significantly to the total response. Where mass scaling was used, the applied scaling factor and resulting stable time increment were reported, and the force-displacement response was checked to confirm that mass scaling did not alter the quasi-static tensile behaviour.

Almost all the preliminary FE runs were excluded from the results, as they formed part of the model-development and calibration stage rather than the final production dataset. These trial simulations served to adjust and assess modelling parameters such as the plastic stress-strain input, damage-initiation strain, damage-evolution displacement, mesh controls and solution stability. Their purpose was to establish a stable Day 0 baseline model and a consistent numerical workflow before the model was applied to the corroded and projected pitting cases. Once the final modelling settings had been selected, these calibration and diagnostic runs were not carried through into the parametric results.

One exception within the production dataset concerns the Day 42 Cyl-1 realisation and its mesh sensitivity study which carried through to the production stage simulations. These were run to a displacement of 15 mm rather than the 10 mm applied in the standard production simulations. This extension was adopted because fracture occurred earlier than in the other realisations, and the additional displacement range was used to confirm that the damage evolution had fully completed and that no residual load-carrying capacity remained beyond the point of fracture. The extended run followed the same material model, damage settings, mesh strategy and boundary conditions as the standard production cases, so the result remains consistent with, and directly comparable to, the rest of the accepted simulation set.

Runs that terminated because of numerical instability, excessive element distortion, or incomplete solution were also not treated as valid result cases. Where such behaviour occurred, the run was used only to inform modelling decisions, such as mesh selection or the exclusion of unstable pit-shape trials. The final reported dataset therefore consists only of completed simulations from the adopted workflow, while preliminary calibration runs and unsuccessful numerical trials were excluded for methodological consistency.

5.1 Modelling Rationale

Although the immersion exposure allowed corrosion to develop on multiple exposed surfaces of the gauge region, the finite-element pitting model idealised the corrosion morphology on one main surface of the reduced section. Therefore, the numerical model was not intended to reproduce the exact three-dimensional corrosion distribution observed experimentally on all exposed surfaces. Instead, the model provided a controlled representation of localised material removal so that the influence of pitting morphology and prescribed mass loss on tensile response could be investigated in a consistent manner.

The adoption of a one-face pitting idealisation represents a deliberate modelling simplification aimed at preserving mesh quality, ensuring numerical stability, and maintaining consistency across numerical cases. Given that the coupon thickness is relatively small compared to the pit dimensions, the introduction of pits on multiple opposing surfaces would likely result in extremely thin residual ligaments, significant local element distortion, and potential instability in element deletion or damage localisation. Such conditions would hinder the clear differentiation between the mechanical effects of corrosion severity and numerical artefacts arising from inadequate meshing. By restricting pit placement to a single primary gauge surface, a consistent modelling workflow can be maintained across varying mass-loss levels and pit configurations, thereby enabling a controlled evaluation of the effects of prescribed material loss and localised pitting.

The Day-0 finite-element model was assessed against the full experimental engineering stress–strain response rather than ultimate tensile strength alone. The calibrated model reproduced the experimental ultimate tensile strength with close agreement, indicating that the peak load-carrying capacity of the uncorroded coupon was well represented. In addition, the overall shape of the stress–strain curve was examined, including the initial elastic response, the onset of yielding, the strain-hardening region and the final deformation capacity.

The same material model was used for all corroded FE simulations, calibrated from the uncorroded Day-0 tensile response. No corrosion-dependent change was applied to the elastic modulus, yield stress, plastic hardening behaviour or damage parameters. The numerical study therefore isolates the geometric effect of corrosion. Changes in tensile response arise only from the removal of material through the generated pit cavities, separating the influence of pit geometry and spatial distribution from possible corrosion-induced changes in the steel material properties.

The elastic region showed reasonable agreement with the experimental response. This confirmed that the applied elastic modulus and boundary conditions were appropriate for the global coupon response. Minor differences between the experimental and FE curves were expected in the yield region, since the material model used a simplified plastic stress-strain input and did not explicitly reproduce any local yield-point phenomenon or small experimental yield plateau. The strain-hardening portion of the curve carried more importance for the present study, as it governs the post-yield tensile response leading to ultimate strength. The FE model captured the general hardening trend and peak stress level of the Day-0 coupon, providing a suitable baseline material response for the subsequent corroded models.

The fracture strain was also considered, but it was interpreted more cautiously than ultimate tensile strength. The final failure point is sensitive to the adopted damage parameters, mesh discretisation and endpoint definition. The Day-0 model was therefore not judged solely by exact agreement in fracture strain. Instead, the calibration was considered acceptable because it reproduced the overall tensile response, including the elastic region, yielding behaviour, strain hardening and ultimate strength. This agreement was sufficient for isolating the geometric effect of corrosion in the subsequent FE simulations.

Three main decisions define the numerical workflow, each supported by the literature reviewed in Chapter 2.

The first decision is to represent corrosion as a change in geometry rather than as a change in material properties. The material model is calibrated using the uncorroded Day 0 tensile response, and the same material card is then used for all corroded simulations. Corrosion is introduced only by removing material from the coupon surface to form pits.

This approach suits the modest mass-loss range considered in this study. At this corrosion severity, chloride pitting mainly removes metal and creates local stress raisers. No direct experimental evidence in this programme suggests that the bulk constitutive behaviour of the remaining steel changed with exposure. Assigning a different material card to each exposure period would therefore mix the geometric effect of corrosion with an assumed material degradation effect, making the interpretation less clear. Previous damage-mechanics studies have shown that a single constitutive description combined with a geometric or mass-loss representation of corrosion can reproduce key features of the degraded tensile response [3], [6]. This supports the separation between material behaviour and corrosion geometry adopted in this study.

Secondly, treating corrosion as a population of discrete, randomly distributed pits rather than as uniform thickness loss or a single idealised defect. This follows from the localised and statistically variable nature of pitting corrosion discussed in Chapter 2. Previous studies have shown that localised corrosion can be more damaging than uniform corrosion at the same mass loss. Two specimens with the same mass loss may behave differently depending on how the material loss is distributed [15], [16], [17]. A stochastic pit field is therefore used to represent the random nature of corrosion morphology and to allow the separate effects of mass loss and pit morphology to be examined.

Thirdly, to idealise each pit as a regular geometric cavity. The production models in this thesis use flat-bottomed right circular cylindrical pits. Idealised pit shapes such as hemispherical, semi-ellipsoidal, conical and cylindrical pits are commonly used in finite element studies of pitted steel because they make geometry creation and meshing more practical [5], [24]. The aim of the model is not to reproduce the exact shape of every natural corrosion pit. Instead, it is to provide a controlled and reproducible framework for studying how pit severity and pit distribution affect tensile response.

The geometry-only corrosion assumption also improves modelling control. If the steel material properties were reduced for each exposure period, the simulation might predict a lower tensile capacity. However, it would not be clear whether that reduction was caused by the assumed material degradation or by the pit geometry. By keeping the material card fixed, the simulation becomes a controlled numerical experiment. The independent variable is the corroded geometry, while the constitutive response of the remaining steel is unchanged.

5.2 Stochastic Pit Generation (MATLAB)

The pit-generation stage was implemented in MATLAB as a stochastic algorithm for creating a population of pits on the exposed gauge surface of the coupon. The generated pit field was constrained by explicit geometric and physical rules, and the final pit list was written to a spreadsheet for transfer into the finite element model. The generator was seed-controlled, meaning that the same random seed reproduces the same pit field. This reproducibility is an important feature of the workflow because it allows each corrosion realisation to be regenerated, checked and compared.

Pit centres were placed on the exposed face using a random sequential placement method. Candidate pit centres were generated randomly and were accepted only if they satisfied the prescribed edge clearance and spacing requirements. These requirements ensured that pits remained within the gauge region and did not overlap physically. Each accepted pit was assigned a radius from a controlled statistical population. In the present study, the preferred pit radius was sampled from a Gaussian distribution within a specified radius range.

The generator also fitted normal, lognormal, truncated-normal and Weibull distributions to the generated radius, depth and aspect-ratio data. These distribution fits were written to the output file. This allowed the generated pit population to be compared with statistical forms reported for real corroded surfaces. The use of a Gaussian preferred radius was a deliberate modelling choice for the low-to-moderate mass-loss range considered in this study, where the pitting damage was still relatively limited. Previous studies have commonly reported lognormal distributions for more developed pitting [1], [20]. The generator therefore also reports lognormal and Weibull fits, allowing the assumed distribution to be checked against measured pit data and refined in future work if required.

Each pit was assigned a depth so that the total volume removed by all generated pits reproduced the target removed volume corresponding to the measured mass loss. The mass-loss calculation is described in Section 5.2.1. Pit depth was limited by a maximum depth-to-thickness ratio of $d/t \leq 0.25$. This limit was used to keep the generated pits within a physically reasonable proportion of the 2.0 mm plate thickness and to prevent perforation. If the requested mass loss could not be achieved within the allowable surface area, pit size range and depth limit, the generator issued a feasibility warning. This prevented the model from producing an unrealistic pit field.

The principal generator parameters are summarised in Table 5.1. Because the pit population was generated using fixed rules and a recorded seed, each realisation corresponded to a known corrosion severity rather than an arbitrary defect arrangement.

Parameter	Value / setting	Role
Pit shape	Flat-bottomed right circular cylinder	Idealised pit geometry
Layout scheme	Random sequential placement	Non-overlapping random pit field
Preferred radius distribution	Gaussian over r ≈ 0.5-1.25 mm (mean 0.875 mm, SD 0.15 mm; hard bounds 0.45-1.56 mm)	Pit-size population
Distribution fits output	Normal, lognormal, truncated-normal, Weibull	Check assumed vs real pit statistics
Edge clearance	≈ 0.5 mm minimum	Prevents edge breaching
Centre-to-centre spacing	≈ 0.5mm~1mm minimum (set by a 0.5 mm minimum edge-to-edge pit gap)	Prevents pit overlap
Maximum depth-to-thickness	$d/t \leq 0.25$	Keeps pits physically reasonable
Maximum pit count	250	Upper bound on population size

Parameter	Value / setting	Role
Mass-loss control	Summed pit volume equals removed target volume	Links geometry to measured mass loss, Δm
Reproducibility	Fixed random seed	Allows exact regeneration of a field
Specimen gauge dimensions (L × W × t)	65 × 12.5 × 2 mm	Defines the exposed face and section geometry
Steel density ρ	0.00785 g/mm³ (7.85 g/cm³)	Mass-to-volume conversion (Eq. 4.1)

Table 5.1. *Principal parameters of the MATLAB stochastic pit generator.*

Representative generated pit fields for the mildest and most severe exposure cases are shown in Appendix A. The corresponding distribution-fit plots for pit depth, radius and aspect ratio are also provided in Appendix A. The output statistics for each realisation are summarised by exposure group and listed seed by seed. The detailed placement, sampling, depth-scaling and feasibility checks of the algorithm are also described in Appendix A.

The idealised pit population used in the numerical model was deliberately coarser than the natural pit population observed during SEM examination. SEM observations indicated characteristic pit diameters of approximately 80 to 200 µm. The generated numerical pits, by contrast, adopted a larger bounded plan-diameter range of approximately 0.90 to 2.65 mm. The selected numerical pit dimensions were therefore not intended to reproduce the individual natural pits one-to-one. Instead, the SEM measurements served as a qualitative basis for defining physically plausible localised surface defects, while the pit dimensions were scaled to a size that could be represented reliably in the finite-element mesh.

This coarsening was necessary for practical computational reasons. Explicitly resolving the large number of sub-0.2 mm natural pits with sufficient local mesh refinement through the 2 mm coupon thickness would be computationally prohibitive, particularly for explicit tensile-to-fracture simulations involving damage localisation. The numerical model therefore represents the corrosion morphology using a smaller number of larger idealised pits, while preserving the required removed material volume. The quantitative link between the experiment and the numerical model is established through equivalent volume loss, and hence mass loss, rather than through exact pit count or individual pit size.

Within this modelling constraint, the geometric rules adopted in Table 5.1 were selected to maintain a physically reasonable and numerically stable idealisation. The minimum edge clearance ensured that pits remained within the exposed gauge region, while the minimum edge-to-edge spacing prevented artificial overlap and unrealistic pit coalescence. The depth-to-thickness limit of $d/t \leq 0.25$ restricted each pit to a moderate proportion of the 2 mm coupon thickness and avoided local perforation. The bounded pit-size range also ensured that each defect could act as a discrete stress raiser while remaining sufficiently large to be meshed reliably.

The stochastic generator has two main functions. First, it creates a physically possible corroded surface. This means that pits remain inside the gauge region, do not overlap and do not exceed the prescribed depth limit. Second, it creates a numerically traceable surface. Each pit has a recorded coordinate, radius, depth and volume contribution. This traceability allows the same geometry to be regenerated, audited and compared with other realisations.

The mass-loss constraint provides the main link between the experimental and numerical stages. The algorithm scales the generated pits so that the sum of their volumes corresponds to the measured or target mass loss, rather than selecting pit depth arbitrarily. This prevents the finite element geometry from being only a visual representation of corrosion. The generated surface is instead tied quantitatively to a corrosion severity that can be measured in the laboratory.

5.2.1 Mass-Loss Based Pit Volume Control

The target corrosion severity was imposed through a mass-loss based volume-control procedure. For each numerical case, the required mass loss was first converted into an equivalent volume of removed steel using the density of the material. The stochastic pit-generation algorithm then distributed this target volume among the generated cylindrical pits, such that the sum of the individual pit volumes closely matched the prescribed volume loss. In this way, the numerical corrosion severity was controlled by the total amount of material removed, even though the pits were idealised on one main surface rather than distributed over all experimentally exposed surfaces.

The link between the model geometry and the measured corrosion severity is made through volume. The measured mass loss Δm is converted to a target removed volume using the steel density ρ,

$$V_{target} = \Delta m / \rho, \tag{4.1}$$

and the pit depths are scaled during generation so that the summed volume of the cylindrical pits equals this target. For a single flat-bottomed cylindrical pit of radius r and depth h the removed volume is

$$V_{pit} = \pi r^2 h, \tag{4.2}$$

so that, for a population of N pits, the depths are determined by the constraint $\Sigma \pi r_i^2 h_i = V_{target}$ subject to the d/t limit.

Exposure	Target gauge mass loss Δm (%)	Achieved gauge mass loss Δm (%)	Range of Pit counts N across 4 cases	Gauge mass loss Δm (g)
Day 14	1.29	1.29	101~144	Δm = 0.165 g;
Day 21	1.74	1.74	105~147	Δm = 0.223 g
Day 28	1.94	1.94	101~149	Δm = 0.248 g
Day 35	2.20	2.20	123~148	Δm = 0.280 g
Day 42	2.49	2.49	123~151	Δm = 0.318 g

Table 5.2. *Target versus achieved mass loss for each modelled exposure.*

The full coupon mass was recorded during gravimetric measurements. However, the mass-loss ratio used in this thesis was referenced to the exposed gauge-section mass. This choice reflects the fact that corrosion exposure was intentionally limited to the reduced gauge section, while the shoulders and gripping regions were wrapped and protected during immersion. It is therefore more logical to attribute the measured material loss to the exposed gauge section, rather than to normalise it by the full coupon mass, which includes regions that were not intended to corrode.

On this basis, the experimental mass loss was interpreted using the gauge-section mass as the reference mass. The same gauge-section basis was then applied in the numerical pit-generation workflow. This keeps the experimental corrosion severity and the finite element corrosion geometry consistent, since both are based on the part of the coupon that was exposed to the sodium-chloride solution.

The whole-coupon mass-loss percentage and the gauge-section mass-loss percentage still describe the same absolute material loss in grams. The difference is only in the reference mass used for normalisation. When the full coupon mass is used, the percentage mass loss appears smaller because the protected shoulders and gripping regions are included in the denominator. When the gauge-section mass is used, the percentage mass loss is larger because it is referenced only to the exposed region where corrosion was intended to occur.

5.2.2 Direct Pit Insertion in Abaqus

The generated pit list is transferred to Abaqus through a Python script that reads the spreadsheet and cuts each pit as a cylindrical cavity from the gauge face of the coupon solid before meshing. The mapping between the spreadsheet columns and the cutter inputs is fixed (Table 5.3) so that the transfer is unambiguous and repeatable. The flat-bottomed cylindrical pit geometry is consistent between the MATLAB generator and the Abaqus cutter, the same shape and dimensions are used in both, which removes a common source of inconsistency between the geometry that is generated and the geometry that is analysed, and is a deliberate strength of the workflow. The pits are cut on a single exposed gauge face, consistent with the masked-exposure arrangement of the experiment (Section 3.2). Because both the generation and the realisation are scripted and seed-controlled, the complete corroded geometry can be regenerated exactly for any exposure case. This can be changed accordingly in the script as necessary should the output file needs to be modified.

Spreadsheet column	Item	Abaqus cutter input
B	Pit centre x-coordinate	Cavity centre x

Spreadsheet column	Item	Abaqus cutter input
C	Pit centre y-coordinate	Cavity centre y
D	Pit depth	Cylinder depth (into thickness)
F	Pit radius	Cylinder radius

Table 5.3. *Mapping from the pit-generation spreadsheet to the Abaqus pit-cutting script.*

5.3 Geometry and material model

The coupon was modelled as a three-dimensional deformable solid representing the reduced gauge section and shoulders of the flat dog-bone specimen. The nominal specimen dimensions followed those described in Section 3.1. A three-dimensional solid model was required because the corrosion pits were represented as local three-dimensional cavities. These cavities create local stress and strain concentrations through the thickness of the plate, which cannot be represented properly using a two-dimensional or shell idealisation.

Young's modulus and Poisson's ratio for structural steel defined the elastic response, while a tabulated true-stress and true-plastic-strain hardening curve defined the plastic response. Ductile failure was captured through a progressive ductile-damage model with element deletion, allowing the load-carrying capacity to decrease once damage initiated and enabling the coupon to separate after failure.

Calibration of the material model was performed once, using the uncorroded Day 0 tensile response, and the resulting material card was carried forward unchanged into all corroded simulations. The pit geometry therefore stood as the only principal difference between the uncorroded and corroded models, a principle that held equally across the different corroded exposure cases. By holding the material properties fixed in this way, the finite element simulations could isolate the effect of pitting geometry without introducing additional assumed changes to the steel itself.

Exposure	Gauge section Target Δm (%)	N pits	Mean radius (mm)	Mean depth (mm)	Max depth range (mm)	Mean (h/t)	Max (h/t) range	Pit density (/100 mm²)	Pit-area ratio (%)	$S_{a,eq}$ (mm)	$S_{q,eq}$ (mm)
Day 14	1.29	126 ± 20	0.709 ± 0.059	0.105 ± 0.001	0.139 – 0.145	0.052 ± 0.000	0.069 – 0.072	17.09 ± 2.68	27.26 ± 0.19	0.0286 ± 0.0000	0.0558 ± 0.0001
Day 21	1.74	123 ± 18	0.715 ± 0.048	0.142 ± 0.001	0.181 – 0.190	0.071 ± 0.001	0.091 – 0.095	16.75 ± 2.45	27.30 ± 0.15	0.0385 ± 0.0000	0.0751 ± 0.0003
Day 28	1.94	126 ± 23	0.712 ± 0.062	0.155 ± 0.002	0.205 – 0.213	0.078 ± 0.001	0.103 – 0.106	17.15 ± 3.18	27.55 ± 0.25	0.0428 ± 0.0000	0.0834 ± 0.0003
Day 35	2.2	133 ± 11	0.688 ± 0.027	0.176 ± 0.001	0.234 – 0.240	0.088 ± 0.001	0.117 – 0.120	18.04 ± 1.49	27.44 ± 0.03	0.0485 ± 0.0000	0.0943 ± 0.0002
Day 42	2.49	134 ± 13	0.685 ± 0.026	0.201 ± 0.005	0.260 – 0.277	0.100 ± 0.003	0.130 – 0.139	18.14 ± 1.74	27.25 ± 0.51	0.0550 ± 0.0000	0.1073 ± 0.0010

Table 5.4. *Summary of generated pit morphology for the Day 14–Day 42 FE models*

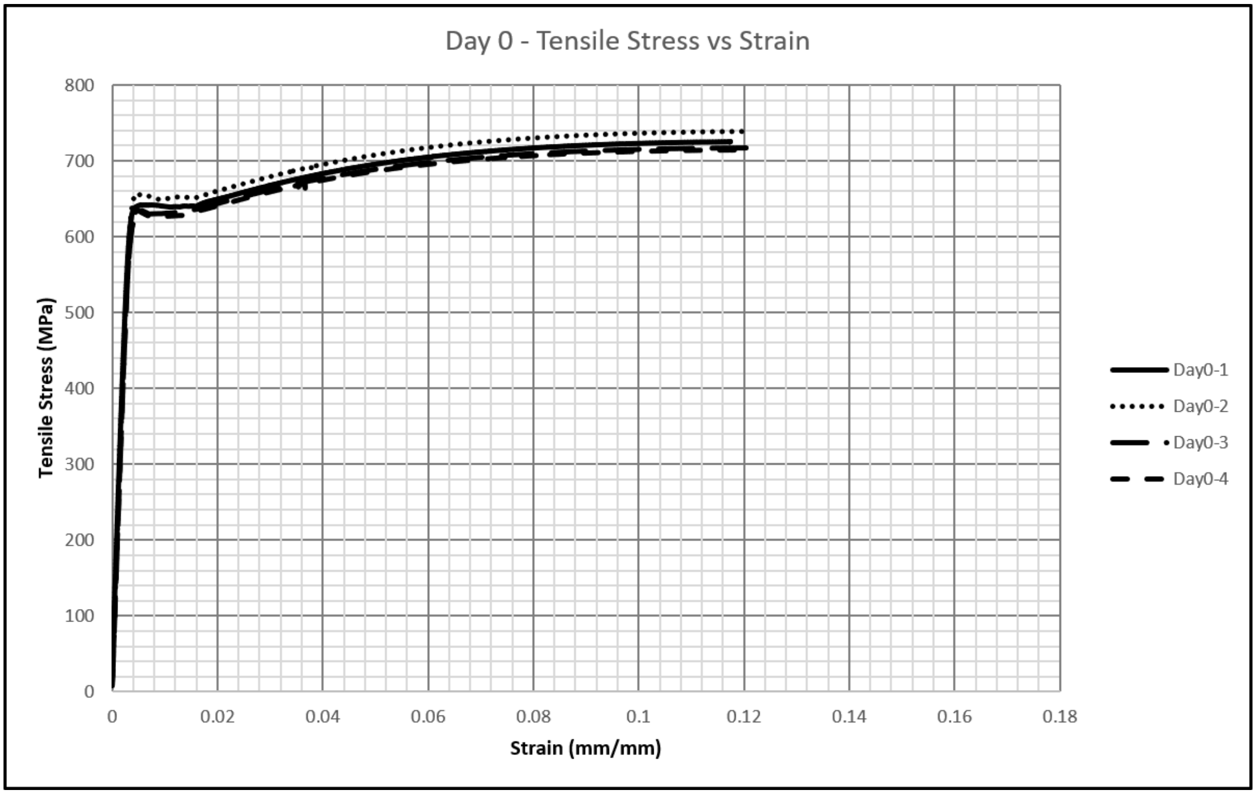

Figure 5.2. *Table depicting the tensile stress versus strain graphs of Day 0 baseline steel coupon samples subjected to uniaxial tensile testing using the Instron machine.*

Experimental Day 0 Sample 1 (Day0-1) was adopted as the representative baseline experimental curve for comparison with the finite-element model. The four Day 0 coupons showed similar uncorroded tensile behaviour, with comparable elastic response, yielding, strain hardening, and ultimate strength. Among these curves, Day0-1 lies within the main experimental response envelope and does not represent either the highest or lowest bound of the Day 0 results. It therefore provides a suitable representative curve for the uncorroded baseline condition.

A single experimental curve was required for direct curve-to-curve comparison with the numerical baseline model. Although an averaged Day 0 response could be calculated for selected scalar quantities such as ultimate tensile strength, fracture strain, and toughness, a point-by-point average stress–strain curve was not adopted. This is because the individual coupons do not necessarily reach necking, softening, and fracture at the same strain. Averaging the full curves, particularly near the post-peak region, could therefore generate an artificial response that was not physically measured in any individual specimen.

Day0-1 was selected on this basis as a representative experimental baseline curve, while the remaining Day 0 coupons were retained in the figure to show the natural experimental scatter. Using Day0-1 as the reference curve does not imply that the other Day 0 coupons were invalid. It instead provides a consistent baseline for assessing whether the finite-element model can reproduce the general uncorroded tensile response before corrosion pits are introduced. The strain obtained from the four steel coupons ranged between approximately 0.140 and 0.175. The Day 0 FE baseline model was therefore calibrated to produce fracture at a strain of approximately 0.155 to 0.160, taken as a representative mean of the experimental results.

The calibrated material card used in the production simulations is summarised in Table 5A-1 so that the model can be reproduced. Steel density was defined as 7.85×10^{-9} tonne/mm³. Linear isotropic elasticity was defined using a Young's modulus of 210,000 MPa and a Poisson's ratio of 0.3. The model used a tonne, millimetre and second unit system, in which force is expressed in Newtons and stress in MPa. Keeping the density, modulus, force and stress units consistent matters both for the Abaqus/Explicit analysis and for interpreting the quasi-static verification discussed later in this chapter.

Plasticity was represented using the von Mises yield surface with isotropic hardening. The hardening curve was defined using the true-stress and true-plastic-strain data listed in Table 5A-1. In the calibrated production material card, the true stress increased from 560 MPa at zero plastic strain to 840 MPa at a plastic strain of 0.16. Beyond the last tabulated point, the stress was held constant by extrapolation. Isotropic hardening was adopted because the tensile tests were monotonic and did not involve load reversal.

Using the standard conversion up to the onset of necking, the tabulated hardening curve was derived from the uncorroded Day 0 engineering stress-strain response, converting it to true stress and true plastic strain.

The Abaqus ductile-damage initiation criterion, followed by a damage-evolution law with element deletion, was used to represent ductile failure. An equivalent fracture strain of 0.13 at a stress triaxiality of 0.33 defined damage initiation, with the strain-rate term set to zero. This triaxiality value of 0.33 corresponds to the ideal uniaxial tensile stress state, in which the hydrostatic stress equals one third of the axial stress and the von Mises equivalent stress matches the axial stress.

Linear softening, together with a plastic displacement at failure of 0.22 mm, defined damage evolution in displacement form. Elements were removed once the damage variable reached unity, following the maximum-degradation rule. Mesh dependence in softening behaviour is reduced by defining post-initiation softening through displacement rather than strain.

The ductile damage parameters were selected through a physically guided calibration against the uncorroded Day 0 tensile response. The purpose of this calibration was to obtain a stable baseline model that reproduced the main experimental stress–strain behaviour before introducing corrosion pits. The damage-initiation strain was set to 0.13, which is close to the engineering fracture strain observed in the uncorroded Day 0 coupons, approximately 0.12. This allowed damage to initiate at a deformation level broadly consistent with the measured ductility of the material. The stress triaxiality was fixed at one third, corresponding to the nominal uniaxial tensile stress state in the coupon gauge section.

The plastic displacement at failure was set to 0.22 mm after trial adjustments to obtain a stable and gradual post-necking softening response leading to separation, rather than sudden element deletion. This produced a fracture response that was broadly consistent with the ductile behaviour observed in the tensile tests. However, the damage parameters should not be interpreted as independently calibrated fracture properties. They were adjusted within physically reasonable bounds to reproduce the baseline Day 0 response and were then kept constant for the subsequent corroded models. No separate multi-axial fracture-locus calibration was carried out. Therefore, the damage model is used primarily as a consistent numerical fracture framework for comparing uncorroded and pitted models, rather than as a fully validated material fracture law.

Material behaviour	Setting / value	Basis
Density	Uniform; 7.85×10^{-9} $t\cdot mm^{-3}$	Structural steel; consistent t–mm–s units
Elastic	Isotropic; E = 210 000 MPa, ν = 0.3	Room-temperature steel constants [3], [6]
Plastic – model	von Mises, isotropic hardening; constant extrapolation	Adopted for monotonic tensile loading of ductile steel.
Plastic – curve (σ_y MPa: ε_{pl})	560:0; 620:0.003; 670:0.01; 710:0.025; 760:0.06; 800:0.10; 825:0.135; 840:0.16	True stress–true plastic strain from Day-0 coupon
Ductile damage – initiation	ε_f = 0.13; triaxiality = 0.33; strain rate = 0; accumulation power 0	η = 1/3 is the uniaxial-tension value
Damage evolution	Displacement type; linear softening; u_f = 0.22 mm; maximum degradation; element deletion	Adopted to provide controlled post-peak stiffness degradation after damage initiation.

Table 5.5. *As-built Abaqus material card for the steel (material name "Steel"), calibrated once against the uncorroded Day-0 response and then held constants for all corroded models.*

The pits were idealised as flat-bottomed right circular cylinders. This pit shape was adopted for the production workflow for two main reasons. The first reason was numerical robustness. In the present study, cylindrical-pit models were much more reliable to construct, mesh and analyse than the conical-pit alternative. Across the attempted conical-pit simulations, only one case completed successfully. In contrast, the cylindrical-pit models ran reliably across all exposure cases. This is important because the workflow required repeated simulations of dense random pit fields rather than a single isolated pit.

The second reason was modelling control. For a cylindrical pit, the removed volume is calculated directly as $V_{pit} = \pi r^2 h$.

This gives a clear relationship between pit radius, pit depth and removed volume. It also allows the achieved mass loss to be checked without ambiguity.

After trial modelling of more complex pit forms such as conical pits, the cylindrical pit shape was retained because the random pit field had to be cut, meshed and analysed repeatedly. If that geometry produces repeated mesh failure or distorted elements in a dense pitted coupon, however, it is not suitable for the production workflow of this thesis. Robustness and reproducibility form part of the modelling justification, and they form part of the limitation of this thesis as well.

From a mechanical point of view, the cylindrical pit is treated as a conservative idealisation. A flat-bottomed cylindrical pit removes material over a constant area and introduces a sharper geometric discontinuity than a rounded semi-ellipsoidal pit or a tapering conical pit of equal removed volume. This idealisation may therefore promote earlier local plastic strain at the pit edge, consistent with the reduced apparent strain hardening observed in some pitted simulations.

The use of cylindrical pits does not imply that natural corrosion pits are cylindrical. Natural pits are irregular and may take rounded, tapered or asymmetric shapes. The cylinder serves here as a convenient, robust and conservative idealisation for a mass-loss-controlled finite element workflow. This thesis intends a comparison between the uncorroded coupon and mass-loss-equivalent pitted geometries analysed under the same material law, rather than a reconstruction of the exact natural pit morphology.

5.4 Element Type and Mesh Selection

The pitted coupon geometry contains many local cavities with curved surfaces. A structured hexahedral mesh would be difficult to apply to this geometry because the mesh would need to conform to many small circular pit boundaries while maintaining acceptable element quality. For this reason, a free tetrahedral mesh was adopted for the production pitted models.

Second-order quadratic tetrahedral elements, C3D10, were selected for the production simulations. This element type was chosen in preference to the modified tetrahedral element, C3D10M, because C3D10M produced negative-mass and excessive-distortion errors in the strongly distorted regions around the pits in this study. C3D10 was also chosen in preference to the linear tetrahedral element, C3D4, because linear tetrahedra can behave overly stiffly in plasticity-dominated problems and may suffer from locking.

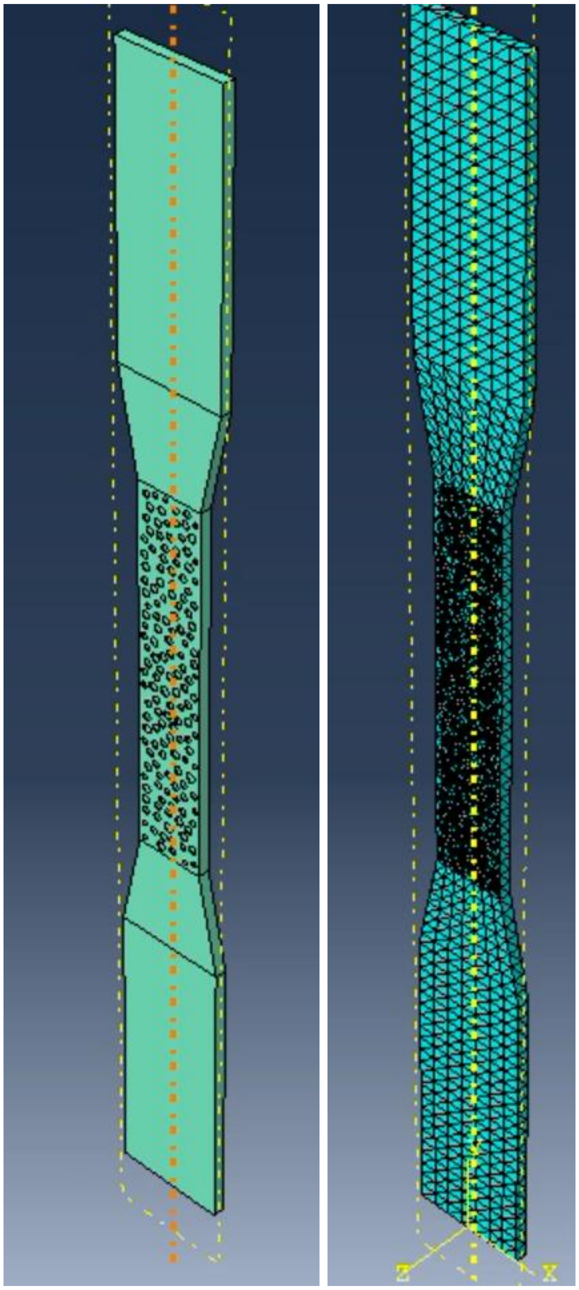

Figure 5.3 – *Typical C3D10 meshing of a corroded pitting model in ABAQUS*

The production mesh used a global seed size of approximately 2.25 mm with curvature-based refinement. A maximum curvature deviation factor of 0.15 was used so that the mesh refined around the circular pit mouths. A minimum element size of 0.3 of the global size was specified, giving a minimum element size of approximately 0.675 mm. This allowed the mesh to refine around the pit surfaces while keeping the bulk of the coupon sufficiently economical for repeated simulations.

The mesh was generated using the free meshing technique with tetrahedral element shape and the default Abaqus tetrahedral meshing algorithm. A conservative interior element-growth rate of 1.05 was used. This allowed the element size to increase gradually from the refined pit region into the coarser bulk material. Limiting the growth rate reduced abrupt changes in element size, which can produce poor element shapes and reduce the stable time increment in Abaqus/Explicit. Mapped triangular meshing was permitted on bounding faces where the surface geometry allowed it.

A mesh-convergence study on the uncorroded Day 0 model was done to check the adequacy of the selected mesh. The global seed size was varied in this study, and both hexahedral C3D8 and tetrahedral C3D10 discretisations were compared, as summarised in Table 5.6. The predicted ultimate tensile strength varied by only a few percent across the mesh densities and element families considered, indicating that the strength response was sufficiently mesh-converged at the production seed size. The production mesh, using a 2.25 mm global seed and C3D10 elements, was therefore adopted as a balance between numerical accuracy and computational cost.

The one-face pit insertion strategy also supported the meshing requirements of the model. Multi-face pit insertion in a thin coupon would create more severe local geometric discontinuities and could produce very small remaining ligaments between opposing pits. Poor-quality tetrahedral elements, local distortion and unstable damage localisation would become more likely as a result. The adopted one-face approach therefore provided a more robust basis for comparing different mass-loss and pit-distribution cases.

It is noted that the fracture strain predicted by an element-deletion damage model can remain mesh dependent even when the ultimate strength has converged. For this reason, the mesh-convergence assessment is used primarily to justify the strength response. Fracture strain and toughness are interpreted mainly as comparative trends between models rather than as exact absolute predictions. The convergence measure presented in Table 5.6 should be explicitly defined as being based only on the ultimate tensile strength. The mesh sensitivity of the predicted fracture strain and toughness was not assessed separately in this study. Consequently, fracture strain and toughness are used in the subsequent analysis as comparative trend indicators between models analysed using the same mesh configuration, rather than as fully mesh-converged absolute quantities.

Global seed (mm)	C3D8 hexahedral UTS (MPa)	C3D10 tetrahedral UTS (MPa)
1.00	726.9	- (run did not complete due to excess distortion of elements)
1.50	727.2	726.8
2.25 (production)	743.4	721.1
3.00	725.6	728.9

Table 5.6. *Mesh-convergence study on the uncorroded Day-0 model: predicted ultimate tensile strength versus global seed size for linear hexahedral (C3D8) and quadratic tetrahedral (C3D10) elements. The predicted UTS is within approximately 3% across the range, indicating convergence; the C3D10 element at a 2.25 mm seed with curvature control was adopted for production.*

Additional mesh trials were carried out using the pitted Day 42 geometry. These trials examined different global seed sizes, minimum element-size factors and curvature controls. A finer 2.0 mm global seed with stricter curvature control did not improve the elastic-to-plastic transition and increased post-fracture oscillation. Increasing the minimum element-size factor also did not improve the hardening response. The selected mesh setting, with a 2.25 mm global seed, a 0.3 minimum size factor and a curvature deviation factor of 0.15, was therefore retained as the best practical balance between geometric resolution and numerical stability.

The remaining difference between the pitted finite element curve and the Day 0 curve was not treated as a mesh-density problem. Since several mesh settings produced similar plateau behaviour, the flatter hardening response was interpreted mainly as a consequence of pit-induced strain localisation and the cylindrical pit idealisation.

For reproducibility, the complete set of meshing controls used in the production model is summarised in Table 5.5.

Mesh setting	Value / setting	Reason / basis
Element family / type	Standard library, C3D10 ten-node quadratic tetrahedron	Curved pit cavities prevent practical use of a structured hexahedral mesh. The quadratic tetrahedron provides improved accuracy compared with linear tetrahedra and avoids the over-stiff response associated with C3D4 elements.
Element shape / technique	Tetrahedral (Tet), free meshing	Allows the mesh to conform to the dense and irregular pitted geometry.
Meshing algorithm	Default tet algorithm; standard interior growth	Applied consistently across all corroded realisations using the standard Abaqus meshing controls.
Interior element-growth rate	1.05	Gradual element-size transition from the pit walls to the bulk; preserves element quality and the stable time increment
Approximate global seed	2.25 mm	Selected from the mesh-convergence study as a practical balance between accuracy and computational cost.
Curvature control (max. deviation factor)	Maximum deviation factor of 0.15	Automatic refinement around the curved pit mouths
Minimum element size	0.3 × global seed ≈ 0.675 mm	Sets the lower bound on element size in highly curved regions.
Mapped tri meshing on bounding faces	Enabled	Imposes well-shaped surface triangles that seed a higher-quality interior mesh

Table 5.7. *As-built mesh controls for the production model (Abaqus/CAE 2026, educational edition), as applied through the Global Seeds and Mesh Controls dialogs. The approximate global seed, curvature-deviation factor and minimum-size factor are the converged values identified in Table 5.4; the quadratic tetrahedron (C3D10) was adopted for the reasons given in the text.*

5.5 Loading, Boundary Conditions and Solution Scheme

The tensile test was simulated in Abaqus/Explicit as a quasi-static analysis. One gripped end of the coupon was fully restrained and the other was displaced axially through a coupled reference point, so that the applied elongation and the corresponding reaction force could be recovered directly as the reference-point displacement (U2) and reaction force (RF2). A monotonic axial displacement of the order of the experimental elongation (a prescribed reference-point displacement U2 = 10 mm over the modelled length, corresponding to about 0.20 engineering strain over the 50 mm gauge length, L_0) was applied smoothly over the step. Engineering stress and strain were then computed from the reaction force and displacement using the original gauge area (A_0 = 25 mm²) and gauge length (L_0 = 50 mm), so that the simulated and measured curves are defined consistently.

An explicit dynamic solver was chosen in preference to an implicit static solver. The analysis involves progressive element deletion and severe local distortion at the pits. An explicit scheme is more robust under these conditions and avoids the convergence difficulties that element removal causes in an implicit solution. Mass scaling was applied with a target stable time increment of 1×10^{-5} s to make an explicit, inherently dynamic, solver efficient for a quasi-static problem.
Only the pre-fracture part of the load-displacement curve is used to assess quasi-static behaviour for the explicit analysis. The specimen unloads rapidly after fracture or a major load drop, and the remaining fragments can vibrate. Oscillations after this point are numerical consequences of dynamic unloading and element deletion. They are not used to define UTS, fracture strain or toughness. The curve is therefore interpreted up to the first major loss of load-carrying capacity.

The extraction of engineering stress and strain from RF2 and U2 also helps maintain consistency with the experiment. Stress is calculated using the original gauge area A0, rather than the local net section at a pit, because the experimental engineering stress is based on original area. Net-section stress may be useful as a supplementary local measure, but it is not used for the main experimental comparison.
The as-built step, constraint and boundary-condition settings are collected in Table 5.6. The analysis uses a single explicit dynamic step (“Step-1”, procedure Dynamic, Explicit) of unit time

period with geometric nonlinearity active (Nlgeom = On), the latter being mandatory because the coupon undergoes large plastic strains, necking and finite rotation of the failing ligaments, for which a small-strain formulation would be invalid. Adiabatic heating is not included, consistent with the room-temperature, rate-independent, isothermal idealisation adopted for the material card at the quasi-static rates modelled here the heat generated by plastic work does not materially alter the response and including it would introduce a thermal coupling that the experiment does not isolate.

The explicit analyses used automatic stable time incrementation. Since the stable increment in Abaqus/Explicit is controlled by the smallest local element size, the refined mesh around the pit boundaries produced very small time increments. Mass scaling was therefore introduced to improve computational efficiency while preserving quasi-static behaviour. The acceptability of the scaled analyses was assessed through the energy-history outputs, including ALLKE, ALLIE, ALLAE, ETOTAL, and DMASS.

The linear and quadratic bulk-viscosity parameters are left at the Abaqus defaults of 0.06 and 1.2 respectively. Bulk viscosity in Abaqus/Explicit is a numerical device that damps the highest-frequency element "ringing" and, through the quadratic term, prevents elements from collapsing under very strong compressive shocks; the default values are calibrated by the code for general use and introduce negligible artificial damping at the quasi-static loading rates modelled here.

Load is introduced through a single kinematic coupling constraint ("Constraint-1") that ties the loaded end-face of the coupon to a reference point (RP-1) on the loading axis, with all six degrees of freedom (U1, U2, U3, UR1, UR2, UR3) coupled and the influence radius set to the outermost point of the region. A kinematic coupling makes the coupled face behave as a rigid loading clamp driven by the single reference point, which both reproduces the action of a testing-machine grip and provides a clean location at which to read the work-conjugate axial reaction force (RF2) and displacement (U2) for the engineering stress–strain curve. Concentrating the load and the output at one reference point is what makes the reaction-force history a direct analogue of the load cell and avoids the need to integrate tractions over a deforming surface.

Two boundary conditions complete the model. BC-1 fully encastres the opposite (fixed) end of the coupon (ENCASTRE, U1 = U2 = U3 = UR1 = UR2 = UR3 = 0), reproducing the stationary grip and providing the reaction against which the specimen is stretched. BC-2 prescribes the motion of the reference point: in the initial step all six components are held, and in Step-1 the axial component is released to a prescribed value while the remaining five components are held at zero, so that the loaded end translates purely along the loading axis without lateral drift or rotation. The prescribed axial displacement is applied through a smooth-step amplitude ("Amp-1") rather than as a step change, so that the velocity and acceleration of the loaded end rise and fall smoothly; a smooth (tabular or smooth-step) amplitude is the recommended way to keep an explicit analysis quasi-static, because it avoids the sudden acceleration that would launch stress waves and inflate the kinetic energy, and it is the practical mechanism by which the kinetic-to-internal energy ratio is kept well below one per cent. The constraint and boundary conditions are shown on the model in Figure 5.1.

Setting	Value	Reason
Step / procedure	Step-1; Dynamic, Explicit; time period 1	Robust with element deletion and severe distortion
Geometric nonlinearity	Nlgeom = On	Large strain, necking and finite rotation
Adiabatic heating	Not included	Isothermal, rate-independent idealisation
Incrementation	Automatic; global estimator; improved Dt; max increment unlimited; time scaling 1.0	Conditional stability of explicit solver
Bulk viscosity (linear, quadratic)	0.06, 1.2 (defaults)	Damps high-frequency ringing; negligible at quasi-static rate
Coupling (Constraint-1)	Kinematic; face → RP-1; U1–U3, UR1–UR3 coupled	Rigid loading clamp; clean RF2/U2 read-out
BC-1 (fixed end)	ENCASTRE (all DOF = 0)	Stationary grip / reaction
BC-2 (loaded end), initial	All DOF = 0	Reference point fixed before loading
BC-2 (loaded end), Step-1	U2 = 10 mm via amplitude Amp-1; U1 = U3 = UR1 = UR2 = UR3 = 0	Pure axial elongation; smooth ramp keeps analysis quasi-static

Table 5.8. *As-built step, coupling and boundary-condition settings for the explicit tensile analysis. The prescribed axial displacement (U2 = 10 mm) corresponds to an applied engineering strain of*

about 0.20 over the 50 mm gauge length (L_0), sufficient to carry the most ductile case through ultimate load and final separation; it is applied smoothly through amplitude Amp-1 and verified to be quasi-static in Section 5.6.

5.5.1 Output Extraction and Post Processing

The output requests were selected to support three main tasks. These were construction of the engineering stress-strain curve, verification of quasi-static behaviour and interpretation of the deformation mechanism.

The engineering stress-strain curve was obtained from history output at the loaded reference point. The axial reaction force (RF2) and axial displacement (U2) were recorded at 200 intervals. Engineering stress was calculated from ($RF2/A_0$), where ($A_0 = 25$) mm², and engineering strain was calculated from ($U2/L_0$), where ($L_0 = 50$) mm for comparison with the experimental gauge length.

Whole-model energy history output was also requested to verify the quasi-static nature of the explicit analysis. The internal energy (ALLIE), kinetic energy (ALLKE), total energy (ETOTAL) and added mass from mass scaling (DMASS) were recorded. The ratio of kinetic energy to internal energy was used to check that the response remained quasi-static before fracture. The added mass was also checked to confirm that mass scaling did not dominate the physical response.

Field output was requested to interpret the deformation and failure mechanism. The main variables used were stress (S), displacement (U) and element status (STATUS). (STATUS) was used to show element deletion and to identify the development of the fracture path through the pitted gauge region.

Request	Domain / frequency	Variables	Purpose
F-Output-1 (field)	Whole model, 20 intervals	S, U, STATUS	Stress contours, strain localisation and element deletion
H-Output-1 (history)	Loaded Reference-point set "rp"; 200 intervals	RF2, U2	Load-displacement and engineering stress-strain curve
H-Output-2 (history)	Whole model; 200 intervals	ALLIE, ALLKE, ALLAE, ETOTAL, DMASS	Quasi-static verification and mass-scaling check

Table 5.9. *Field and history output requests used for post-processing and quasi-static verification.*

5.6 Quasi-Static Verification

Two checks confirm that the explicit, mass-scaled solution represents a quasi-static response rather than a dynamic one, and that mass scaling does not contaminate the result. The mass-scaling target was verified first by repeating a representative analysis with the target stable time increment reduced by two orders of magnitude, from 1×10^{-5} s to 1×10^{-6} s. The predicted load-displacement response was essentially unchanged. This confirmed that the added, scaled mass is small enough not to affect the result and that the solution is insensitive to the time increment within this range.

The energy balance of the analysis was monitored throughout loading as the second check. The artificial hourglass energy ALLAE remained negligible. The ratio of kinetic energy ALLKE to internal energy ALLIE stayed well below 1% during loading. The internal energy ALLIE increased smoothly, and the total energy ETOTAL remained essentially constant. A kinetic-to-internal energy ratio of this order is the standard criterion for a quasi-static explicit analysis.

Together, these checks, summarised in Table 5.10, establish that the simulated tensile response is quasi-static and free of significant artificial energy. The response is also independent of the mass-scaling parameters. Differences between models can therefore be attributed to geometry rather than to numerical artefacts.

Verification check	Criterion	Outcome
Mass-scaling sensitivity	Load-displacement response remains essentially unchanged when the target stable time increment is reduced. Response invariant to 100× change in target time increment	Satisfied
Kinetic / internal energy	(ALLKE/ALLIE) remains well below 1% during pre-fracture loading	Satisfied
Artificial energy	Artificial energy remains negligible compared with internal energy	Satisfied
Internal energy ALLIE	Smooth, monotonic increase	Satisfied
Total energy ETOTAL	ETOTAL remains stable during the pre-fracture response, with changes occurring after damage/localisation.	Satisfied

Table 5.10. *Quasi-static verification checks for the explicit, mass-scaled tensile analysis. Typical energy histories are shown in Figures 5.4 to 5.7.*

Run ID	***ALLAE***	***ALLIE***	***ALLKE***	***ALLKE/ALLIE***	***ALLKE/ALLIE <1%?***
Day 14 Cyl1	*0*	*125000*	*90*	*0.072%*	*Yes*
Day 14 Cyl2	*0*	*123000*	*85*	*0.069%*	*Yes*
Day 14 Cyl3	*0*	*123000*	*85*	*0.069%*	*Yes*
Day 14 Cyl4	*0*	*123000*	*125*	*0.102%*	*Yes*
Day 21 Cyl1	*0*	*121000*	*80*	*0.066%*	*Yes*
Day 21 Cyl2	*0*	*118000*	*80*	*0.068%*	*Yes*
Day 21 Cyl3	*0*	*121000*	*125*	*0.103%*	*Yes*
Day 21 Cyl4	*0*	*120000*	*100*	*0.08%*	*Yes*
Day 28 Cyl1	*0*	*115000*	*80*	*0.07%*	*Yes*
Day 28 Cyl 2	*0*	*121000*	*90*	*0.07%*	*Yes*
Day 28 Cyl3	*0*	*121000*	*125*	*0.10%*	*Yes*
Day 28 Cyl4	*0*	*119000*	*100*	*0.08%*	*Yes*
Day 35 Cyl1	*0*	*121000*	*80*	*0.07%*	*Yes*
Day 35 Cyl2	*0*	*111000*	*100*	*0.09%*	*Yes*
Day 35 Cyl3	*0*	*119000*	*90*	*0.08%*	*Yes*
Day 35 Cyl4	*0*	*121000*	*90*	*0.07%*	*Yes*
Day 42 Cyl1	*0*	*121000*	*90*	*0.07%*	*Yes*
Day 42 Cyl2	*0*	*118000*	*100*	*0.08%*	*Yes*
Day 42 Cyl3	*0*	*118000*	*150*	*0.13%*	*Yes*
Day 42 Cyl4	*0*	*115000*	*125*	*0.11%*	*Yes*
4% Mass Loss Cyl1	*0*	*90000*	*70*	*0.08%*	*Yes*

4% Mass Loss Cyl2	*0*	*90000*	*70*	*0.08%*	*Yes*
4% Mass Loss Cyl3	*0*	*105000*	*60*	*0.06%*	*Yes*
4% Mass Loss Cyl4	*0*	*102500*	*90*	*0.09%*	*Yes*
6% Mass Loss Cyl1	*0*	*78000*	*70*	*0.09%*	*Yes*
6% Mass Loss Cyl2	*0*	*79000*	*45*	*0.06%*	*Yes*
6% Mass Loss Cyl3	*0*	*79000*	*80*	*0.10%*	*Yes*
6% Mass Loss Cyl4	*0*	*79000*	*80*	*0.10%*	*Yes*
8% Mass Loss Cyl1	*0*	*45000*	*65*	*0.14%*	*Yes*
8% Mass Loss Cyl2	*0*	*55000*	*100*	*0.18%*	*Yes*
8% Mass Loss Cyl3	*0*	*65000*	*70*	*0.11%*	*Yes*
8% Mass Loss Cyl4	*0*	*55000*	*60*	*0.11%*	*Yes*
10% Mass Loss Cyl1	*0*	*34000*	*50*	*0.15%*	*Yes*
10% Mass Loss Cyl2	*0*	*48000*	*100*	*0.21%*	*Yes*
10% Mass Loss Cyl3	*0*	*45000*	*100*	*0.22%*	*Yes*
10% Mass Loss Cyl4	*0*	*52500*	*125*	*0.24%*	*Yes*
12% Mass Loss Cyl1	*0*	*50000*	*60*	*0.12%*	*Yes*
12% Mass Loss Cyl2	*0*	*55000*	*55*	*0.10%*	*Yes*
12% Mass Loss Cyl3	*0*	*55000*	*100*	*0.18%*	*Yes*
12% Mass Loss Cyl4	*0*	*67500*	*125*	*0.19%*	*Yes*

Table 5.10A. *Summary of quasi-static verification checks for the explicit, mass-scaled tensile analysis with the checks for ALLAE and ALLKE/ALLIE ratios. All runs satisfied.*

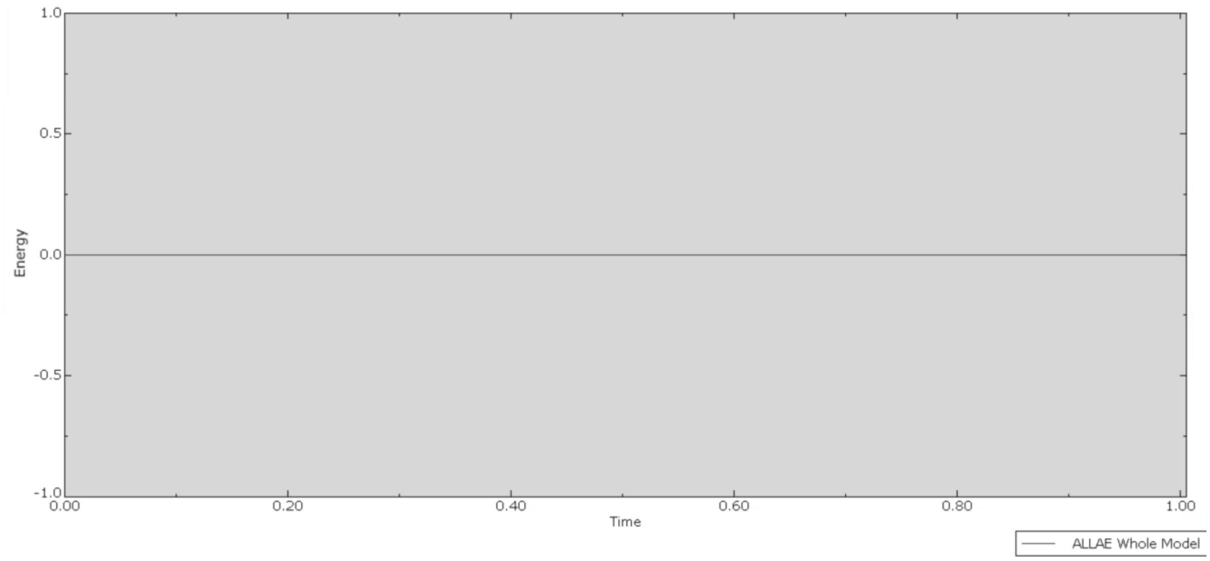

Figure 5.4 – *Typical ALLAE plot with no artificial energy detected*

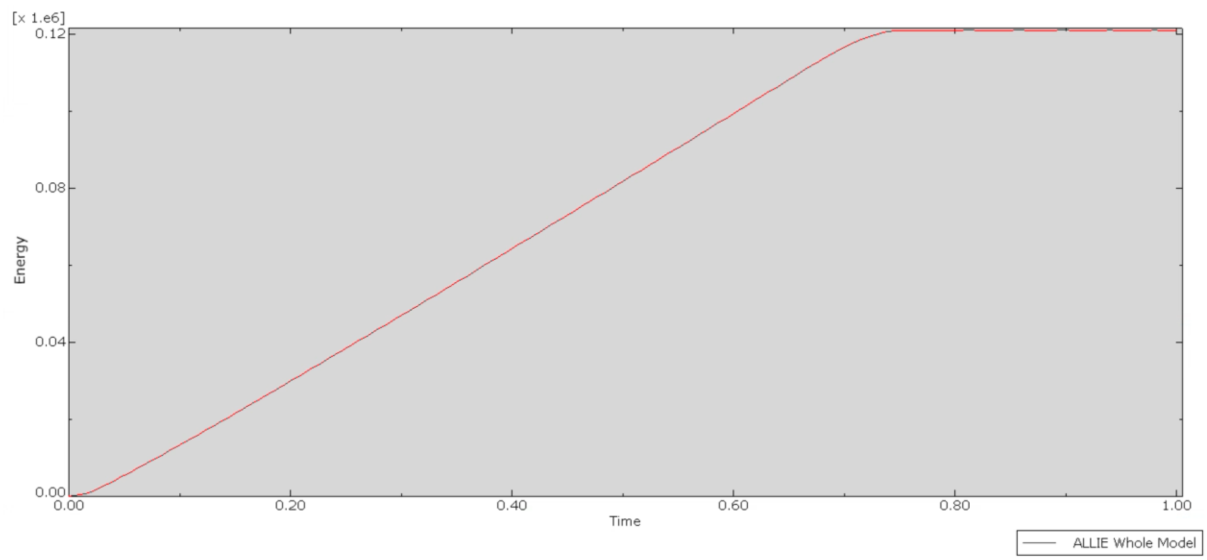

Figure 5.5A - *Typical ALLIE plot – smooth monotonic increase*

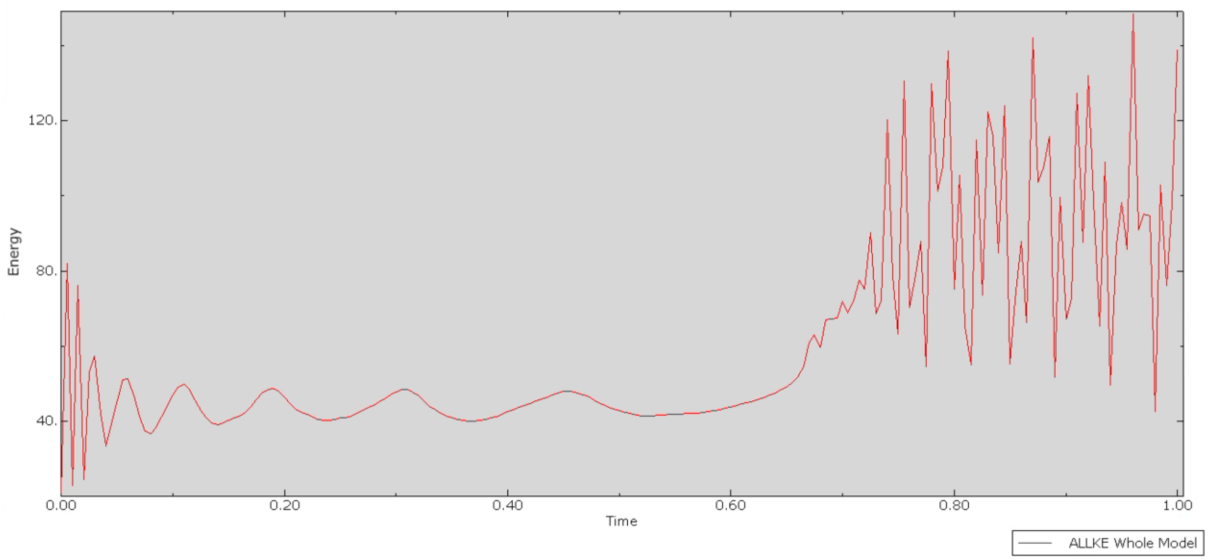

Figure 5.5B - *Typical ALLKE plot - in small magnitude of less than 1% of ALLIE*

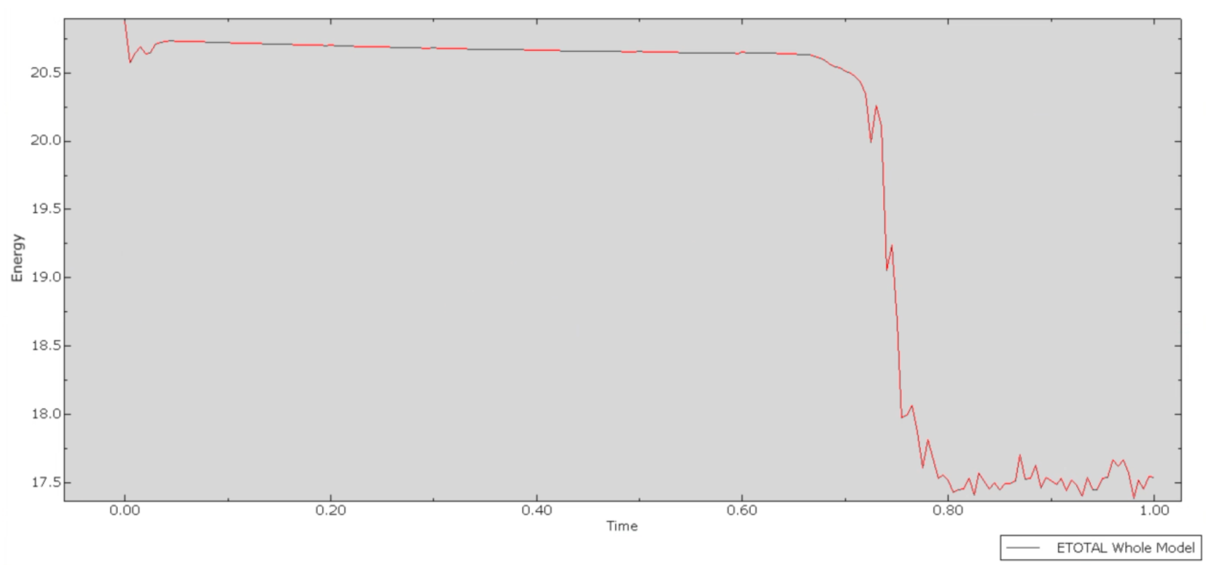

Figure 5.6 - *Typical ETOTAL Plot stable during the pre-fracture*

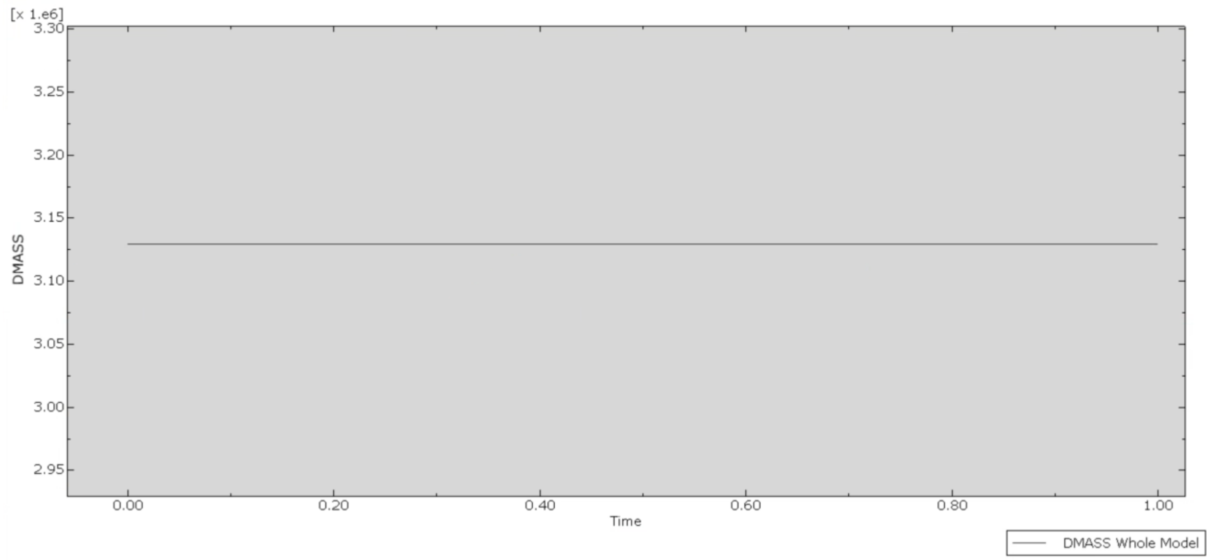

Figure 5.7A - *Typical DMASS Plot stable during the pre-fracture*

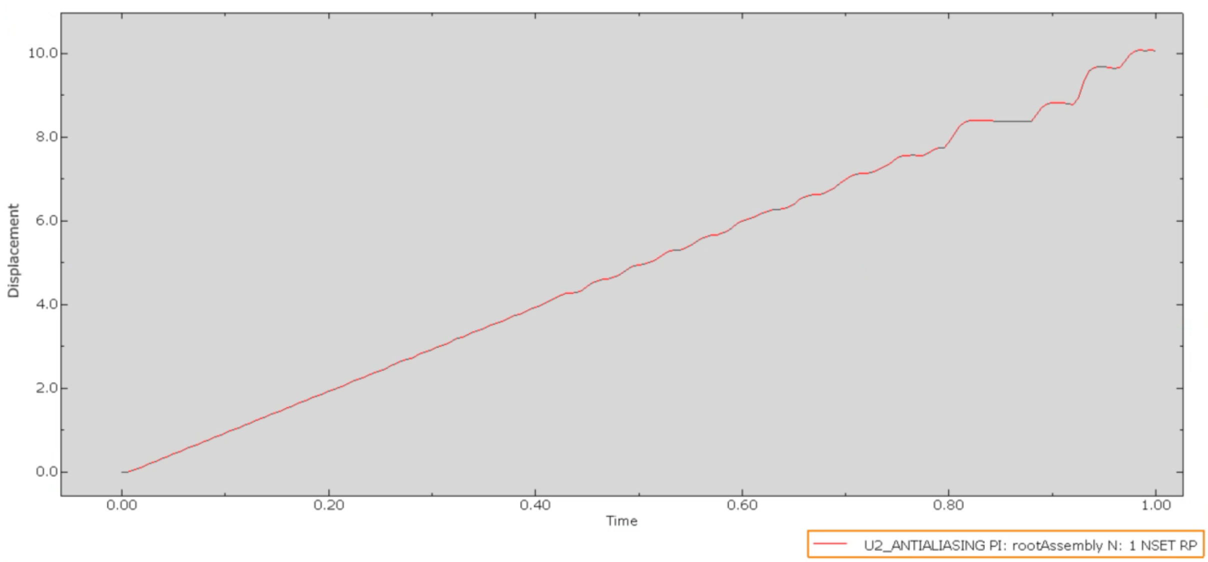

Figure 5.7B - *Typical U2 Displacement Plot almost linearly increasing during the displacement load*

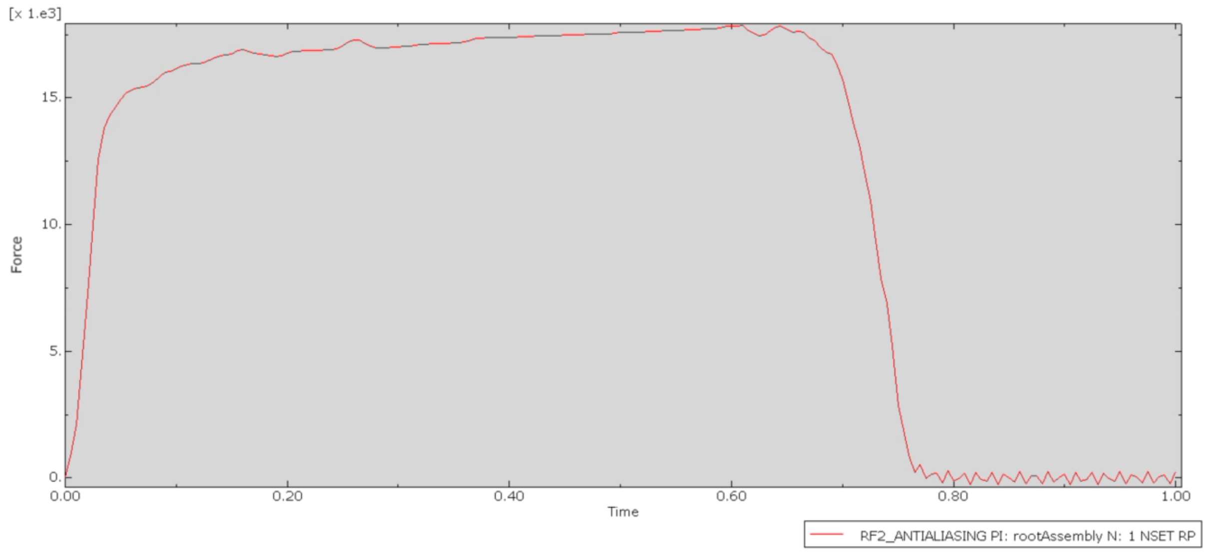

Figure 5.7C - *Typical RF2 Plot showcasing the elastic response, strain hardening and fracture curve of a steel coupon sample.*

5.7 Methodological Justification of the Abaqus workflow

The Abaqus workflow rests on a sequence of linked modelling checks rather than on a single assumption. Each stage was designed to control one part of the modelling process and to make the numerical response traceable.

The Day 0 coupon was used first to establish the baseline material response. This was the most appropriate calibration case, since the uncorroded specimen was unaffected by pit geometry. The material card obtained from this calibration was then kept fixed for all corroded simulations. This step prevented the model from mixing geometric corrosion effects with assumed changes in steel strength or hardening.

Corrosion was introduced second through a mass-loss-equivalent pit field. The pit field was generated in MATLAB, checked through its achieved removed volume, and transferred to Abaqus using a Python cutting script. The pitted geometry was therefore neither manually drawn nor arbitrary. Each pit had a recorded coordinate, radius and depth, and the total removed volume could be checked against the target mass loss. This forms the main reproducibility feature of the workflow.

The mesh was selected third using convergence and sensitivity checks rather than visual judgement alone. For the smooth Day 0 model, the ultimate tensile strength was checked against mesh density and element type. The pitted models also had to satisfy the practical requirement of stable meshing around many cylindrical pits. The final mesh was therefore chosen as a balance between convergence, geometric resolution and numerical robustness. Later mesh refinements did not remove the flatter pitted hardening response, which supports the interpretation that the remaining difference stems mainly from pit-induced strain localisation rather than from mesh density.

The explicit analysis was verified fourth as a quasi-static tensile simulation. Smooth displacement loading was used, post-fracture oscillations were excluded from interpretation, and the kinetic energy was checked against the internal energy before fracture. These checks mattered because Abaqus/Explicit was selected for its robustness with element deletion and local distortion, yet the pre-fracture response still needed to represent a quasi-static tensile test rather than a dynamic event.

5.8 Assessment of the finite-element workflow

This section assesses the finite element workflow against the experimental data presented in Chapter 4. The assessment first establishes the uncorroded Day 0 baseline, which is used to calibrate the material model and check the predicted tensile response. Examination is next for the corroded cases from Day 14 to Day 42. The comparison is framed carefully because the experimental results showed that, within the measured low mass-loss range, the corrosion effect is smaller than the coupon-to-coupon scatter identified in Section 4.2.

The assessment is therefore divided into two levels. Material calibration forms the first level, performed using the smooth Day 0 coupon. This case suits calibration because it remains unaffected by pit geometry. Mechanistic assessment forms the second level, performed using the corroded pitted geometries. The aim for the corroded cases is not to force the numerical curve to match every experimental curve exactly. Each experimental coupon carries its own unmeasured corrosion morphology, local pit distribution and material scatter. An exact match to one corroded curve would not, therefore, necessarily prove that the model is physically correct.

The purpose of the corroded case comparison instead is to determine whether the model produces the expected mechanical mechanism. This mechanism is local pit-induced strain localisation, expected to affect deformation-related quantities more strongly than UTS. The comparison therefore focuses on the predicted strength response, the overall shape of the stress-strain curve, and the trend of deformation-related quantities such as fracture strain and toughness. Absolute fracture strain is interpreted cautiously, as it is affected by the element-deletion damage model and retains some mesh dependence.

5.8.1 Uncorroded baseline (Day 0)

The Day 0 uncorroded coupon was used for material calibration because it provides the clearest representation of the base steel response. Since this coupon contains no corrosion pits, its tensile behaviour is governed by the bulk material properties and the nominal specimen geometry. The calibration is therefore not affected by assumptions about pit shape, pit distribution or corrosion severity. The Day 0 condition is also the least affected by corrosion-related scatter and provides a single well-defined target curve for calibrating the elastic response, plastic hardening and ductile-damage parameters.

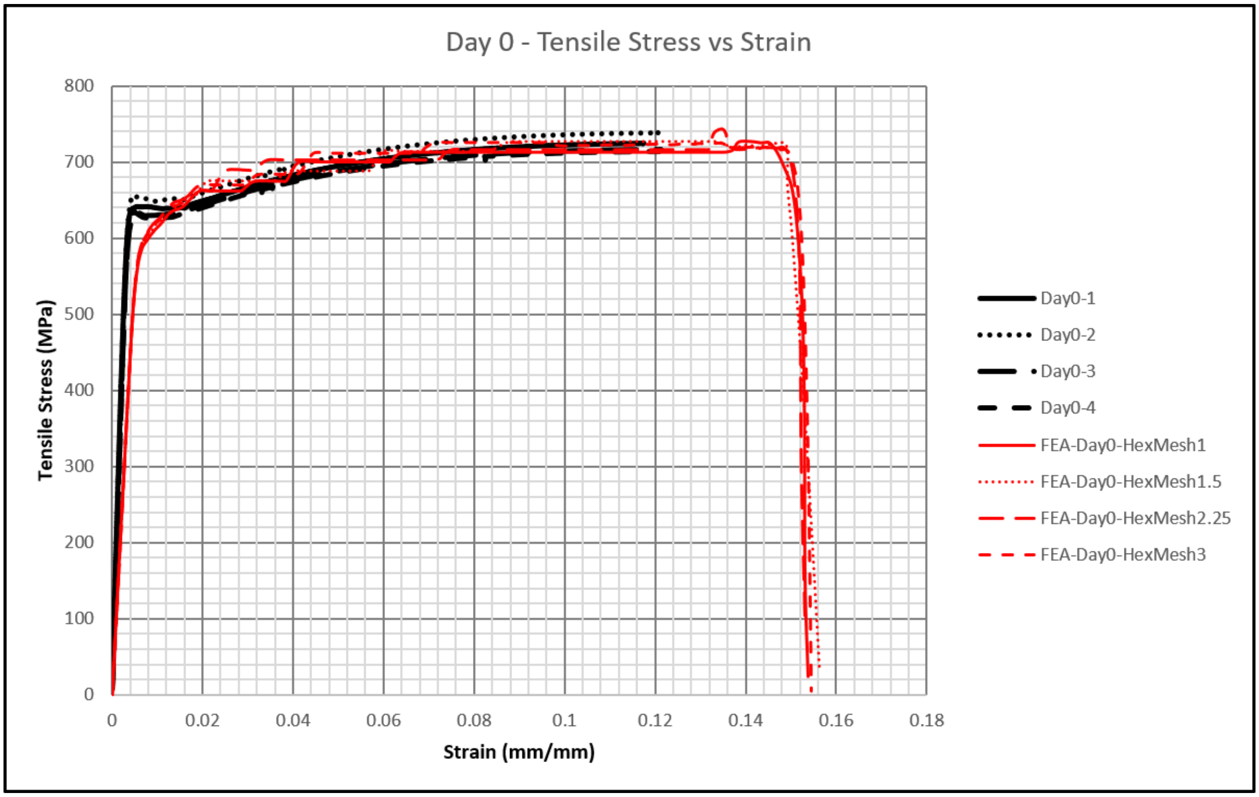

Figure 5.8. - *Comparison of Tensile Stress for Day 0 Experimental Coupon Test Results versus FEA Base Models for Day 0 with Meshing Sensitivity Study done for Mesh Sizes for C3D4 Tetrahedral element meshing*

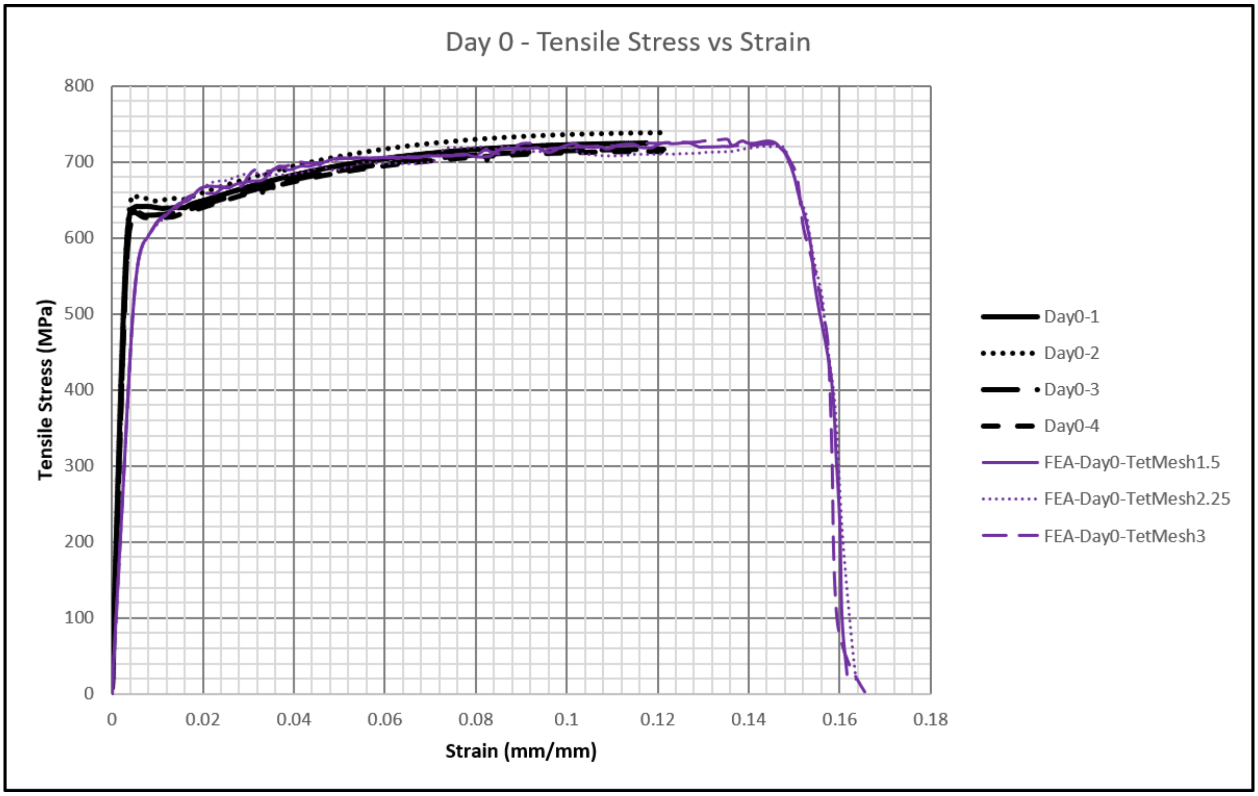

Figure 5.9. - *Comparison of Tensile Stress for Day 0 Experimental Coupon Test Results versus FEA Base Models for Day 0 with Meshing Sensitivity Study done for Mesh Sizes for C3D10 Tetrahedral element meshing*

Calibrating the material model using a corroded case would be less appropriate because the measured response would already include the effects of pit geometry and local strain concentration. Any fitted material card would then become specific to one corrosion state and one pit morphology. By calibrating the material model only against the Day 0 response and then keeping it fixed for all corroded simulations, the later comparisons isolate the effect of pitted geometry.

The FE workflow was assessed primarily against the overall stress–strain response and ultimate tensile strength. Fracture strain and toughness are treated as comparative indicators because they are more sensitive to the damage parameters and mesh setting.

The model is therefore treated as quantitatively reliable for ultimate tensile strength and for the general shape of the pre-fracture stress-strain response. Fracture strain and toughness are interpreted more cautiously, serving mainly as comparative trends between the uncorroded and pitted models rather than as exact absolute predictions. This interpretation aligns with the literature position that strength is generally predicted more reliably in finite element models of corroded steel, while ductility-related quantities remain more sensitive to modelling assumptions [3].

5.8.2 Corroded cases (Day 14 to Day 42)

The Day 0 agreement is very close, with the finite element prediction differing from the experimental group mean by approximately 0.4%. The material properties remain unchanged to isolate the pit geometry effects. Pitted models are then stochastically generated and analysed in ABAQUS to observe the tensile responses of the pitted models.

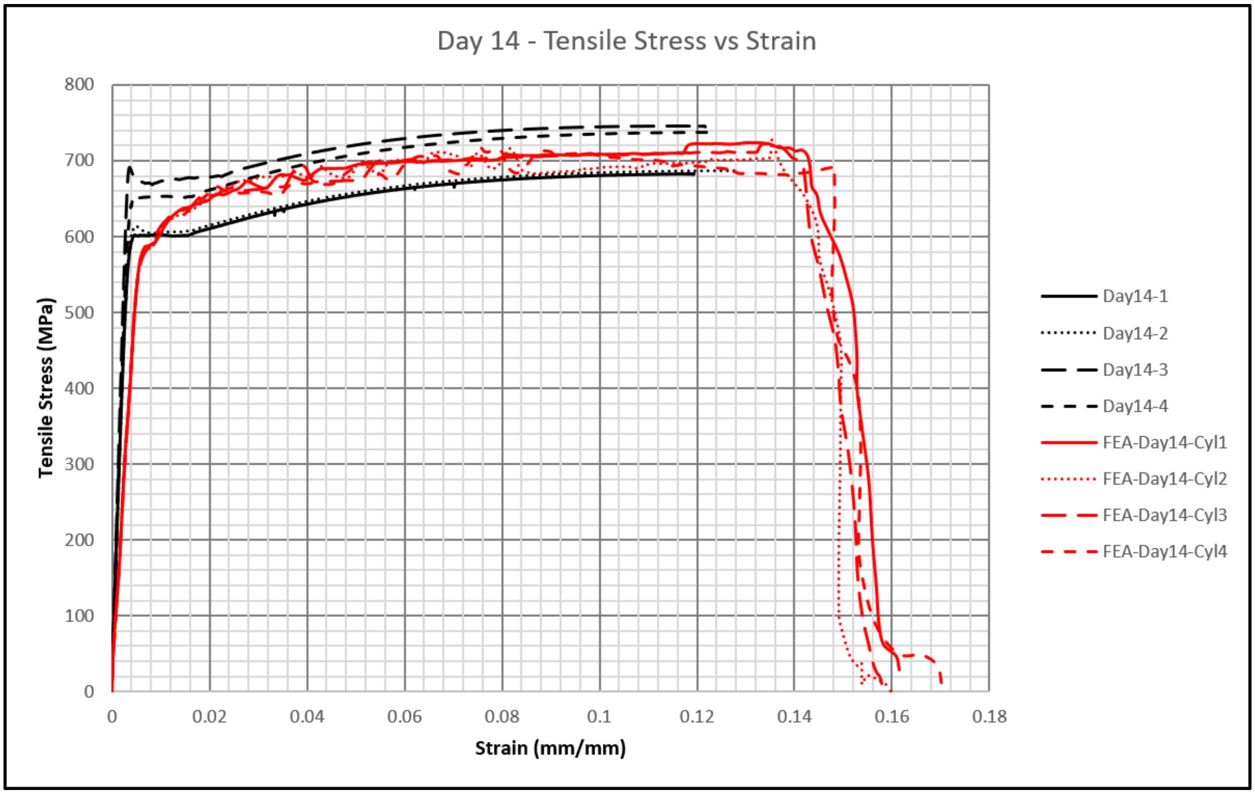

Figure 5.10. - *Comparison of Experimental vs FEA Pitted Models for Day 14 Exposure*

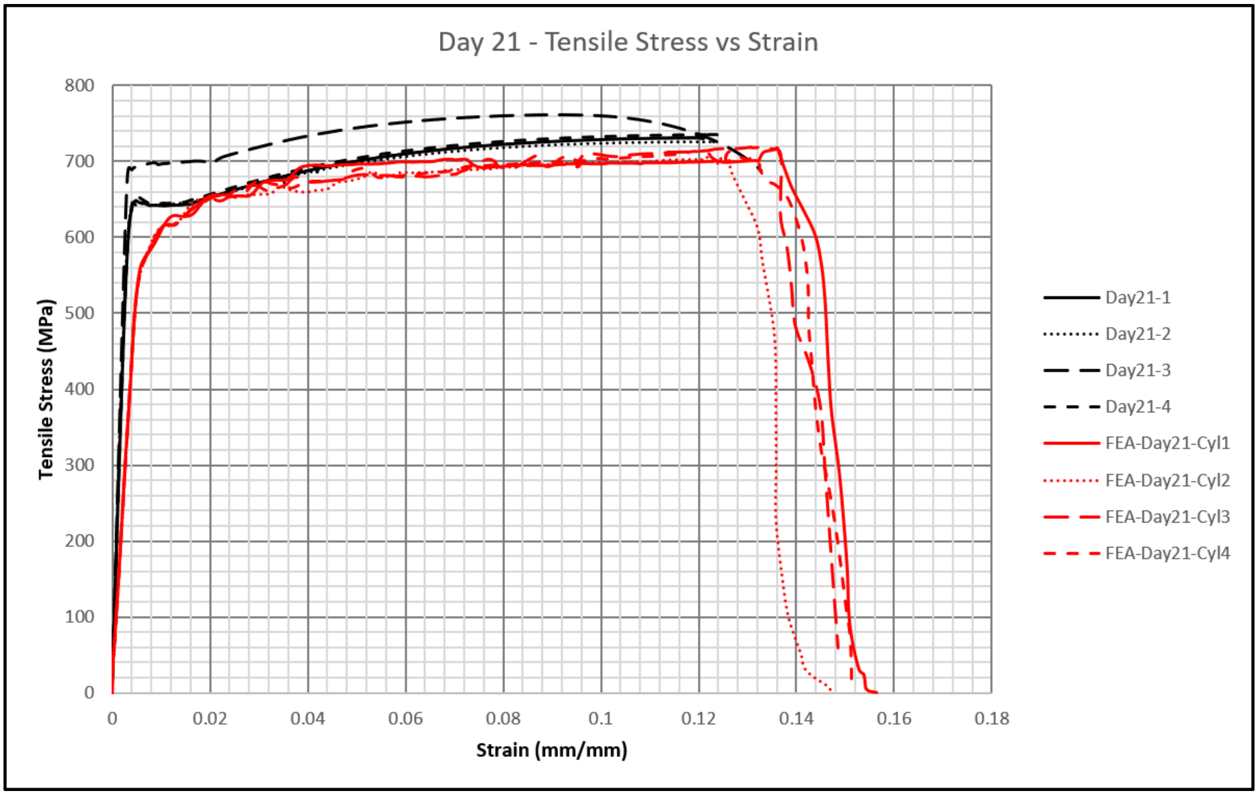

Figure 5.11. - *Comparison of Experimental vs FEA Pitted Models for Day 21 Exposure*

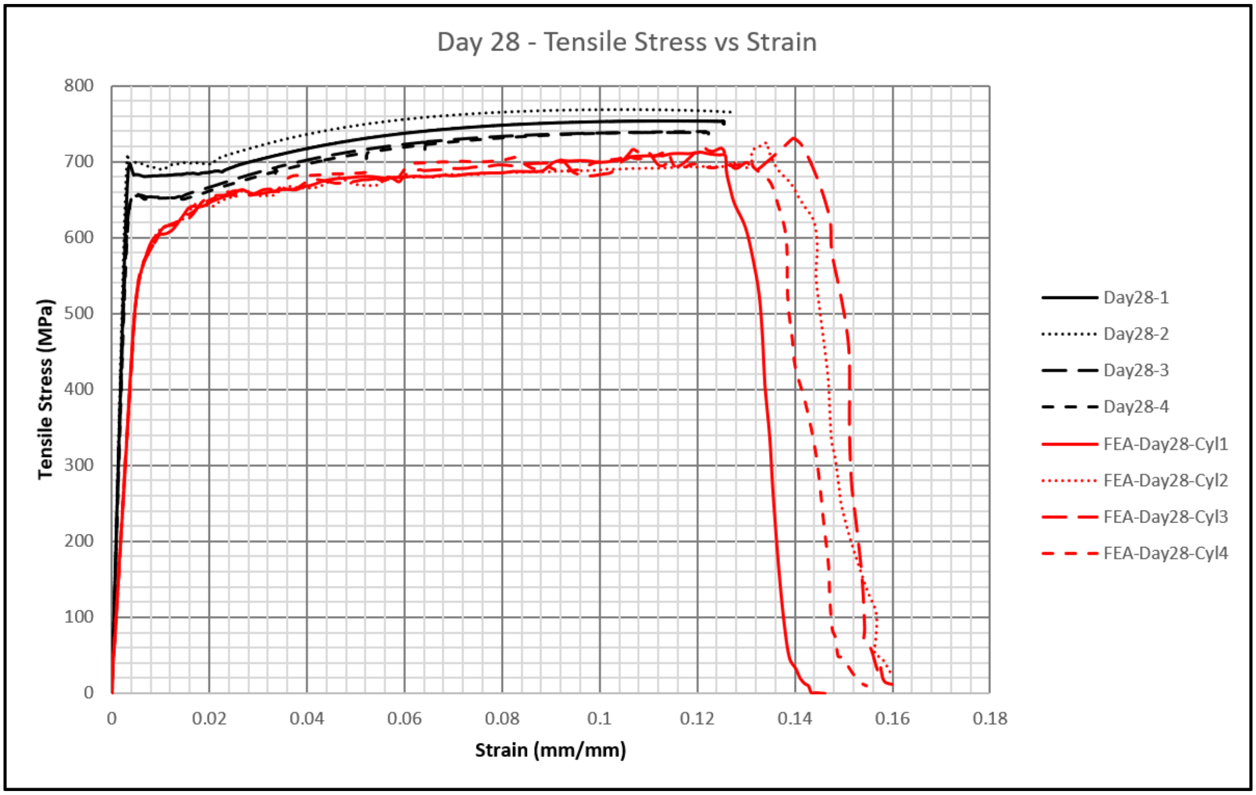

Figure 5.12. - *Comparison of Experimental vs FEA Pitted Models for Day 28 Exposure*

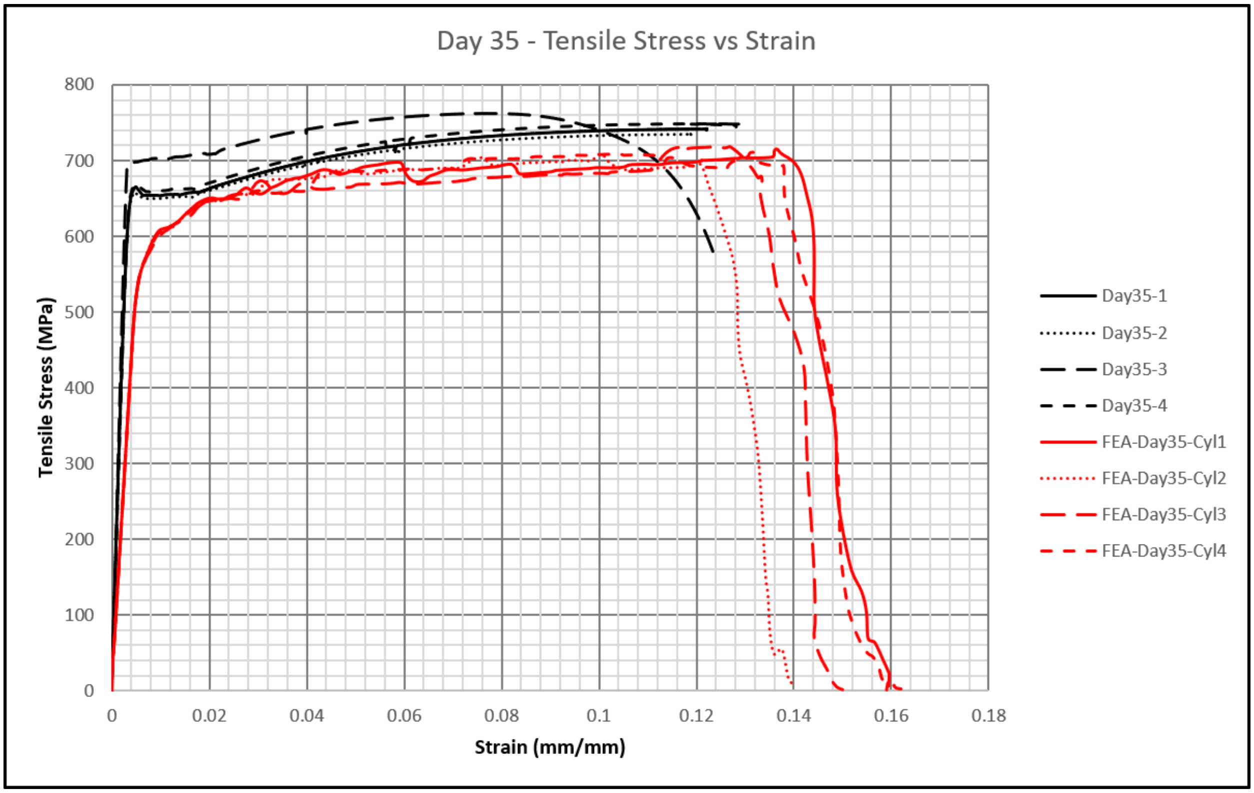

Figure 5.13. - *Comparison of Experimental vs FEA Pitted Models for Day 35 Exposure*

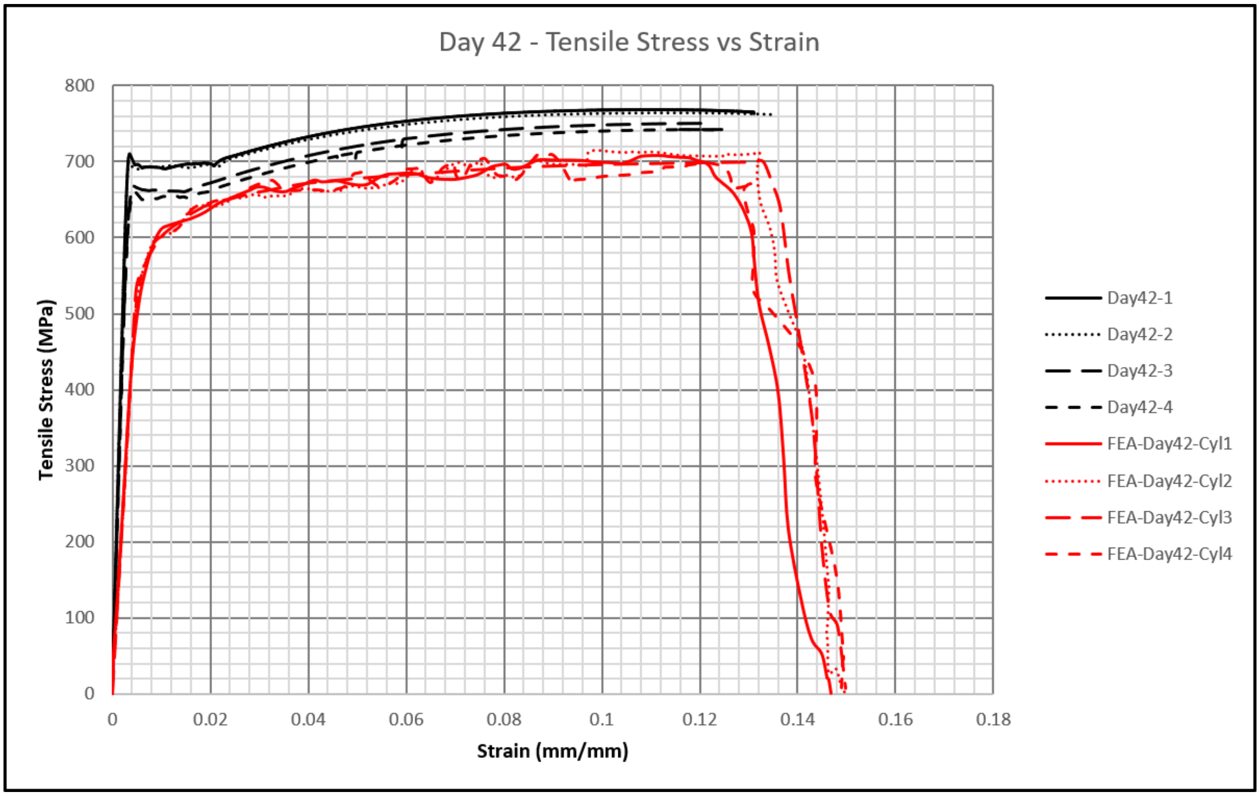

Figure 5.14. - *Comparison of Experimental vs FEA Pitted Models for Day 42 Exposure*

For the corroded exposure groups, the comparison shows a clear difference between the experimental trend and the finite element trend. The experimental group-mean UTS does not decrease with exposure. Instead, it varies upward and reaches 756.2 MPa at Day 42. This upward variation is not interpreted as corrosion-induced strengthening, because corrosion is not expected to increase the tensile strength of the steel but discussed as a scatter. The differences between exposure groups are of the same order as the within-group scatter. For example, the Day 14 standard deviation is ±32.6 MPa. Therefore, the experimental UTS values at this low mass-loss range should not be interpreted as a statistically clear corrosion trend.

The finite element model cannot reproduce this experimental upward variation, since the same material card is used for every exposure case. This is intentional. The model isolates the geometric effect of pitting by keeping the steel material properties fixed and changing only the pit geometry. The finite element results therefore represent a controlled numerical comparison rather than a reproduction of coupon-to-coupon material scatter. The difference between the model and the experiment at later exposure ages reflects the difference between a real experimental dataset affected by material variability and a numerical model that isolates corrosion geometry.

Exposure	Average Δm for gauge section (%)	Experimental UTS (MPa)	FE Mean UTS (MPa)	Difference (%)
Day 0 (baseline)	0	723.8 ± 10.9	721.1	-0.4
Day 14	1.29	713.0 ± 32.6	722.8 ± 4.1	+1.4
Day 21	1.74	738.3 ± 15.8	714.5 ± 5.1	-3.2
Day 28	1.94	750.4 ± 13.8	720.4 ± 8.6	-4.0
Day 35	2.20	746.6 ± 11.4	713.2 ± 4.3	-4.5
Day 42	2.49	756.2 ± 12.2	707.8 ± 6.4	-6.4

Table 5.11. *Comparison between experimental and finite element ultimate tensile strength. Experimental values are reported as group mean ± standard deviation. The percentage mass loss is referenced to the exposed gauge-section mass. The close Day 0 agreement confirms the material calibration. The increasing difference at later exposure ages reflects experimental scatter and the use of a fixed material card in the finite element model.*

The finite element UTS results should not be interpreted as a strictly linear or monotonic degradation trend. Although the total removed volume increases with exposure, UTS is not controlled by mass loss alone. It is also affected by the local pit distribution, the deepest pits, the spacing between pits and whether the most severe pits occur near the critical tensile section. Because the pitted surfaces are generated stochastically, two models with different mass-loss levels may still have similar peak loads if the critical pit arrangement is less severe in one case. Conversely, a lower mass-loss case may show a slightly lower UTS if the random pit field produces a more critical local ligament.

The Day 14 and Day 28 FE UTS values fail to follow a smooth decreasing sequence for this reason. Rather than a linear strength-loss curve, the FE UTS values are better understood as a narrow scatter band with a weak downward tendency at the highest mass loss. At Day 42, the lowest mean FE UTS occurs, with a predicted value of 707.8 MPa against 721.1 MPa for the Day 0 baseline.

This amounts to a reduction of approximately 1.8%. Within the low mass-loss range considered in this thesis, then, pitting exerts only a limited effect on peak tensile strength.

A clearer corrosion response emerges in the deformation-related quantities. Table 5.12 summarises the finite element predictions for UTS, fracture strain and toughness. From 0.160 at Day 0 to 0.142 at Day 42, the predicted fracture strain falls by approximately 11%. Predicted toughness follows a similar pattern, dropping from 107.5 MJ/m³ to 92.0 MJ/m³, a reduction of roughly 14%. Although not perfectly linear either, the toughness values show an overall reduction far clearer than the change observed in UTS.

Exposure	Δm based on gauge section (%)	FE UTS (MPa)	FE Strain ε_f (mm/mm)	FE toughness (MJ/m³)
Day 0 (baseline)	0	721.1	0.160	107.5
Day 14	1.29	722.8 ± 4.1	0.152 ± 0.002	100.9 ± 1.6
Day 21	1.74	714.5 ± 5.1	0.144 ± 0.006	94.7 ± 3.9
Day 28	1.94	720.4 ± 8.6	0.144 ± 0.007	94.8 ± 5.0
Day 35	2.20	713.2 ± 4.3	0.143 ± 0.008	93.3 ± 5.5
Day 42	2.49	707.8 ± 6.4	0.142 ± 0.003	92.0 ± 2.1

Table 5.12. *Finite element tensile properties for the uncorroded and pitted models. The FE UTS values for the corroded cases are reported as the mean ± standard deviation of four cylindrical pit realisations. The material card is held constant in all models, so the changes shown are caused by the generated pitted geometry. The fracture-strain and toughness values are the means of the four realisations; their per-realisation scatter was not separately tabulated.*

Exposure	Δm based on gauge section (%)	FE True UTS (MPa)	FE True Strain ε_f (mm/mm)	FE True Toughness (MJ/m³)
Day 0 (baseline)	0	836.5	0.148	107.5

Exposure	Δm based on gauge section (%)	FE True UTS (MPa)	FE True Strain ε_f (mm/mm)	FE True Toughness (MJ/m³)
Day 14	1.29	832.7 ± 4.9	0.141 ± 0.002	100.9 ± 1.6
Day 21	1.74	817.4 ± 7.2	0.135 ± 0.005	94.7 ± 3.9
Day 28	1.94	824.1 ± 11.1	0.135 ± 0.006	94.8 ± 5.0
Day 35	2.2	815.2 ± 7.5	0.134 ± 0.007	93.3 ± 5.5
Day 42	2.49	808.3 ± 7.6	0.133 ± 0.003	92.0 ± 2.1

Table 5.13. - *presents the post-processed true tensile properties obtained from the FE engineering stress–strain results. The corresponding true toughness was obtained by numerical integration of the converted true stress–true strain response. The true-property results show the same general trend as the engineering FE results, with only a small reduction in peak tensile capacity over the experimentally matched mass-loss range, but a clearer reduction in fracture strain and toughness.*

The calculated toughness remains effectively unchanged, even though the stress and strain values change after conversion from engineering to true quantities, since the standard engineering-to-true transformation preserves the area under the stress-strain curve. Apart from minor numerical integration differences, the toughness values in Table 5.13 are therefore numerically the same as those obtained from the engineering stress-strain response.

Mechanically, the difference between the strength response and the ductility response carries real significance. The remaining net section at low mass loss is still sufficient to carry a similar peak load. Local yielding around pits can also redistribute stress before the global maximum load is reached, and UTS remains relatively insensitive to small amounts of pitting as a result. The same pits, however, promote local plastic strain concentration and earlier damage development. Fracture strain and toughness are reduced more clearly by this than peak strength is. Any FE UTS value slightly above the Day 0 baseline is treated as numerical and morphology-induced scatter within an essentially unchanged strength response, rather than as a physical strengthening effect.

The simulated damage pattern lends support to this interpretation. High plastic strain and element deletion develop in the corroded models within the reduced ligaments near critical pits, not at an arbitrary location. The pitted geometry controls the local failure mechanism, this indicates.

Studying how corrosion morphology promotes strain localisation and reduces deformation capacity is well supported by the model on this basis, even though the absolute fracture strain is not reproduced exactly.

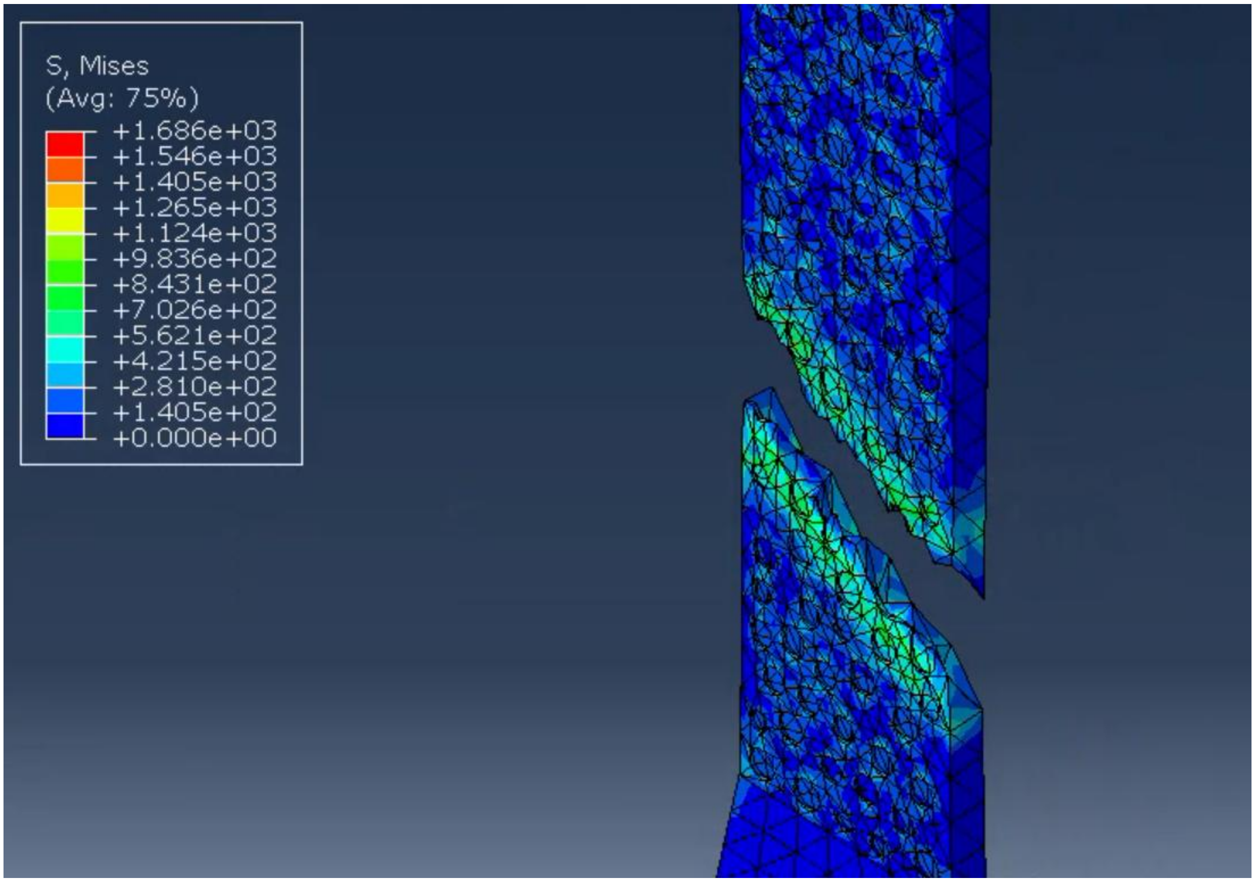

Figure 5.15 - *Sample fracture location and angle of corrosion pitted model.*

Overall, the assessment shows that the finite element workflow captures the main mechanical effect expected from pitting corrosion at low mass loss. The UTS response is weak and affected by morphology-induced scatter, while fracture strain and toughness provide clearer indicators of corrosion damage. For this reason, the later parametric discussion focuses not only on UTS but also on deformation-related quantities.

5.8.3 Comparison with published corroded steel studies

The produced results are consistent with the main findings reported in the corroded steel literature. The finite element results show that UTS is comparatively insensitive to the low mass-loss range considered in this study, while fracture strain and toughness are more strongly affected. This agrees with refined finite element studies of corroded steel, which show that ultimate strength is mainly governed by the critical pits and the remaining section, while ductility is more strongly controlled by residual thickness and strain localisation [3]. It is also consistent with damage-mechanics studies of corroded reinforcement, where corrosion reduces ductility and shortens the post-yield deformation capacity [6].

The present results also support the general finding that mass loss alone is not a complete descriptor of corrosion damage. Localised corrosion can be more damaging than uniform thickness loss at the same mass loss because pit depth, pit spacing, pit clustering and critical pit location influence the mechanical response [15], [16], [17]. This is reflected in the finite element results. The UTS values do not follow a strictly linear decreasing trend, because peak strength is affected by the stochastic pit arrangement as well as by the total removed volume. In contrast, fracture strain and toughness show a clearer overall reduction because they are more sensitive to local plastic strain concentration around pits.

The uncorroded model is confirmed as accurately calibrated, and the corroded models reproduce the expected mechanism of pit-induced strain localisation. The predictive relationships developed later in Chapter 6, however, are not explicitly validated against an independent experimental dataset. Derived from the geometry-isolated finite element results, these relationships are consistent in direction with the literature, though their numerical coefficients should be treated as provisional. Before the relationships could be applied more generally, additional steel grades, wider corrosion severities and independent assessment data would be required. A wider corrosion severity range has since been examined numerically through the higher-severity projection study (Section 5.10), though independent experimental data at higher severity remain necessary nonetheless before broader application becomes appropriate.

The earlier fracture predicted by the cylindrical pit models should therefore be interpreted as a conservative localisation response, not as a direct prediction that every exposed coupon must fail earlier than the Day 0 coupon. Material scatter and individual pit morphologies that were never directly scanned into the finite element model are present within the experimental coupons. The Abaqus model is best used, on this basis, to show that local corrosion geometry alone can reduce deformation capacity when the same calibrated material is given a mass-loss-equivalent pitted surface.

5.8.4 Summary of Assessment

The assessment supports the use of the finite element workflow as a controlled tool for studying the effect of pitting geometry. The uncorroded Day 0 model reproduced the experimental UTS with good accuracy. The predicted UTS was 721.1 MPa, compared with the Day 0 experimental mean of 723.8 MPa, giving a difference of approximately 0.4%. This confirms that the material calibration is suitable for the baseline response.

For the corroded cases, the experimental data did not show a clear corrosion-induced strength reduction. The group-mean UTS values were affected by coupon-to-coupon scatter and even increased with exposure in some cases. This upward variation was not interpreted as corrosion strengthening. Instead, it was attributed to material and testing scatter at low corrosion severity. The finite element model was not expected to reproduce this scatter because the same material card was intentionally retained for all exposure cases.

The geometric effect of pitting is isolated in the finite element results, with the material properties held constant. Only a weak and non-monotonic strength response emerges from the FE UTS values, accompanied by a small reduction at the highest mass loss. Peak tensile strength, within the low mass-loss range studied, is thus relatively insensitive to pitting, this indicates, and is instead affected by the stochastic arrangement of critical pits. Numerical and morphology-induced scatter within an essentially unchanged strength response, rather than a physical strengthening effect, is how any FE UTS value close to or slightly above the Day 0 baseline should be treated.

A clearer corrosion response is provided by the deformation-related quantities. As pit severity increases, the predicted fracture strain and toughness decrease more noticeably than UTS. The main mechanical interpretation of the thesis is supported by this finding: pitting corrosion affects tensile behaviour primarily by promoting local plastic strain concentration and reducing deformation capacity, rather than by causing a large reduction in peak tensile strength at low mass loss.

The model is therefore used in the remainder of the thesis as a controlled numerical workflow for examining the influence of mass loss and pit morphology. UTS is treated as a useful strength measure, but fracture strain and toughness are also examined because they are more sensitive to pitting damage. The absolute fracture strain is interpreted cautiously because it depends on the damage and element-deletion formulation, while the relative trends between uncorroded and pitted models are treated as the more reliable output.

5.9 Parametric Interpretation of the Finite Element Results

The simulations used in this section are the cylindrical-pit realisations described previously. Five corroded exposure levels were considered from Day 14 to Day 42, with four independent random realisations at each exposure level. The Day 0 model is used as the uncorroded baseline. The same material card is used for all models, so the differences in response are caused by geometry only. No material knockdown factor is applied.

The parametric interpretation is necessary because the experimental corrosion range is relatively low. Within this range, the experimental scatter can hide the effect of corrosion on global UTS. The numerical model allows the pitted geometry to be controlled and repeated, making it possible to examine trends that are difficult to observe directly from the experimental groups alone.

The finite element results should therefore be interpreted as a geometry-controlled extension of the experimental programme, not as a replacement for it. The experiment provides the material response, the exposure context and the observed scatter. The numerical model provides a way to isolate the effect of pitting geometry and to examine how mass loss and pit arrangement influence the tensile response.

5.9.1 Effect of Mass Loss

The effect of mass loss is examined by comparing the group-mean response across the exposure levels. The mass-loss ratio increases from 1.29% at Day 14 to 2.49% at Day 42 when referenced to the exposed gauge-section mass. The Day 0 model provides the uncorroded baseline. All twenty corroded finite-element simulations were successfully completed and included in the parametric interpretation. These consisted of four random pit realisations for each of the five exposure levels, and no converged analysis was omitted from the results. The only simulations excluded from the main interpretation were the conical-pit trial models, which were not retained due to numerical instability. Although post-fracture load oscillations were observed in some load–displacement responses, these oscillations were disregarded during interpretation and were not used as a basis for excluding any completed run.

The finite element results show that UTS is only weakly affected over this low mass-loss range. The FE UTS values do not decrease in a strictly linear or monotonic sequence. Day 14 is almost identical to the Day 0 baseline, and Day 28 remains close to the baseline.

A similar peak load can still be carried by the remaining section at low mass loss. Stress can also be redistributed by local yielding around pits before the global maximum load is reached. UTS is thus controlled not only by the total removed volume, but also by the location of the most critical pits and the remaining ligament at the eventual failure section. Morphology-induced scatter, rather than a true strengthening or a clean linear degradation law, is what a slightly higher or lower UTS at one exposure level therefore reflects.

A clearer effect of pitting appears in the deformation-related quantities. From 0.160 for the Day 0 baseline to 0.142 at Day 42, the FE fracture strain decreases, a reduction of approximately 11%. Toughness follows a similar path, falling from 107.5 MJ/m^3 to 92.0 MJ/m^3, corresponding to a reduction of roughly 14%. Larger than the change in UTS, these reductions indicate that pitting affects deformation capacity more strongly than peak tensile strength.

The mechanism discussed in Chapter 2 accounts for this behaviour. The pits become deeper as mass loss increases, and the local ligament between pits becomes more critical. Stronger plastic strain concentration around pit edges and pit roots results, not merely a small reduction in net section. Deformation capacity is therefore reduced before a large reduction in UTS is observed.

The pit-generation statistics support this interpretation. Across the exposure range, the mean pit depth increases from approximately 0.105 mm at Day 14 to approximately 0.201 mm at Day 42. The mean aspect ratio also increases from approximately 0.08 to approximately 0.15 over the same interval, while the mean pit count and pit width remain broadly similar. This indicates that the generated corrosion severity increases mainly through deeper and sharper pits rather than through a large increase in pit number.

Two engineering implications follow from this result. First, an assessment based only on residual strength may understate the effect of low-level pitting corrosion, because UTS changes only slightly while fracture strain and toughness reduce more clearly. Second, a strength reduction at low mass loss may be difficult to detect in physical tests because the change is small compared with ordinary coupon-to-coupon scatter. This is consistent with the experimental data in Chapter 4, where the measured UTS did not show a clear corrosion-induced reduction.

5.9.2 Effect of Pit Morphology at Matched Mass Loss

The influence of pit morphology was evaluated by comparing the four independent random realisations within each exposure group. For a given exposure level, all four models were generated to satisfy the same target mass loss, meaning that the total removed volume was held constant. As a result, any variation in the predicted tensile response within the same group is attributed to differences in pit size, pit depth, and spatial distribution, rather than to differences in overall material loss.

Since only four realisations were considered for each exposure level, the reported within-group standard deviations should be interpreted as indicative measures of morphology-induced variability. They are not intended to represent a full probabilistic assessment or Monte Carlo characterisation of the pit distribution. A larger number of random realisations would be required to define the scatter distribution with greater statistical confidence.

This result demonstrates why mass loss alone does not fully determine the tensile response. The total removed volume defines the average corrosion severity, but it does not define the critical local geometry. The response is influenced by the most critical section that forms during loading. This critical section depends on where the deepest pits are located, how closely neighbouring pits are spaced and whether several pits align across the tensile path. Therefore, two pit fields with the same mass loss can still produce different UTS, fracture strain and toughness.

Case Groups for Trend Across (ranked by number of pits, with Group 1 being highest nos. of pits in FEA models)	**Day 14**	**Day 21**	**Day 28**	**Day 35**	**Day 42**
Case Group 1	Cyl-1 with 144 pits	Cyl-1 with 147 pits	Cyl-4 with 149 pits	Cyl-3 with 148 pits	Cyl-1 with 151 pits
Case Group 2	Cyl-4 with 139 pits	Cyl-4 with 126 pits	Cyl-3 with 143 pits	Cyl-4 with 133 pits	Cyl-4 with 135 pits
Case Group 3	Cyl-2 with 119 pits	Cyl-3 with 115 pits	Cyl-2 with 112 pits	Cyl-1 with 127 pits	Cyl-2 with 125 pits
Case Group 4	Cyl-3 with 101 pits	Cyl-2 with 105 pits	Cyl-1 with 101 pits	Cyl-2 with 123 pits	Cyl-3 with 123 pits

Table 5.14. *Case grouping for trend analysis by ranking number of pits in each stochastic corroded pitting models across Day 14 to Day 42*

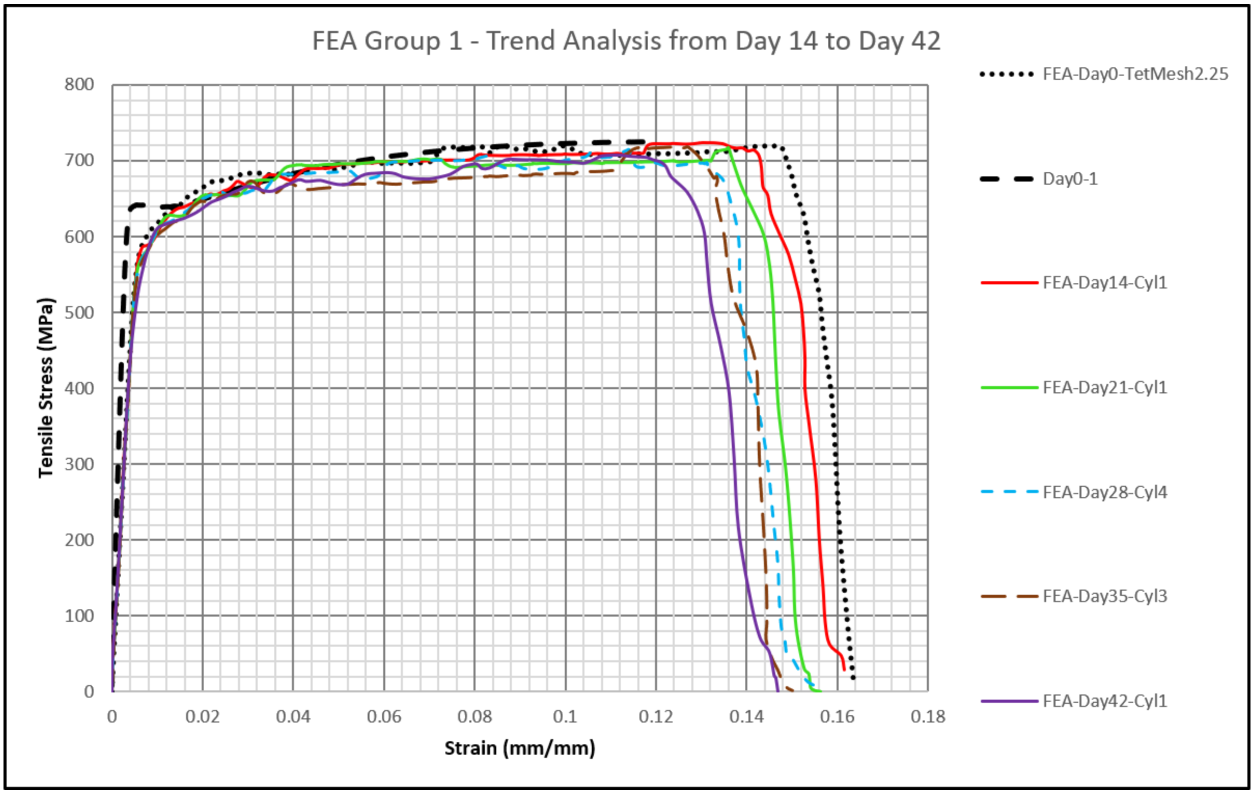

Figure 5.16. – *Trend Analysis for Grouping 1 of Day 14 to Day 42 comparison of Experimental Data vs FEA Pitted Models*

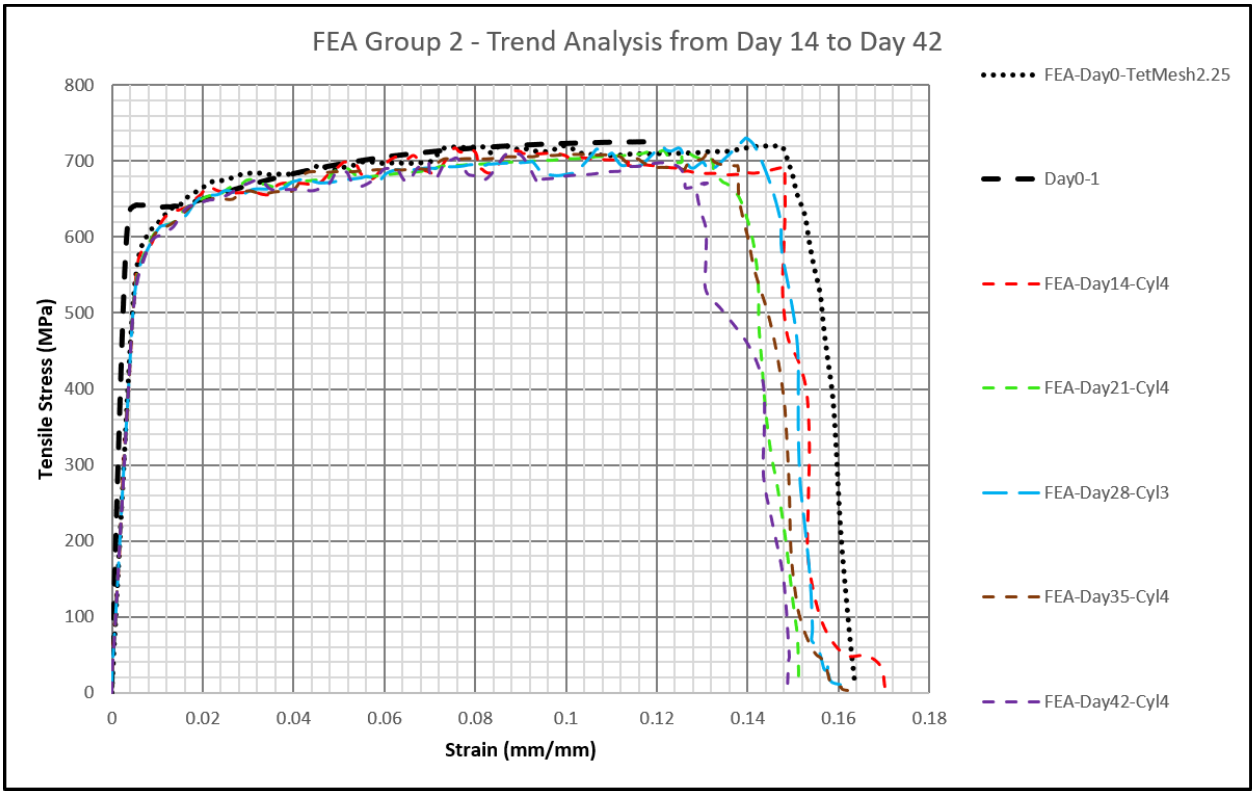

Figure 5.17. – *Trend Analysis for Grouping 2 of Day 14 to Day 42 comparison of Experimental Data vs FEA Pitted Models*

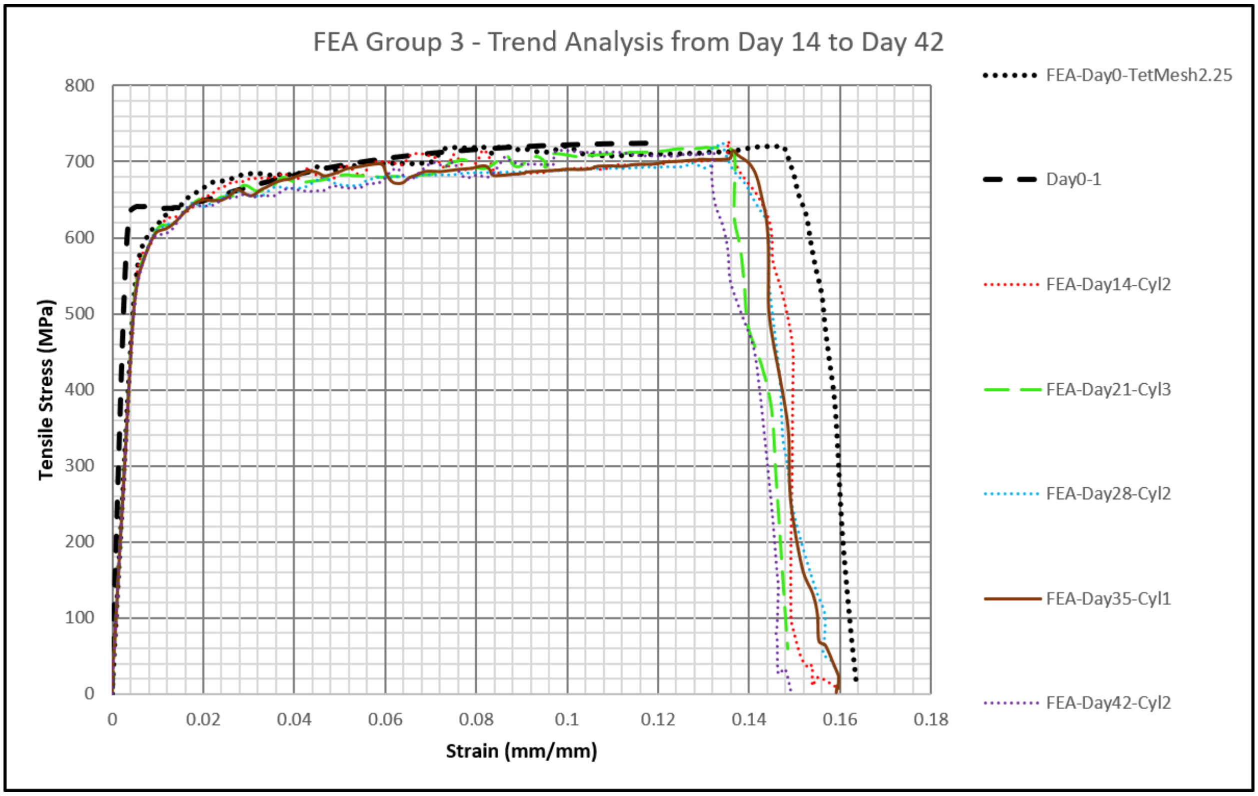

Figure 5.18. – *Trend Analysis for Grouping 3 of Day 14 to Day 42 comparison of Experimental Data vs FEA Pitted Models*

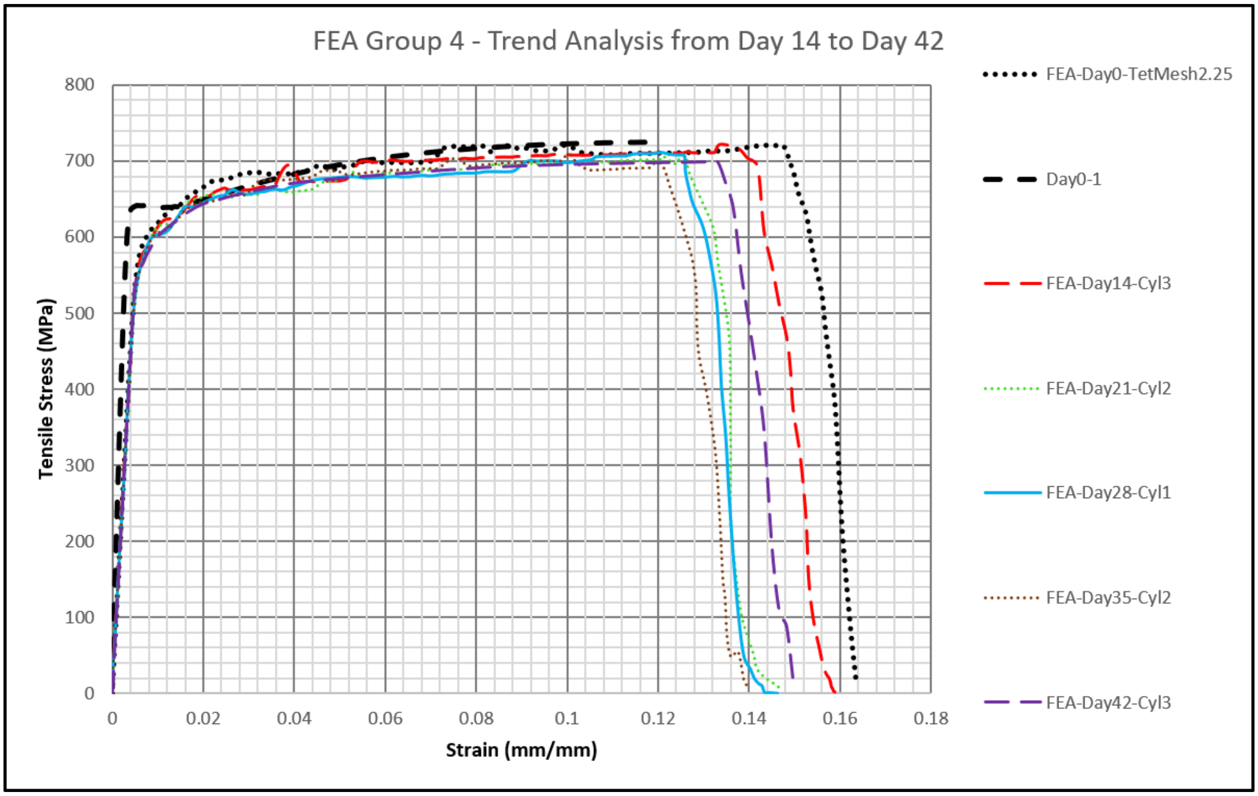

Figure 5.19. – *Trend Analysis for Grouping 4 of Day 14 to Day 42 comparison of Experimental Data vs FEA Pitted Models*

The grouped finite element stress-strain curves show that the pre-peak tensile response is broadly similar across the pitted models. The initial yielding and strain-hardening portions of the curves remain close to the uncorroded Day 0 response, indicating that the fixed material model gives a consistent global response and that the low mass-loss pitting has only a limited effect on the pre-peak behaviour.

The UTS values do not reduce in a smooth or monotonic sequence from Day 14 to Day 42. This is expected because the peak tensile load is not governed by exposure age or pit count alone. At the low mass-loss levels considered, the remaining net section is still able to carry a similar peak load, and local yielding can redistribute stress before final localisation. The results therefore support the interpretation that UTS is relatively insensitive to the generated pitting severity within the studied range.

The more significant difference between the models is observed in the post-peak response and the strain at which rapid load reduction occurs. Several pitted models show earlier softening and fracture than the uncorroded baseline, even though their UTS remains similar. This indicates that the main mechanical effect of pitting is a reduction in deformation capacity rather than a large reduction in peak strength.

The comparison also shows that pit count alone is not a sufficient morphology descriptor. The cases ranked with higher pit numbers do not consistently produce the lowest UTS or the earliest fracture. This is because, at a given target mass loss, a larger number of pits may correspond to a more distributed pit field, while a smaller number of pits may contain deeper or more critically located pits. The tensile response is therefore governed by the critical local pit arrangement, including pit depth, spacing, clustering and position relative to the eventual failure section.

Measurable scatter in the predicted tensile response is demonstrated overall by the grouped curves, introduced by the stochastic pit morphology. The random realisations are supported by this finding as more appropriate than a single deterministic pitted model. The main interpretation of the thesis is reinforced as well: average corrosion severity is defined by mass loss, but localisation behaviour and the resulting loss of ductility are controlled by pit morphology.

This is why the stochastic workflow proves useful. The same response would be assigned to all specimens with the same mass loss by a deterministic uniform-thickness model. The effect of random pit interaction would also be missed by a single-pit model. Not only how much material is removed, but also where it is removed, is captured by the present workflow as central to pitting corrosion.

Why the FE UTS values fail to follow a perfectly smooth decreasing trend with exposure is also explained by the morphology effect. A slightly less severe critical section at a higher mass loss, or a slightly more severe one at a lower mass loss, can be produced by the random pit field. The FE UTS response is therefore best interpreted as a narrow scatter band with a weak reduction at the highest mass loss, rather than as a linear UTS degradation curve.

The practical comparison of pit morphology in this thesis is limited to the robust cylindrical-pit family. Trial modelling of conical pits was carried out, but the conical models were numerically unstable and only one attempted case completed successfully. The conical case is therefore not treated as a full morphology result. The morphology effect quantified in this section refers to variation in pit size, depth and spatial arrangement within the cylindrical idealisation.

5.10 Higher-severity Mass Loss Projection Study

The simulations used for the experimental assessment in this thesis cover the measured corrosion range, up to approximately 2.49% mass loss when referenced to the exposed gauge-section mass, and the residual-property relationships of Chapter 6 are fitted within that experimentally matched range. To test whether the near-flat low-severity strength response continues at higher corrosion severity, and to characterise the higher-severity behaviour, a separate projected mass-loss study was carried out using the same calibrated, geometry-isolated finite-element workflow. This study extends the modelled severity well beyond the experimental range and is presented below. It is a numerical projection rather than an experimentally verified high-severity dataset, because the material card is held fixed and only the pitted geometry is changed.

Projected Mass loss	**N pits**	**Mean radius (mm)**	**Mean depth (mm)**	**Max depth range (mm)**	**Mean (h/t)**	**Max (h/t) range**	**Pit density (/100 mm²)**	**Pit-area ratio (%)**	**$S_{a,eq}$ (mm)**	**$S_{q,eq}$ (mm)**
4% (0.5102g)	128 ± 15	0.707 ± 0.040	0.320 ± 0.009	0.407–0.446	0.160 ± 0.004	0.204–0.223	17.39 ± 2.04	27.67 ± 0.79	0.0883 ± 0.0000	0.1713 ± 0.0025
6% (0.7654g)	124 ± 16	0.709 ± 0.040	0.490 ± 0.013	0.641–0.680	0.245 ± 0.006	0.320–0.340	16.85 ± 2.19	27.06 ± 0.50	0.1325 ± 0.0000	0.2598 ± 0.0024
8% (1.0205g)	127 ± 12	0.699 ± 0.024	0.653 ± 0.019	0.856–0.925	0.326 ± 0.010	0.428–0.462	17.29 ± 1.58	27.02 ± 0.63	0.1766 ± 0.0000	0.3475 ± 0.0046

10% (1.2756g)	126 ± 12	0.698 ± 0.026	0.823 ± 0.018	1.000–1.000	0.411 ± 0.009	0.500–0.500	17.15 ± 1.66	26.83 ± 0.56	0.2208 ± 0.0000	0.4335 ± 0.0038
12% (1.5307g)	130 ± 13	0.694 ± 0.033	0.979 ± 0.006	1.000–1.000	0.490 ± 0.003	0.500–0.500	17.63 ± 1.70	27.07 ± 0.20	0.2649 ± 0.0000	0.5098 ± 0.0016

Table 5.15: *Summary of generated pit morphology for the projected 4–12% cylindrical-pit FE models.*

5.10.1 Main Projection Results

In the projected study, five target gauge-section mass losses of 4, 6, 8, 10 and 12% were imposed, each realised with four independent stochastic cylindrical-pit fields, giving twenty additional finite-element analyses. As in the experimental-range models, the pit generator and the Abaqus pit-cutting script were unchanged, the depth scaling solved for each target removed volume exactly, so that the achieved mass loss equals the target, and the production mesh with a 2.25 mm global seed and C3D10 elements was retained.

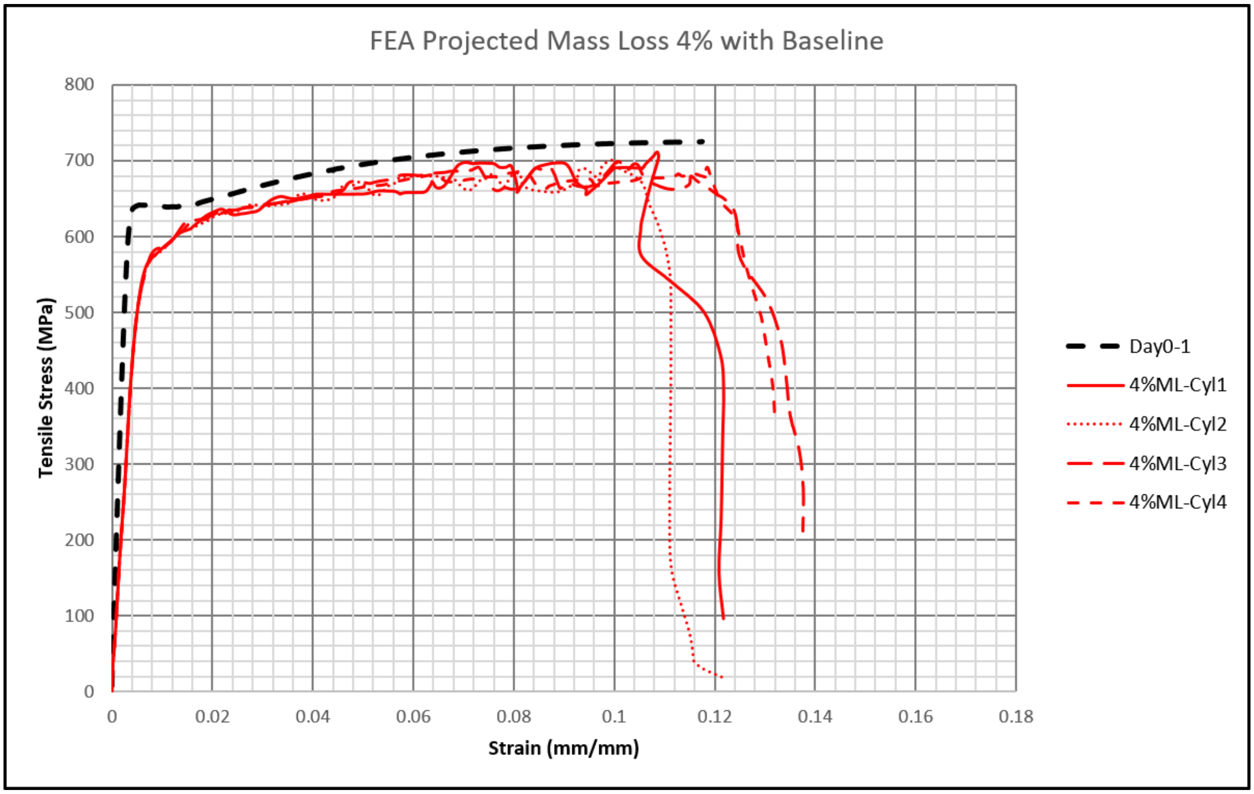

Figure 5.20. – *Comparison of 4 different stochastic pit realisations for FE against baseline Day 0 for tensile stress vs strain at mass loss 4% projection.*

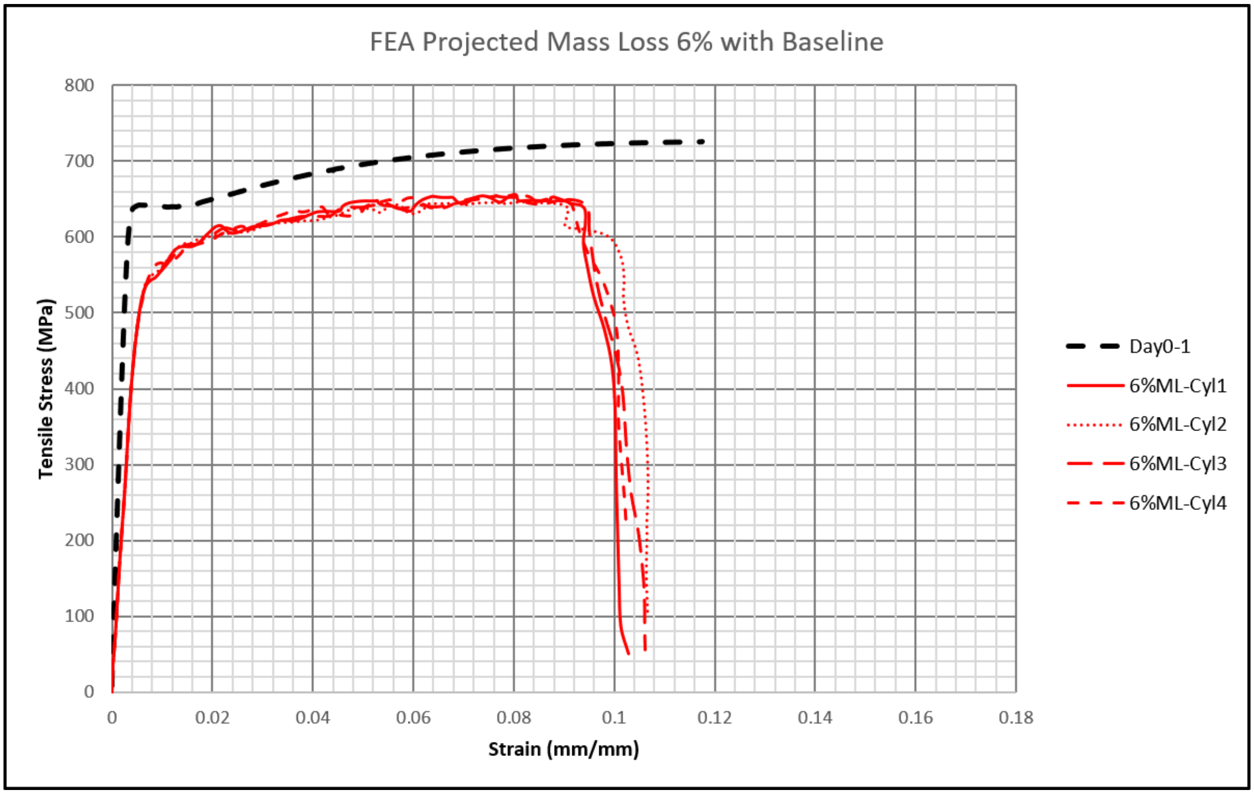

Figure 5.21. – *Comparison of 4 different stochastic pit realisations for FE against baseline Day 0 for tensile stress vs strain at mass loss 6% projection.*

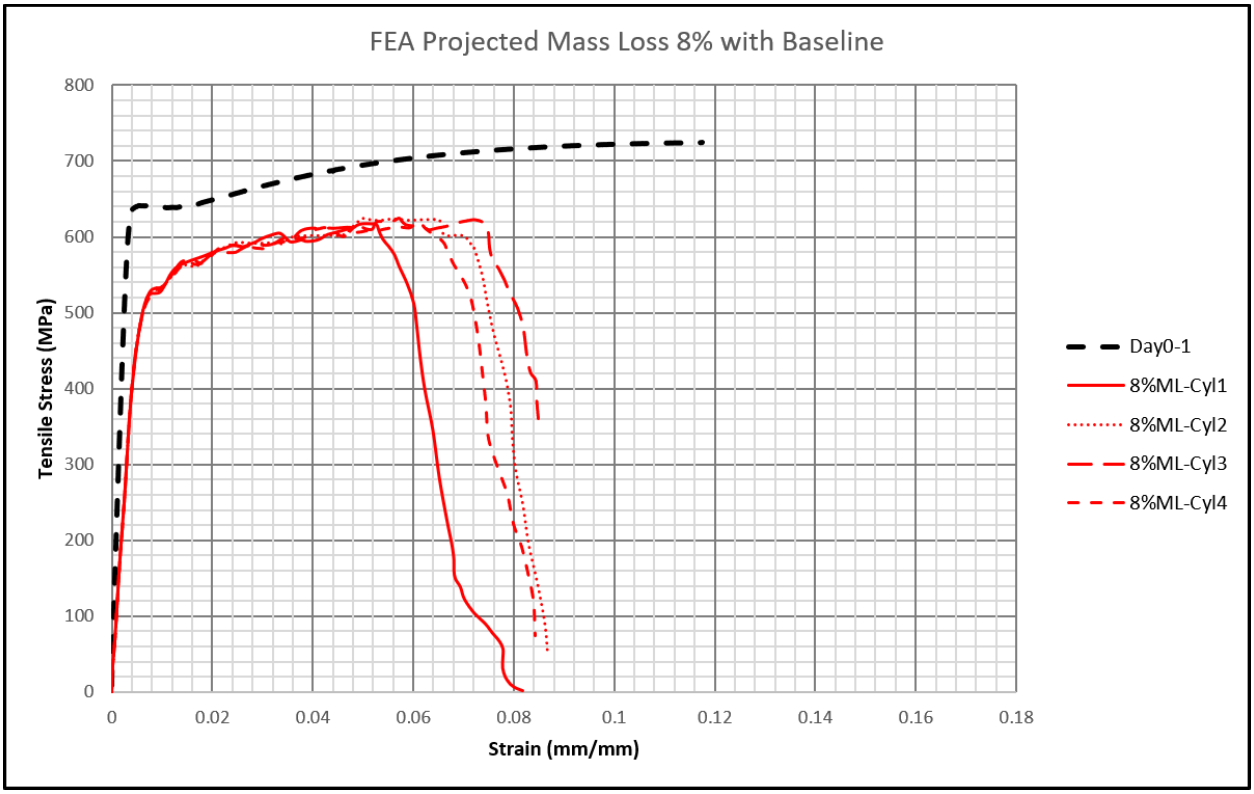

Figure 5.22. – *Comparison of 4 different stochastic pit realisations for FE against baseline Day 0 for tensile stress vs strain at mass loss 8% projection.*

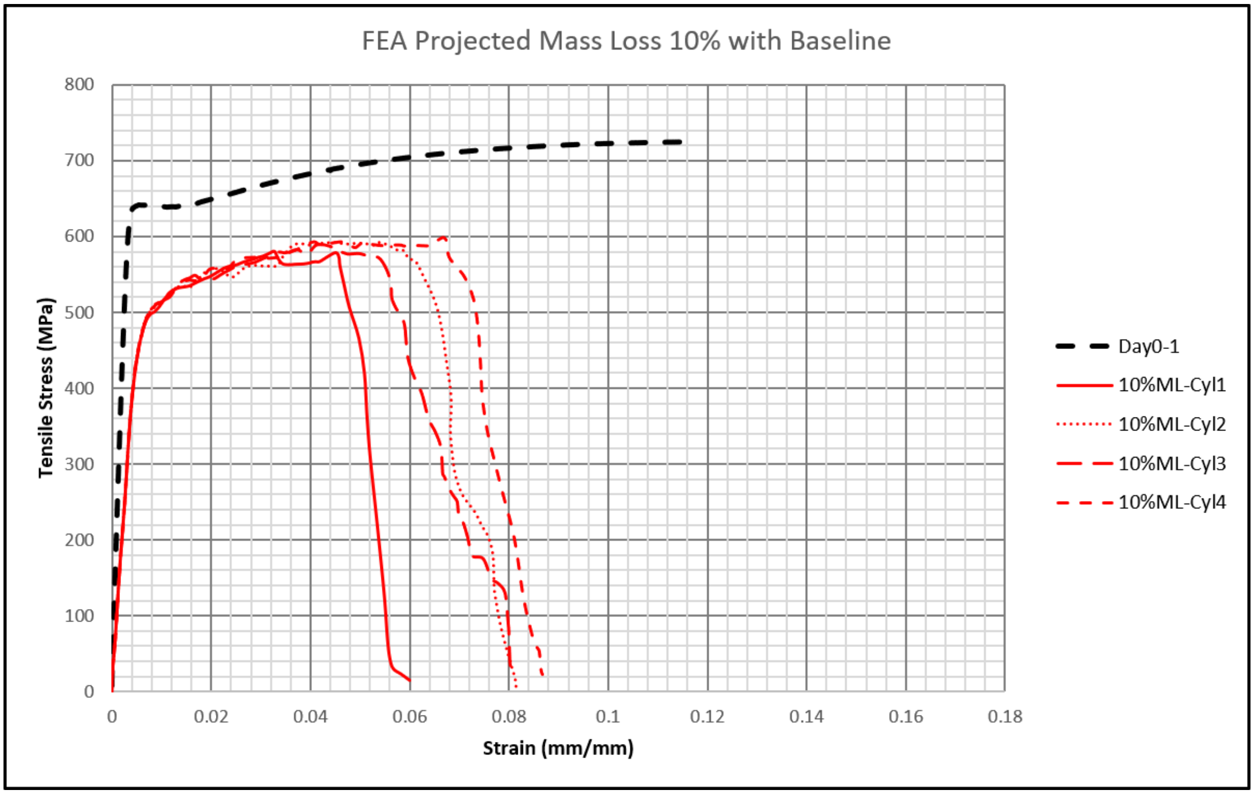

Figure 5.23. – *Comparison of 4 different stochastic pit realisations for FE against baseline Day 0 for tensile stress vs strain at mass loss 10% projection.*

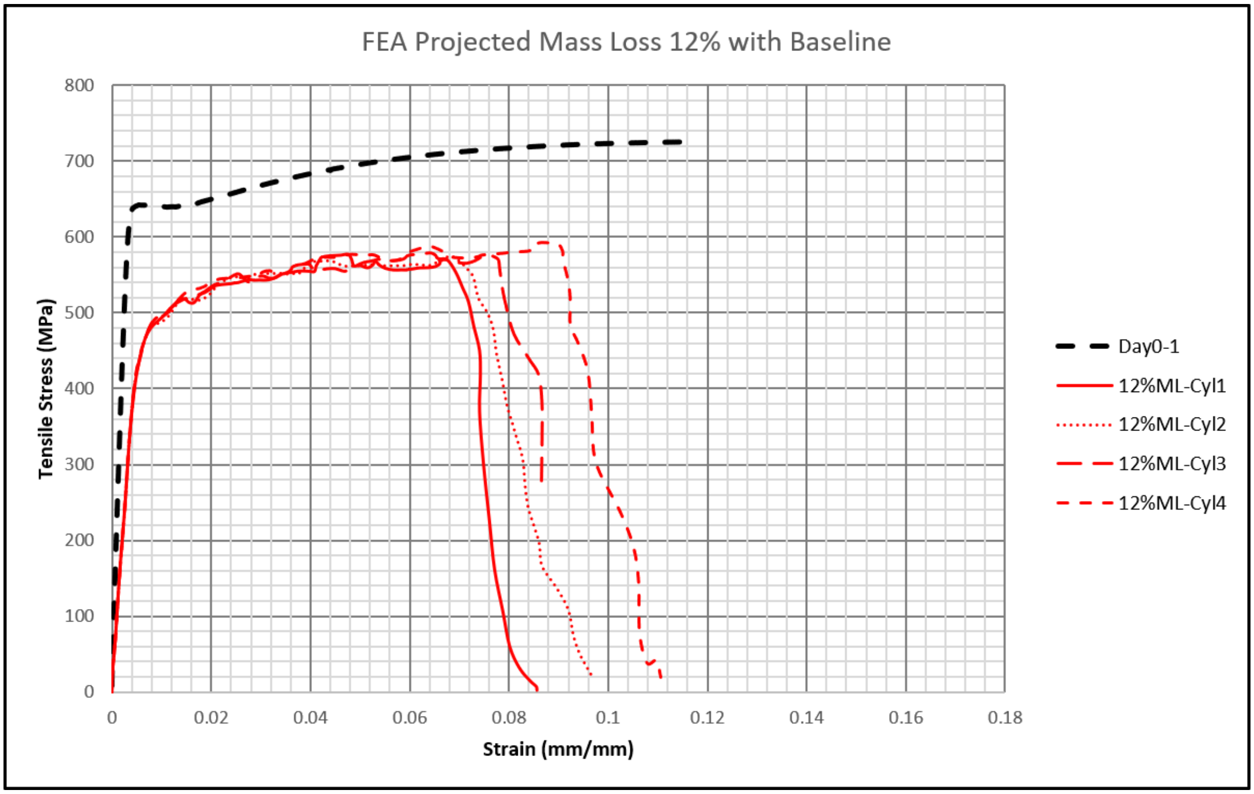

Figure 5.24. – *Comparison of 4 different stochastic pit realisations for FE against baseline Day 0 for tensile stress vs strain at mass loss 12% projection.*

The projected results show a clear and approximately monotonic reduction in ultimate tensile strength once the corrosion severity is increased beyond the experimental range. The group-mean UTS falls from about 700 MPa at 4% mass loss to about 580 MPa at 12% mass loss. Relative to the Day-0 finite-element baseline of 721.1 MPa, this corresponds to a reduction of about 3% at 4%, rising to about 19% at 12%. This is in marked contrast to the near-flat response over the experimentally matched range, where the reduction was only about 1.8% up to 2.49%, and it is now much larger than the within-group morphology scatter of about 4 to 7 MPa. The strength reduction is therefore clearly resolved at higher severity, whereas at low severity it was masked by scatter. The full set of projected properties, expressed both as absolute values and as residual factors normalised to the Day-0 baseline, is given in Table 5.16.

Mass loss Δm (%)	FE UTS (MPa)	FE fracture strain ε_f	FE toughness, U (MJ/m³)
4	700.1 ± 7.1	0.138 ± 0.020	80.9 ± 7.8
6	652.8 ± 4.0	0.105 ± 0.002	61.7 ± 1.1
8	620.9 ± 3.6	0.084 ± 0.002	43.6 ± 4.1
10	590.1 ± 6.4	0.096 ± 0.040	36.7 ± 6.0
12	580.4 ± 6.8	0.095 ± 0.010	46.0 ± 5.3

Table 5.16. *Projected finite-element tensile properties across the 4 to 12% gauge-section mass-loss range. Each value is the mean of four stochastic cylindrical-pit realisations; the UTS is reported as mean ± standard deviation. Residual factors Rσ, Rε and RU are normalised to the uncorroded Day-0 finite-element baseline (UTS 721.1 MPa, fracture strain 0.160, toughness 107.5 MJ/m³). The material card is held constant, so the changes are due to the projected pitted geometry alone.*

Fracture strain and toughness also reduce sharply with increasing severity. The mean fracture strain falls from about 0.138 at 4% to about 0.085 to 0.095 at 8 to 12%, and the mean toughness falls from about 81 MJ/m³ at 4% to about 37 to 46 MJ/m³ over the same interval. The reductions are not perfectly monotonic at 10 and 12%: one realisation at 10% retained an unusually high fracture strain, which lifts the group mean, and the 12% group recovers slightly. This residual scatter is consistent with the morphology effect identified in Section 5.9.2, in which the critical-section geometry, rather than the mass loss alone, governs the post-peak response. In proportional terms the deformation-related quantities therefore remain more sensitive to pitting than the strength, but at higher severity the absolute strength reduction is no longer negligible.

The projected study also defines the upper limit of the low-severity linear relationships proposed in Chapter 6. Extending the anchored strength relationship, $R_\sigma = 1 - 0.0043\Delta m$, to 12% would predict only about a 5% strength loss, whereas the projection gives about 19%; conversely, extending the fracture-strain relationship, $R_\varepsilon = 1 - 0.0485\Delta m$, to 12% would predict a residual factor of about 0.42, whereas the projection gives about 0.59. The low-severity coefficients therefore under-predict the strength loss and over-predict the ductility loss when applied at high severity, which confirms that the relationships must not be linearly extrapolated and that the response becomes genuinely nonlinear above the fitted range.

The pit counts of the four realisations at each level, and another analysis by grouping by pit count, are summarised in Table 5.17, following the same ranking convention used in Table 5.15 for the experimental exposures.

Case Groups for Trend Across (ranked by number of pits, with Group 1 being the highest number of pits in the projected FEA models)	**4% mass loss**	**6% mass loss**	**8% mass loss**	**10% mass loss**	**12% mass loss**
Case Group 1	Cyl-4 with 145 pits	Cyl-4 with 146 pits	Cyl-3 with 139 pits	Cyl-4 with 143 pits	Cyl-4 with 144 pits
Case Group 2	Cyl-3 with 135 pits	Cyl-3 with 124 pits	Cyl-4 with 134 pits	Cyl-3 with 127 pits	Cyl-3 with 135 pits
Case Group 3	Cyl-2 with 121 pits	Cyl-2 with 118 pits	Cyl-2 with 123 pits	Cyl-2 with 120 pits	Cyl-2 with 125 pits
Case Group 4	Cyl-1 with 111 pits	Cyl-1 with 108 pits	Cyl-1 with 113 pits	Cyl-1 with 115 pits	Cyl-1 with 115 pits

Table 5.17. *Case grouping for the projected higher-severity study, by ranking the number of pits in each stochastic cylindrical-pit model across the 4 to 12% gauge-section mass-loss levels.*

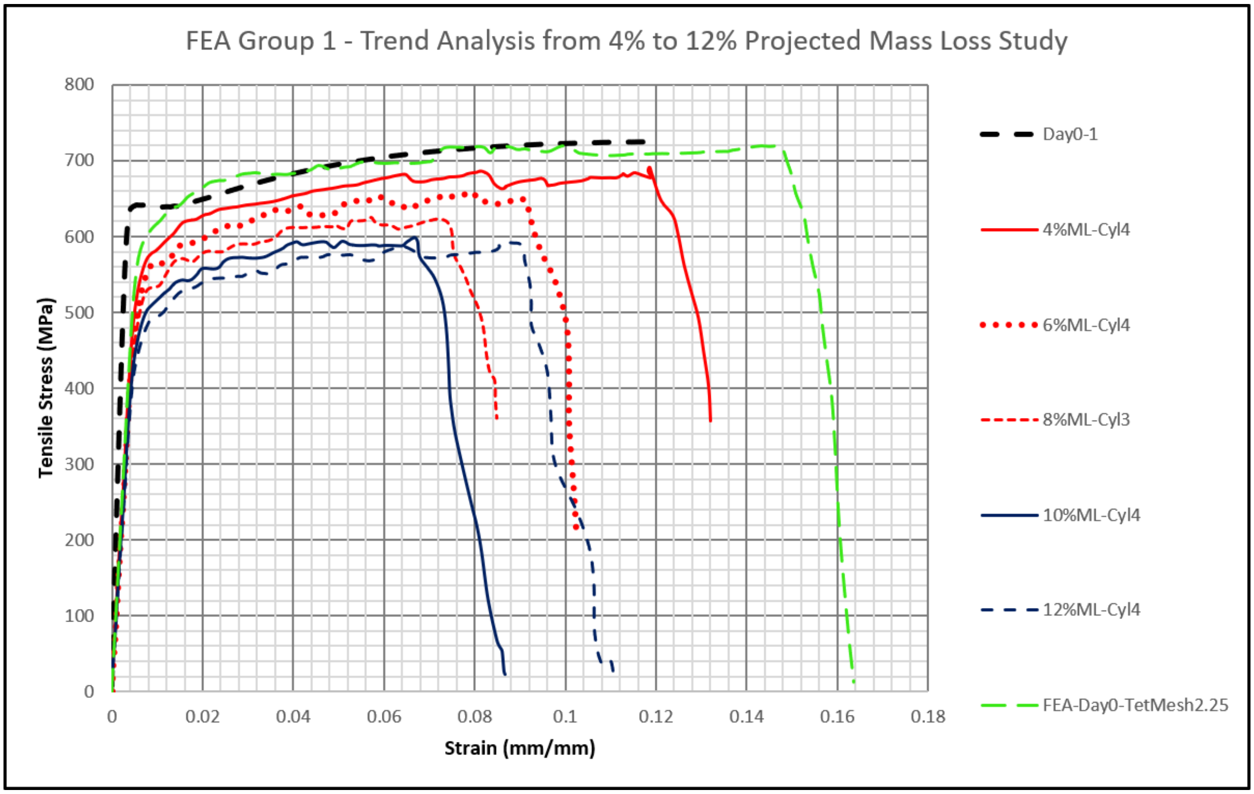

Figure 5.25. - *Trend Analysis for Grouping 1 of 4% to 12% Mass Loss Projection Study comparison of Experimental Data vs FEA Pitted Models*

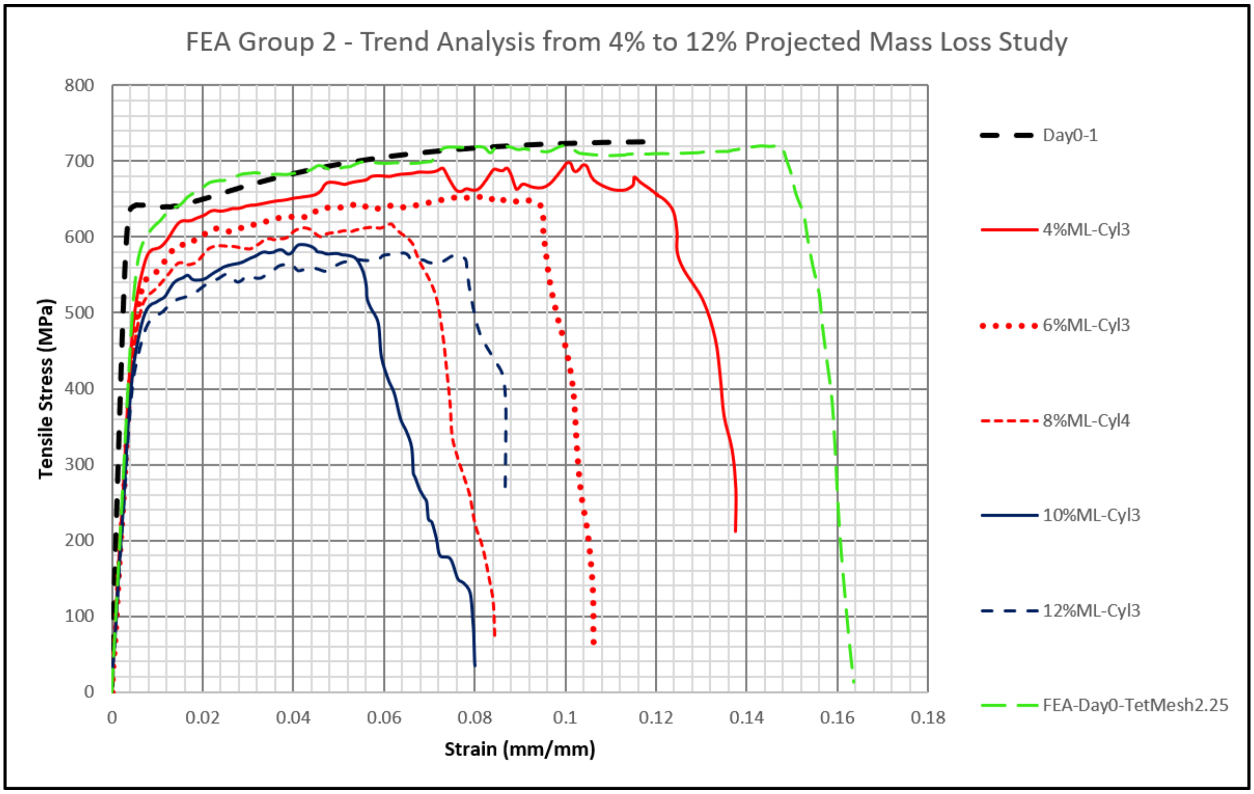

Figure 5.26. - *Trend Analysis for Grouping 2 of 4% to 12% Mass Loss Projection Study comparison of Experimental Data vs FEA Pitted Models*

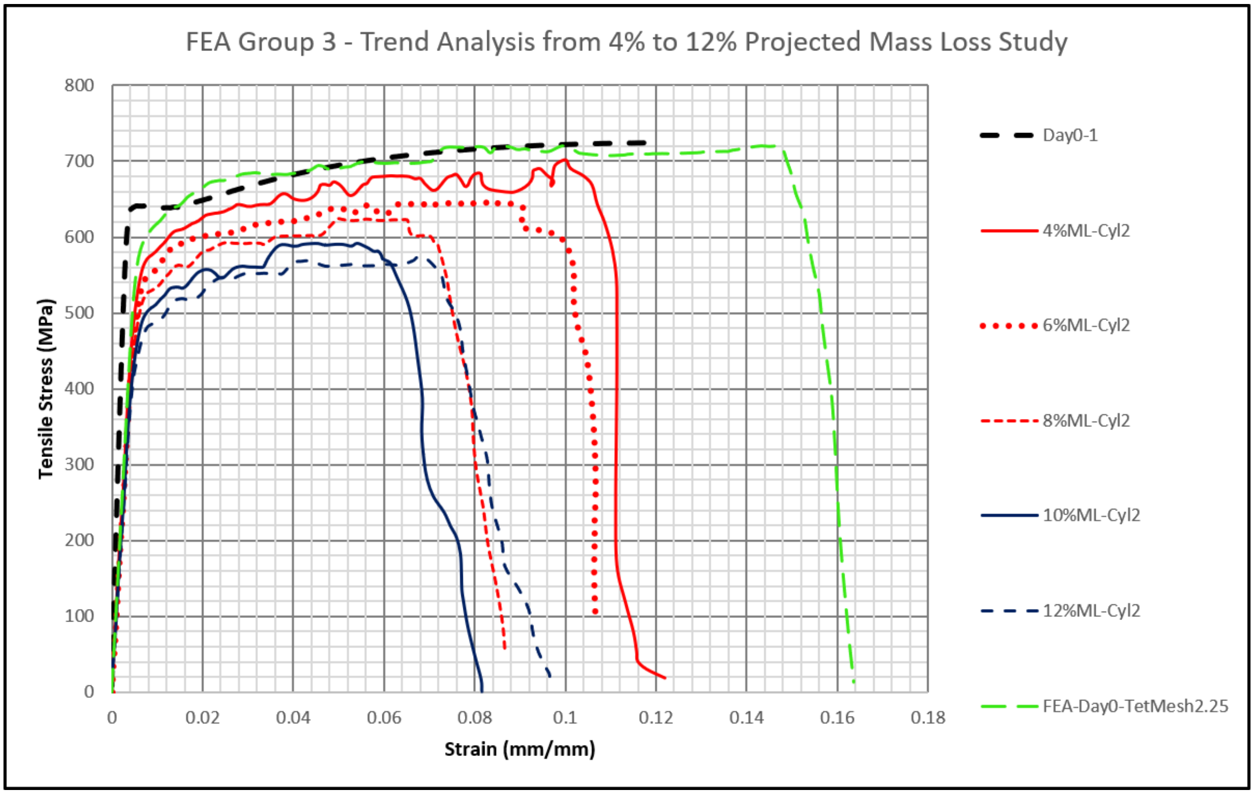

Figure 5.27. - *Trend Analysis for Grouping 3 of 4% to 12% Mass Loss Projection Study comparison of Experimental Data vs FEA Pitted Models*

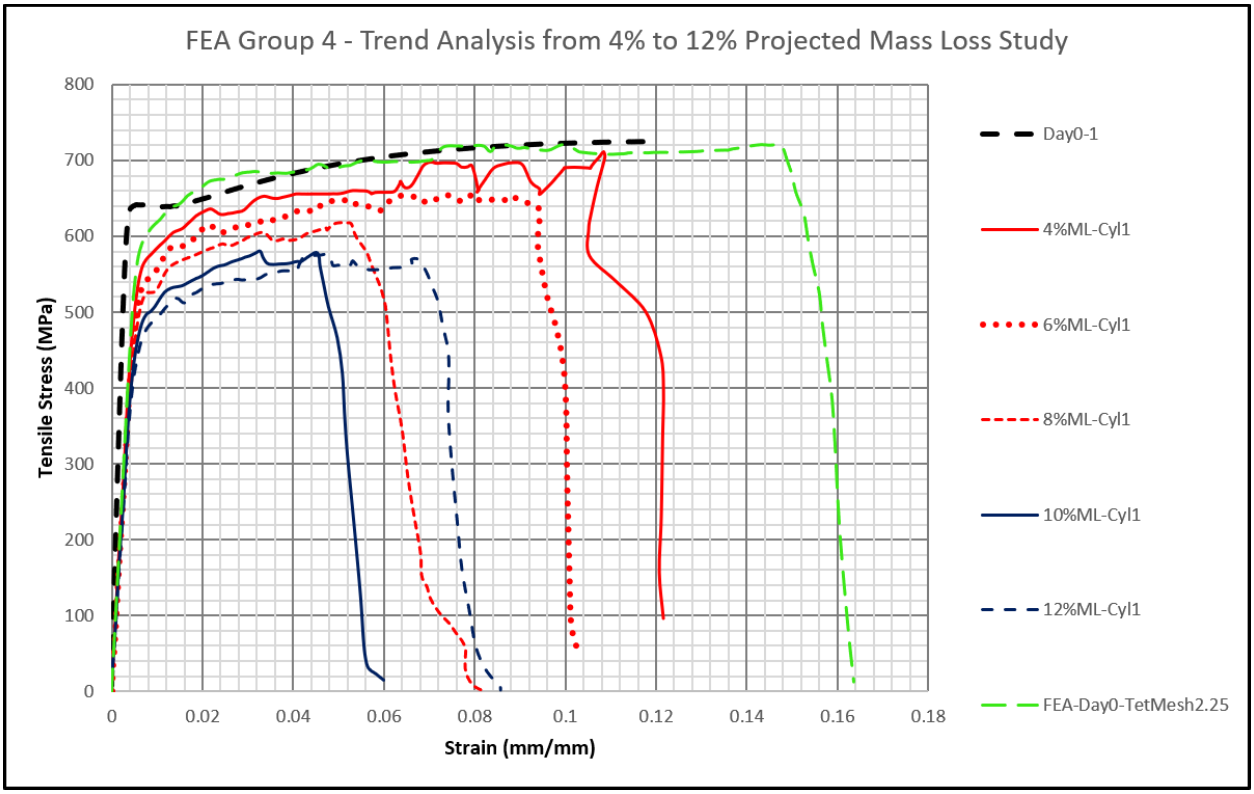

Figure 5.28. - *Trend Analysis for Grouping 4 of 4% to 12% Mass Loss Projection Study comparison of Experimental Data vs FEA Pitted Models*

The projected 4–12% mass-loss study extends the same interpretation observed in the lower-severity Day 14 to Day 42 FE results, but at a level where the degradation becomes more pronounced. In the Day 14 to Day 42 simulations, corresponding to approximately 1.29–2.49% gauge-section mass loss, the pitted models remained close to the Day 0 baseline in terms of UTS, and the main visible effect was a modest reduction in fracture strain and toughness. In contrast, the projected 4–12% models show a clearer downward shift in the stress–strain response, indicating that the loss of load-carrying capacity becomes more evident once the imposed material loss exceeds the experimentally measured range.

The comparison also suggests a transition in the role of mass loss. At the lower experimental corrosion levels, the FE response is dominated by scatter and local pit arrangement, while the average UTS remains relatively stable. In the projected range, mass loss has a more pronounced effect on strength degradation to produce noticeable trend loss of tensile strength, as shown by the progressive reduction in peak stress from 4% to 12%. However, even in the projected cases, the fracture strain and post-peak response remain strongly affected by the individual pit realisation. This indicates that increasing mass loss strengthens the average degradation trend but does not remove the influence of stochastic morphology.

The experimental results provide useful context for this interpretation, although they should not be treated as direct validation of the projected severity range. The experimental exposure programme reached only relatively low mass-loss levels compared with the 4–12% projected models. Therefore, the projected simulations should be interpreted as an extrapolated numerical investigation based on the same modelling framework, rather than as a direct reproduction of measured experimental specimens. The lower-severity FE results support the baseline modelling approach, while the higher-severity projections are used to explore how the same pitting idealisation may behave under more severe material loss.

The grouped pit-count comparison further shows why the projected study cannot be interpreted using mass loss or pit count alone. At the experimental mass-loss levels, the response differences between realisations are small enough that pit morphology mainly appears as scatter around a near-baseline tensile response. At the projected mass-loss levels, the same morphology effect becomes more visible because deeper and more severe pits create stronger local stress concentrations. This explains why the 10% and 12% cases can show substantial differences in fracture strain and toughness even when the same target mass loss is imposed.

Overall, the projected grouped analysis complements the Day 14 to Day 42 FE results by showing how the relative importance of corrosion descriptors changes with severity. In the experimentally measured range, mass loss has limited influence on UTS, and the main effect of pitting is reduced ductility. In the projected range, mass loss produces a clearer strength reduction, while pit morphology continues to control localisation and post-peak scatter. Local pit morphology remains necessary for interpreting deformation capacity and fracture behaviour.

5.10.2 Mesh Convergence Check for Mass Loss Projection

As the higher-severity models involved deeper pit geometries, the influence of mesh density was re-examined for the most severe projected corrosion case. The 12% Cyl-4 model was therefore re-analysed using a coarser approximate global seed size of 3.0 mm, compared with the production mesh seed of 2.25 mm. An additional finer-mesh attempt using a 1.5 mm global seed was also carried out; however, this simulation did not complete successfully. The combination of deep pit geometry and high local plastic deformation led to excessive element distortion, causing the Abaqus/Explicit analysis to terminate automatically due to a distortion error.

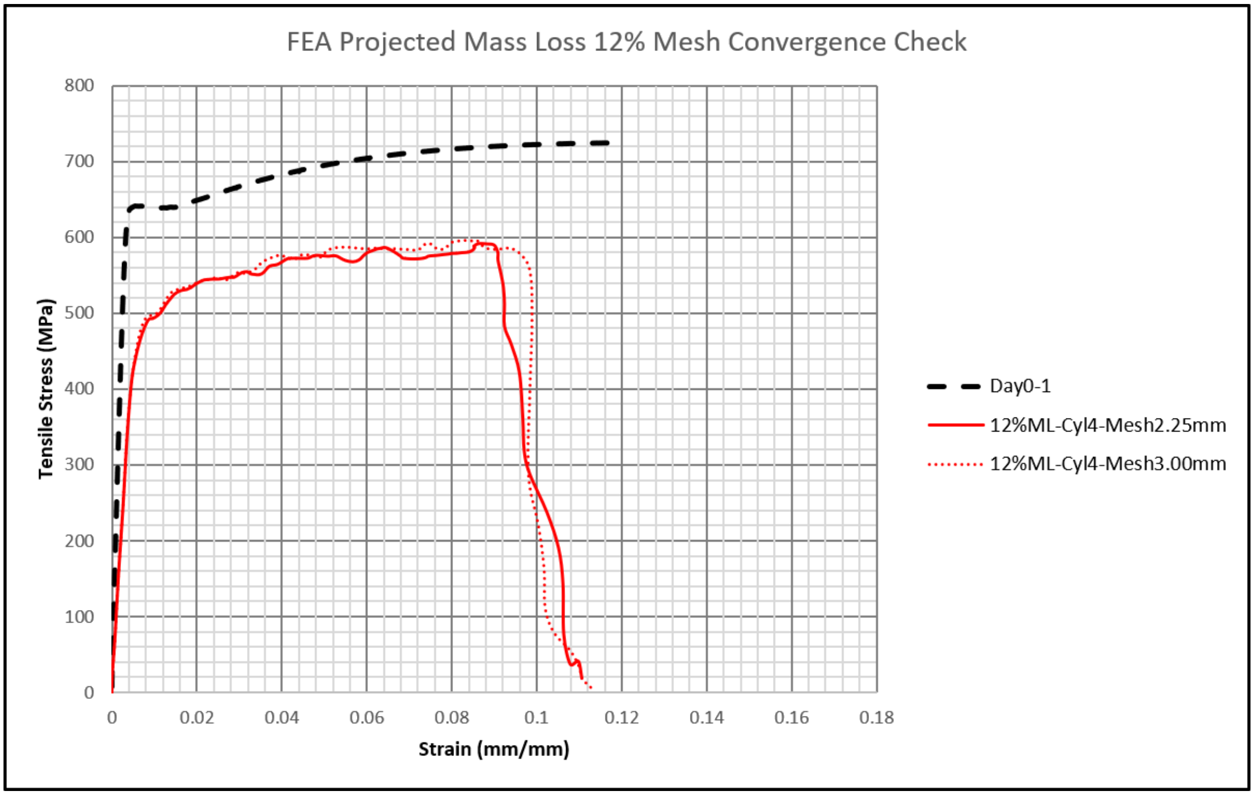

Figure 5.29. – *Mesh sensitivity study conducted at highest mass loss projection of 12% with C3D10 Tetrahedral meshing done at 2.25mm and 3.00mm. Run was unsuccessful for usage of approximate global mesh size of 1.50mm due to extreme distortion of elements.*

The comparison between the 2.25 mm production mesh and the 3.0 mm mesh is summarised in Table 5.18.

Quantity	**2.25 mm seed (production)**	**3.0 mm seed**	**Difference**
Ultimate tensile strength (MPa)	591.9	595.8	+0.7%
Fracture strain ε_f	0.111	0.114	+2.8%
Toughness (MJ/m³)	54.4	55.4	+1.7%

Table 5.18. *Mesh-sensitivity check at the most severe projected condition (12% mass loss, Cyl-4), comparing the 2.25 mm production seed with a 3.0 mm seed. A finer 1.5 mm seed was also attempted but the analysis was aborted automatically because of excessive element distortion. The predicted UTS differs by less than 1% and the fracture strain and toughness by less than 3%, indicating that the projected results are governed by the modelled geometry rather than by mesh resolution even at the highest severity.*

Taken together, the projected study shows that the geometry-isolated workflow can be carried to substantially higher corrosion severity, and that the strength reduction which was hidden by scatter in the experimental range becomes clearly resolved by 12% gauge-section mass loss.

Two limits of the projection should nevertheless be kept in view. First, the study is a numerical projection that holds the material card fixed; it does not represent any change in the bulk material behaviour that may accompany real corrosion at higher severity (Section 7.4.3). Second, the projection still represents corrosion as a population of discrete, non-interacting cylindrical pits. Beyond the 12% mass loss range examined here, pit coalescence and nonlinear net-section loss are expected to become dominant, and the probability that several severe pits align across a critical section increases, so the response may become controlled by a small number of severe defects rather than by the average pit population.

6. Proposed Preliminary Trend Relationships

In this thesis, the corrosion severity used for the predictive relationships is the mass-loss percentage referenced to the exposed gauge-section mass. This basis is used because the reduced gauge section was the region intentionally exposed to the sodium-chloride solution, while the shoulders and gripping regions were wrapped and protected during immersion. Therefore, the gauge-section mass provides the most appropriate reference mass for linking measured corrosion loss to the pitted finite element geometry.

Following the project aim, this chapter proposes simple predictive relationships linking residual tensile properties to mass loss. The relationships are derived from the geometry-isolated finite element results of Sections 5.8 to 5.10, where the material model is held constant and only the pitted geometry changes. The relationships are presented as provisional engineering estimates. Their range of validity, fit quality and limitations are stated explicitly. They are best described as preliminary fitted relationships rather than design equations.

6.1 Form of the relationships

The residual properties are expressed as dimensionless residual factors normalised to the uncorroded Day 0 finite element baseline:

$$R_\sigma = f_u / f_{u,0} \quad (6.1)$$

$$R_\varepsilon = \varepsilon_f / \varepsilon_{f,0} \quad (6.2)$$

$$R_U = U / U_0 \quad (6.3)$$

where R_σ is the residual UTS factor, R_ε is the residual fracture-strain factor and R_U is the residual toughness factor. The mass loss is denoted by Δm and is expressed as a percentage of the exposed gauge-section mass.

Because an uncorroded specimen must have a residual factor of unity, the primary relationships are constrained to pass through the point $\Delta m = 0$, $R = 1$. This physically anchored form is used as the main statement of each relationship. Unconstrained linear fits are also reported for comparison, because their slopes and intercepts indicate how closely the finite element data follow the anchored form.

6.2 Derivation and fitted relationships

Linear relationships were fitted to the five group-mean residual factors from Day 14 to Day 42. The mass-loss range is from 1.29% to 2.49% when referenced to the exposed gauge-section mass.

The proposed relationships are written as:

$$R_\sigma = 1 - k_\sigma \Delta\mathrm{m} \quad (6.1a)$$

$$R_\varepsilon = 1 - k_\varepsilon \Delta\mathrm{m} \quad (6.2a)$$

$$R_U = 1 - k_U \Delta\mathrm{m} \quad (6.3a)$$

where;

k_σ = fitted strength-reduction coefficient

k_ε = fitted fracture-strain / deformation-capacity reduction coefficient

k_U =fitted toughness-reduction coefficient

The physically anchored relationships are:

$$R_\sigma = 1 - 0.0043\Delta\mathrm{m} \quad (6.4)$$

$$R_\varepsilon = 1 - 0.0485\Delta\mathrm{m} \quad (6.5)$$

$$R_U = 1 - 0.0597\Delta\mathrm{m} \quad (6.6)$$

where Δm is in percent of the exposed gauge-section mass.

The corresponding unconstrained fits are

$$R_\sigma = 1.023 - 0.0156\Delta\mathrm{m} \quad (6.4a)$$

$$R_\varepsilon = 1.002 - 0.0493\Delta\mathrm{m}; \quad (6.5a)$$

$$R_U = 1.013 - 0.0659\Delta\mathrm{m}; \quad (6.6a)$$

The unconstrained intercepts are close to unity, especially for fracture strain and toughness, which supports the use of the anchored form. The anchored fit quality is weakest for strength because the FE UTS response is small and non-monotonic over the low mass-loss range. This is consistent with the interpretation in Sections 5.8 and 5.9 that UTS is comparatively insensitive to low-level pitting and is affected by morphology-induced scatter. The deformation-related quantities give clearer relationships, especially toughness.

Property	**Anchored relationship**	**Unconstrained fit**	**R^2 (anchored)**	**Predicted residual at $\Delta m = 2.49\%$**
Strength R_σ	$1 - 0.0043\Delta m$	$1.023 - 0.0156\Delta m$	≈ 0.34	≈ 0.989, about 1.1% reduction
Fracture strain R_ε	$1 - 0.0485\Delta m$	$1.002 - 0.0493\Delta m$	≈ 0.80	≈ 0.879, about 12.1% reduction
Toughness R_U	$1 - 0.0597\Delta m$	$1.013 - 0.0659\Delta m$	≈ 0.88	≈ 0.851, about 14.9% reduction

Table 6.1. *Proposed anchored predictive relationships for residual UTS, fracture strain and toughness as functions of gauge-section mass-loss percentage Δm. The relationships are fitted and recommended over the experimentally matched range up to 2.49%; the projection study in Section 5.10 shows that the response is clearly nonlinear over the 4 to 12% range, so this single linear fit is not extended across the full projected range.*

The higher-severity projection study provides an important check on the range of applicability of the low-severity relationships. The projected simulations cover gauge-section mass losses of 4%, 6%, 8%, 10%, and 12%, which extend beyond the experimental corrosion range. These models were not used to re-fit the low-severity relationships. Instead, they were used to assess whether the same linear trends remain reasonable when corrosion severity is increased.

The projected results show that a single linear extension of Equations 6.4 to 6.6 is not appropriate over the full 0–12% range. At low mass loss, the UTS reduction is small and partly masked by stochastic morphology effects. At higher mass loss, the stress–strain curves show a clearer downward shift, and the peak stress reduces more substantially. This indicates that mass loss becomes a stronger global driver of strength degradation once the imposed material loss exceeds the experimentally measured range.

The mean projected FE results are summarised in Table 6.2. The residual factors were calculated using the Day 0 FE baseline values of $f_{u,0} = 721.1$MPa, $\varepsilon_{f,0} = 0.160$, and $U_0 = 107.5$MJ/m³.

Projected mass loss, Δm (%)	**FE UTS (MPa)**	**R_σ**	**FE fracture strain, ε_f**	**R_ε**	**FE toughness, U(MJ/m³)**	**R_U**
4	700.1 ± 7.1	0.971	0.138 ± 0.020	0.863	80.9 ± 7.8	0.752
6	652.8 ± 4.0	0.905	0.105 ± 0.002	0.656	61.7 ± 1.1	0.574
8	620.9 ± 3.6	0.861	0.084 ± 0.002	0.525	43.6 ± 4.1	0.406
10	590.1 ± 6.4	0.818	0.096 ± 0.040	0.600	36.7 ± 6.0	0.341
12	580.4 ± 6.8	0.805	0.095 ± 0.010	0.594	46.0 ± 5.3	0.428

Table 6.2. *Projected FE residual tensile properties from 4% to 12% gauge-section mass loss. Values are reported as mean ± standard deviation from four stochastic realisations at each projected mass-loss level.*

The projected results show two important trends. First, the UTS reduction becomes much more pronounced at higher corrosion severity. At 12% projected mass loss, the residual UTS factor is approximately 0.805, corresponding to a strength reduction of about 19.5% relative to the Day 0 FE baseline. This is much larger than would be predicted by extending the low-severity strength relationship, which would give $R_\sigma \approx 0.948$ at $\Delta m = 12\%$. Therefore, the low-severity strength coefficient under-predicts the strength loss at high projected mass loss.

Second, the fracture strain and toughness do not follow a perfectly monotonic sequence in the projected range. The reduction is severe from 4% to 8%, but the 10% and 12% mean values are affected by morphology-induced scatter and the sensitivity of post-peak response to the critical pit arrangement. This confirms that fracture strain and toughness are not governed by mass loss alone. At higher severity, the local distribution of pits, including pit depth, spacing, clustering, and position relative to the eventual failure section, has a stronger influence on localisation and final deformation capacity.

The projection study therefore changes the interpretation of the fitted relationships. Equations 6.4 to 6.6 are suitable as low-severity trend relationships within the experimentally matched range. They should not be treated as general equations that can be linearly extrapolated to heavily corroded conditions. For mass losses in the projected 4–12% range, the tabulated FE trends and grouped stress–strain comparisons provide a more appropriate basis for interpretation than the low-severity linear equations.

Since the mean fracture strain and toughness values at 10% and 12% projected mass loss were affected by morphology-induced scatter, an additional conservative monotonic trend was calculated for comparison. This trend was obtained by fitting a linear relationship to the 4%, 6%, and 8% projected results, where both fracture strain and toughness showed a clear decreasing sequence. The fitted relationships were then extrapolated to 10% and 12% mass loss to provide a conservative reference envelope. This conservative trend is not used to replace the actual FE results but is included to show the lower-bound implication that would be obtained if the initial 4–8% degradation trend continued monotonically.

Projected mass loss, Δm (%)	**FE UTS (MPa)**	**R_σ**	**FE fracture strain, ε_f**	**R_ε**	**FE toughness, U(MJ/m³)**	**R_U**
4	700.1 ± 7.1	0.971	0.138 ± 0.020	0.863	80.9 ± 7.8	0.752
6	652.8 ± 4.0	0.905	0.105 ± 0.002	0.656	61.7 ± 1.1	0.574
8	620.9 ± 3.6	0.861	0.084 ± 0.002	0.525	43.6 ± 4.1	0.406
10	590.1 ± 6.4	0.818	0.096 ± 0.040	0.6	36.7 ± 6.0	0.341

12	580.4 ± 6.8	0.805	0.095 ± 0.010	0.594	46.0 ± 5.3	0.428

Table 6.3. *Comparison between the direct projected FE results and a conservative monotonic reference trend for fracture strain and toughness. The conservative values were obtained by fitting a linear decreasing trend to the 4%, 6%, and 8% projected mass-loss results and extrapolating this trend to 10% and 12%. The conservative trend is included only as a lower-bound reference and does not replace the direct FE results, which retain the effects of stochastic pit morphology and post-peak localisation.*

As such, proposed conversative residual relationships based on the projection study are derived.

For the **conservative monotonic reference trend based on the 4–8% projected results**, the three residual-factor equations are:

$$R_{\sigma,\text{cons}} = 1.0772 - 0.02746\Delta m \tag{6.7}$$

$$R_{\varepsilon,\text{cons}} = 1.1802 - 0.08281\Delta m \tag{6.8}$$

$$R_{U,\text{cons}} = 1.0978 - 0.08674\Delta m \tag{6.9}$$

where $\Delta m$is the projected mass loss in percent.

These are based on Equations 6.1 to 6.3 respectively:

$$R_\sigma = \frac{f_u}{f_{u,0}}$$

$$R_\varepsilon = \frac{\varepsilon_f}{\varepsilon_{f,0}}$$

$$R_U = \frac{U}{U_0}$$

using the Day 0 FE baseline:

$$f_{u,0} = 721.1 \text{ MPa}$$

$$\varepsilon_{f,0} = 0.160$$

$$U_0 = 107.5 \text{ MJ/m}^3$$

The corresponding absolute-value linear fits are:

$$f_{u,\text{cons}} = 776.73 - 19.80\Delta m \tag{6.10}$$

$$\varepsilon_{f,\text{cons}} = 0.1888 - 0.01325\Delta m \tag{6.11}$$

$$U_{\text{cons}} = 118.02 - 9.325\Delta m \tag{6.12}$$

6.3 Sensitivity and interpretation

The most important feature of the relationships is the relative size of the fitted coefficients. The fracture-strain coefficient is approximately 11 times the strength coefficient, and the toughness coefficient is approximately 14 times the strength coefficient:

$k_\varepsilon / k_\sigma \approx 11$ (6.13)

$k_U / k_\sigma \approx 14$ (6.14)

This means that within the studied range, fracture strain and toughness reduce approximately an order of magnitude faster than UTS per unit of gauge-section mass loss. This result captures the main mechanical finding of the thesis. Pitting corrosion at low mass loss has only a small effect on peak tensile strength, but it has a clearer effect on deformation capacity.

At the maximum studied gauge-section mass loss of 2.49%, the anchored relationships predict a strength reduction of approximately 1.1%, a fracture-strain reduction of approximately 12.1% and a toughness reduction of approximately 14.9%. Therefore, an assessment based only on UTS would detect very little degradation, while a ductility or toughness assessment would show a more significant reduction.

The strength relationship should be interpreted cautiously. The FE UTS values do not form a smooth linear degradation trend because the strength effect is small and affected by the random pit arrangement. The strength equation is therefore best viewed as an indicative mean trend. The fracture-strain and toughness relationships are more meaningful within this dataset because they show clearer reductions with increasing pitting severity.

The relationships can be used in either direction within the fitted range. Given a measured gauge-section mass loss, Equations 6.4 to 6.6 provide first estimates of the residual strength, fracture strain and toughness factors. These factors can be multiplied by the uncorroded properties to obtain absolute estimates. Conversely, a target residual property can be inverted to estimate the corresponding mass-loss level. This provides the mass-loss-to-behaviour link sought in the project aim, but only within the stated range of validity.

The projected study extends this interpretation by showing that the role of mass loss changes with corrosion severity. At low mass loss, UTS remains within a narrow scatter band and is strongly influenced by stochastic pit morphology. At projected mass losses of 4–12%, the reduction in UTS becomes clearer, indicating that the global loss of material begins to dominate the strength response. However, even in the projected range, fracture strain and toughness remain strongly affected by the individual pit realisation. This shows that increasing mass loss strengthens the average degradation trend but does not remove the influence of local pit morphology.

The projection study also confirms that pit count alone is not a sufficient descriptor of tensile degradation. At the same target mass loss, a larger number of pits can distribute material loss across more defects, while a smaller number of pits can concentrate the same removed volume into fewer and potentially more severe stress raisers. Therefore, the residual tensile response is controlled by both the total removed volume and the critical local pit geometry.

6.4 Status and limitations of the relationships

They are derived from finite element results where the material card is held constant and only the pitted geometry changes. They therefore describe the predicted geometric effect of pitting on the studied steel. They are not independent experimental degradation equations.

The present experimental data cannot fully verify these relationships because the corrosion severity is low and the experimental results are affected by coupon-to-coupon scatter. The relationships are therefore supported by the calibrated Day 0 baseline, the verified Abaqus workflow and the agreement in trend with the corroded-steel literature. The predicted pattern, small strength loss with larger ductility and toughness loss, is consistent with previous studies showing that ductility-related properties are more sensitive to corrosion than UTS [3], [6].

The relationships are fitted over the experimentally matched gauge-section mass-loss range, up to 2.49%, and should not be linearly extrapolated to heavily corroded members. The higher-severity projection study in Section 5.10 confirms that the response becomes markedly nonlinear above this range, with the ultimate tensile strength falling by about 19% by 12% gauge-section mass loss, so that the low-severity coefficients under-predict the strength loss and over-predict the ductility loss when applied at high severity. Secondly, the relationships are specific to the steel grade, coupon geometry, single-face pitting assumption and cylindrical pit idealisation used in this thesis. The relationships are valid only for monotonic uniaxial tensile loading of flat dog-bone coupons with geometry and boundary conditions like those used in this study. They should not be directly extrapolated to different steel grades, thicker structural members, different coupon geometries, different pit shapes, multi-surface corrosion patterns, alternative material models, cyclic loading, bending, compression or structural-scale members without further calibration. In particular, the projected mass-loss cases beyond the experimental corrosion range should be interpreted as numerical sensitivity results rather than experimentally validated predictive equations. Third, the coefficients are provisional. The fracture-strain and toughness relationships depend on the element-deletion damage model, and absolute fracture strain remains mesh-dependent.

Parameter	**Validity range / assumption in this study**	**Limitation**
Steel material	Low-carbon structural steel represented using the calibrated Day-0 material model	Not directly transferable to other steel grades without recalibration
Geometry	Flat ISO-type dog-bone coupon / gauge-section tensile model	Not directly applicable to structural members, welded details or different section geometries
Corrosion descriptor	Effective gauge-section mass loss	Mass loss does not fully describe pit depth, radius, density or spacing
Pit shape	Flat-bottomed cylindrical pits	Natural pits may be rounded, irregular, undercut or clustered
Pit distribution	Stochastic, seed-controlled pit fields with selected radius/depth/spacing rules	Other pit-generation rules may produce different localisation behaviour

Surface condition	Mainly one-surface pitting idealisation in FE	Experimental corrosion occurred on all exposed gauge-section surfaces
Mass-loss range	Experimental low mass-loss range plus numerical projection up to 12% gauge-section mass loss	Projection is not experimentally validated beyond the tested range
Loading type	Monotonic uniaxial tensile loading	Not valid for fatigue, cyclic loading, bending, compression or combined loading
Material degradation	Fixed Day-0 material model for all corrosion levels	Does not include corrosion-induced material property degradation
FE assumptions	Abaqus/Explicit, selected mesh, mass scaling and endpoint definition	Results depend on quasi-static checks, mesh sensitivity and fracture-point definition
Stochastic sample size	Four realisations per corrosion level	Indicates trends and scatter only; not a full probabilistic model

Table 6.4. – *Summary table depicting the validity and assumptions as well as limitations in relation to each parameter considered in the FEA modelling.*

Table 6.4 provides the summary of the conditions under which the proposed relationships should be interpreted. The fitted equations are therefore not intended to provide universal design predictions for all forms of pitted steel corrosion. Instead, they represent first-order FE-based trend relationships for the specific coupon geometry, material model, pit-generation assumptions and loading condition adopted in this study. Their main purpose is to summarise the average numerical response obtained from the mass-loss-matched stochastic pit models and to show the relative sensitivity of strength, fracture strain and toughness to increasing corrosion severity.

The proposed relationships should therefore be regarded as trend relationships derived from controlled idealised FE simulations, rather than general predictive equations for all forms of naturally corroded steel.

With these qualifications, the relationships are offered as a transparent first step toward mass-loss-based prediction of residual tensile behaviour. They are not design equations. They are engineering estimates derived from a controlled numerical workflow and should be re-fitted when additional data become available.

6.5 Comparison with published degradation relationships

The proposed relationships are controlled numerical trend relationships derived from FE models in which the material properties were held constant and corrosion was represented through pitted geometry. They therefore describe the geometric effect of pitting for the studied steel and should not be interpreted as independent experimental degradation laws.

Their use is limited by the low experimental corrosion range, specimen-to-specimen scatter, and the modelling assumptions adopted in this thesis. Only up to 2.49% gauge-section mass loss are Equations 6.4 to 6.6 fitted, and linear extrapolation to higher severities should be avoided. Beyond this range, the 4-12% projection study shows that the response becomes more nonlinear. The proposed relationships, accordingly, stand as preliminary engineering estimates rather than design equations.

6.6 Worked example, uncertainty and conditions of use

Although mass loss was used as the primary independent variable in the proposed residual-property relationships, it should not be interpreted as a complete descriptor of pitting corrosion. Mass loss defines the total volume of material removed, but it does not specify how that material loss is distributed through pit radius, depth, density, spacing, clustering or surface location. Therefore, stochastic realisations with the same mass loss may still produce different tensile responses, particularly in fracture strain and toughness, where local strain localisation is strongly influenced by pit morphology and spatial distribution.

The proposed relationships should therefore be interpreted as simplified mass-loss-based trend relationships within the assumptions of this study, rather than as general predictive equations for pitted steel. They provide a practical first-order estimate of the average FE response for the adopted cylindrical pit idealisation, selected pit-radius distribution, one-surface pitting assumption, fixed Day-0 material model, coupon geometry and investigated mass-loss range. The scatter around the fitted trends reflects the additional influence of pit morphology, which is not explicitly included as an independent variable in the equations.

To illustrate the intended use of the low-severity relationships, consider a coupon of the studied steel with a cleaned gauge-section mass loss of 2.00%. Since this value lies within the fitted range of $0 < \Delta m \leq 2.49\%$, the anchored relationships in Equations 6.4 to 6.6 may be applied directly:

$$R_\sigma = 1 - 0.0043(2.00) \approx 0.991$$
$$R_\varepsilon = 1 - 0.0485(2.00) \approx 0.903$$
$$R_U = 1 - 0.0597(2.00) \approx 0.881$$

This corresponds to an estimated strength reduction of approximately 0.9%, a fracture-strain reduction of approximately 9.7%, and a toughness reduction of approximately 11.9%. The interpretation is that, within the low-severity range, a strength-based assessment would indicate only limited degradation, whereas the deformation and energy-absorption measures show a clearer reduction.

The same relationships can also be inverted within the fitted range. For example, a 10% reduction in toughness corresponds to:

$$0.90 = 1 - 0.0597\Delta m$$
$$\Delta m \approx 1.67\%$$

Thus, within the fitted low-severity range, a toughness reduction of approximately 10% would be associated with a gauge-section mass loss of about 1.67%.

The use of these relationships is subject to the following conditions. For gauge-section mass losses in the range:

$$0 < \Delta m \leq 2.49\%$$

Equations 6.4 to 6.6 are the recommended low-severity trend relationships. For projected mass losses in the range:

$$4\% \leq \Delta m \leq 12\%$$

the direct projected FE results and associated trend interpretation should be used instead of linearly extrapolating the low-severity equations. The intermediate interval:

$$2.49\% < \Delta m < 4\%$$

is treated as a transition region because it lies between the experimentally matched range and the projected FE range. If an estimate is required within this interval, interpolation between the low-severity relationship at 2.49% and the 4% projected FE result may be used as an indicative transition estimate. However, additional FE simulations within this interval would be required for a more robust prediction.

Three sources of uncertainty should also be recognised in any use of the relationships. Least reliable is the strength relationship, since the change in UTS within the low-severity range is small and affected by morphology-induced scatter. Part of the physical interpretation of stochastic pitting, and not simply numerical noise, is what the scatter between random pit realisations represents. A mean trend estimate, rather than an exact value, is therefore how a single predicted value should be interpreted. Comparing relative changes between models analysed under the same numerical assumptions, rather than defining exact absolute fracture properties, is what fracture strain and toughness are most appropriately used for.

The studied low-carbon structural steel, the tested dog-bone coupon geometry, monotonic quasi-static tensile loading, and the single-face cylindrical pitting idealisation adopted in this thesis are the only conditions under which the relationships hold. Where a whole-coupon mass-loss percentage is reported, conversion to the exposed gauge-section basis must occur before the relationships can be applied.

7. Discussion

It provides a measurable basis for defining corrosion severity and for controlling the total removed volume in the finite-element models, but it does not describe how the lost material is distributed spatially. The same mass loss may be produced by many shallow pits, a smaller number of deeper pits, or a clustered pit field near a critical section, each of which can lead to different localisation behaviour.

The experimental programme showed that, within the measured corrosion range, the tensile properties remained strongly affected by specimen-to-specimen scatter. The numerical workflow was therefore used to isolate the geometric effect of pitting by keeping the material model constant and varying only the pitted geometry. This allowed the influence of pit distribution, mass loss, and projected corrosion severity to be examined more systematically than could be achieved from the experimental data alone.

Overall, the results indicate that early-stage pitting may have only a limited effect on ultimate tensile strength, while producing a clearer reduction in deformation capacity and toughness. At higher projected mass-loss levels, the reduction in tensile capacity becomes more pronounced, but the post-peak response remains strongly influenced by stochastic pit morphology.

7.1 Synthesis of Findings

The experimental and numerical results provide complementary information. The experimental results establish the physical corrosion context and show the level of scatter present in nominally similar coupons. Over the measured exposure range, the reduction in strength was not clearly separable from this scatter. This means that the experimental results alone support a cautious interpretation: at the achieved corrosion severities, the tensile strength degradation is small relative to the natural variability between specimens.

Although the Day-0 FE model showed very close agreement with the experimental ultimate tensile strength, the calibration was not assessed using UTS alone. The comparison also considered the overall stress–strain curve shape, including the elastic slope, yield region, strain-hardening response and fracture strain. The model captured the main tensile behaviour of the uncorroded coupon, particularly the post-yield hardening and peak stress response. Minor discrepancies in the yield and final fracture regions are considered acceptable because these parts of the response are more sensitive to experimental scatter, material idealisation, damage parameters and mesh effects. The Day-0 calibration was therefore judged suitable as a baseline fixed material model for the geometry-isolated corrosion simulations.

A controlled interpretation of the geometric effect of pitting is provided by the finite-element results. Only minor changes in UTS, but clearer reductions in fracture strain and toughness, were shown by the FE models for the Day 14 to Day 42 corrosion levels, corresponding to approximately 1.29-2.49% gauge-section mass loss. Deformation capacity, more strongly than peak load-carrying capacity, is affected by low-severity pitting, this supports.

Beyond the experimental range, this interpretation is extended by the projected 4-12% mass-loss simulations. The downward shift in tensile response becomes more evident in these models, and a substantial mean UTS reduction emerges at higher severity. The residual UTS factor falls to approximately 0.805 at 12% projected mass loss, a strength reduction of about 19.5% relative to the Day 0 FE baseline. Once corrosion severity exceeds the low experimental range, mass loss becomes a stronger global driver of strength degradation, this shows.

The perfectly monotonic sequence with mass loss, however, is not followed by fracture strain and toughness in the projected results either. Pit depth, spacing, clustering, and location relative to the eventual failure section all leave the post-peak response sensitive to the critical pit arrangement. Increasing mass loss strengthens the average degradation trend, then, but stochastic pit morphology continues to control localisation and scatter.

7.2 Mass Loss, Morphology and the Sufficiency of Descriptors

The results support two linked conclusions. First, UTS alone is not sufficient to describe corrosion damage. Within the experimentally matched FE range, UTS remains close to the Day 0 baseline, while fracture strain and toughness show clearer reductions. A strength-only assessment would therefore understate the mechanical consequence of pitting where deformation capacity or fracture resistance is important.

Second, mass loss alone is not sufficient to predict the full tensile response. The grouped FE comparisons show that models with the same target mass loss can still produce different fracture strains and toughness values because the pit field differs between realisations. Pit count alone is also insufficient. A larger number of pits does not necessarily produce the most severe response, since the same removed volume may be distributed across many smaller defects or concentrated into fewer deeper defects.

This justifies the use of a mass-loss-controlled stochastic pitting workflow. Mass loss provides the global severity measure, while the stochastic pit field introduces the morphology-induced variability that governs localisation. A uniform-thickness model would capture only the average section loss, while a deterministic single-pit model would miss the effect of random pit interaction. The present workflow therefore provides a more appropriate framework for examining how both total material loss and local defect arrangement affect tensile behaviour.

The SEM observations also support this interpretation qualitatively. The experimental pit population was more complex and finer than the idealised numerical pit population. The generated pits were not intended to reproduce the natural pit population one-to-one. Instead, SEM observations were used as qualitative guidance for selecting a physically reasonable idealised pit scale, while the quantitative link between experiment and model was made through removed volume and mass loss. This distinction is important: the FE model should be interpreted as a controlled morphology idealisation, not as a direct reconstruction of every observed pit.

7.3 Implications for Engineering Assessment

The results suggest that early-stage pitting corrosion should not be judged only by residual tensile strength. A steel coupon may retain most of its peak strength while already showing reduced deformation capacity and energy absorption. This is particularly relevant where ductility, redistribution capacity, or warning before fracture is important.

Mass loss remains useful because it is simple to measure and provides a consistent corrosion-severity scale. However, it should ideally be supplemented by a local morphology descriptor when fracture or ductility is of concern. Examples include maximum pit depth, local thickness loss, pit density, pit clustering, or the presence of severe pits near critical sections. Two specimens with the same mass loss should not automatically be assumed to have the same deformation capacity.

The predictive relationships proposed in Chapter 6 provide preliminary trend estimates for residual UTS, fracture strain, and toughness within the low-severity range. Their main value is not as design equations, but as a transparent way of showing the relative sensitivity of different tensile properties. Within the fitted range, fracture strain and toughness reduce much faster than UTS per unit mass loss. For the projected 4–12% range, the direct FE trends should be used instead of extending the low-severity linear equations.

The transition between the experimentally matched range and the projected range should also be treated carefully. The low-severity relationships are recommended up to 2.49% gauge-section mass loss, while the projected FE results begin at 4%. The intermediate interval between 2.49% and 4% should therefore be regarded as a transition region where interpolation may be used only as an indicative estimate. Additional FE simulations would be required for a more robust relationship in that interval.

7.4 Limitations

The conclusions of this thesis are bounded by several modelling and experimental limitations. These relate mainly to the idealised pit geometry, the one-face pitting assumption, the fixed material model, the treatment of fracture, the mesh sensitivity of post-peak quantities, and the coupon-scale scope of the work.

The finite-element workflow should be interpreted as a controlled numerical investigation into the effect of pitting and mass loss, rather than as an exact reproduction of the experimental corrosion exposure. The experimental immersion exposure allowed corrosion to develop on multiple exposed surfaces of the gauge section, whereas the FE model idealised the corrosion morphology on one main surface. The target volume loss was controlled so that the required mass-loss level was represented, but the model was not intended to reproduce the exact multi-surface corrosion morphology of each physical coupon.

Since the material model was kept constant across all corrosion levels, the differences between the uncorroded and pitted FE responses should be interpreted as the effect of geometric material loss only. The observed reductions in strength, fracture strain and toughness therefore result from the reduced net section and local strain concentration around the idealised pits, rather than from any assumed degradation of the steel constitutive behaviour.

All successful production FE simulations generated using the final adopted modelling workflow were included in the results. No completed production run was removed because of its strength, fracture strain, toughness, or degree of scatter. Preliminary simulations used during model development were excluded because they formed part of the calibration and diagnostic stage, including trials of plastic stress–strain input, damage parameters, mesh controls, and numerical stability. Runs that terminated due to excessive distortion or numerical instability were not treated as valid production cases. The conical-pit trials were excluded from the main interpretation because they did not provide a stable set of completed simulations.

7.4.1 Geometric Idealisation of Corrosion Pits

The production models used flat-bottomed cylindrical pits. This idealisation was selected because it provides robust volume control, repeatable pit insertion, and acceptable mesh quality. However, natural corrosion pits are irregular in plan and depth. They may have rounded or tapering profiles, variable wall angles, local roughness, and coalescence between neighbouring pits. The cylindrical idealisation therefore cannot reproduce the full morphology of naturally corroded surfaces.

The numerical pit population is also coarser than the natural pit population indicated by SEM observations. The model uses fewer, larger idealised pits to represent the same removed volume. This was a deliberate modelling choice driven by mesh feasibility. Resolving a very large number of small natural pits through a 2 mm coupon thickness in an explicit tensile-to-fracture analysis would require a much finer mesh and a substantially higher computational cost. Consequently, the quantitative link between experiment and model is made through removed volume and mass loss, rather than through exact pit count or one-to-one pit-size matching.

The cylindrical geometry may produce stronger local strain concentrations than smoother natural pits with the same removed volume. As a result, the absolute fracture strain and toughness values should be interpreted with caution. The main value of the cylindrical-pit results is in comparing relative trends between models generated using the same assumptions, rather than in predicting the exact fracture response of a specific corroded specimen.

7.4.2 Limited Comparison of Pit Shapes

Although alternative pit shapes were considered during workflow development, the final production study was limited to cylindrical pits. Conical-pit trials were numerically unstable and did not provide a reliable set of completed simulations. Therefore, the morphology effect quantified in this thesis refers to variation in pit size, depth, spacing, and spatial arrangement within the cylindrical-pit family, rather than to a full comparison between different pit shapes.

This means that the study does not resolve the relative effect of cylindrical, conical, semi-ellipsoidal, or irregular natural pit geometries. Future work should revisit this issue using improved meshing strategies, local refinement, or measured-surface-based models.

7.4.3 Fixed Material Properties and Experimental Scatter

The material model was calibrated using the uncorroded Day 0 response and then held as a constant for all corroded and projected simulations. This allowed the effect of corrosion geometry to be isolated. Any change in the predicted tensile response could therefore be attributed to pitting and material removal, rather than to assumed changes in the base steel properties.

This assumption also limits the scope of the model. The simulations do not include possible changes in material behaviour caused by corrosion-related microstructural effects, hydrogen effects, or surface embrittlement. The results should therefore be interpreted as geometry-only corrosion simulations. This applies both to the Day 14–42 models and to the projected 4–12% mass-loss models.

The experimental dataset also contains natural coupon-to-coupon scatter. At the measured mass-loss levels, the corrosion effect is small compared with this scatter, which limits the extent to which the experimental results can independently confirm the small FE-predicted reductions. The FE workflow therefore complements the experiment by isolating a geometric effect that is difficult to resolve experimentally at low severity.

7.4.4 Fracture Modelling and Mesh Dependence

The absolute fracture strain of the uncorroded coupon is over-predicted by the ductile-damage model with element deletion, and some mesh dependence in the fracture response is retained even where the predicted UTS has converged. Local damage models with element deletion carry this as a known limitation. The predicted fracture displacement can depend on element size, damage evolution parameters and the local mesh around the failure zone once damage initiates.

The absolute fracture strain predicted by the model is treated as indicative rather than exact for this reason. UTS and relative ductility trends are what the predictive relationships are framed primarily around. How the pitting changing the deformation response relative to the uncorroded baseline is what the model is considered reliable for identifying, not an exact fracture strain for a specific coupon.

A mesh-regularised or non-local damage formulation would reduce this dependence and improve the absolute prediction of fracture strain. Such an approach is beyond the scope of the present thesis but would be a useful refinement for future work.

7.4.5 Scope of Applicability

The study is limited to coupon-scale specimens under monotonic quasi-static tensile loading. Member-scale behaviour, cyclic loading, dynamic loading, welded details, residual stress, and structural boundary conditions are outside the scope of the work. The results should not be applied directly to full-scale members without additional assessment.

The experimental corrosion range is also limited. The maximum measured gauge-section mass loss was approximately 2.49%. The 4–12% cases are projected numerical studies, not experimentally verified corrosion states. They are useful for examining trends at higher severity, but they should not be interpreted as direct experimental predictions.

The applicability of the numerical results is therefore limited to cases where corrosion can be reasonably represented by equivalent material loss and idealised localised pitting. Multi-face pitting measured pit reconstruction, more complex pit morphology, and improved local meshing would be required before the method could be used for more specimen-specific or design-level predictions.

7.5 Engineering Implications and Positioning of the Workflow

The articles in the literature review are valuable because they provide the empirical basis for understanding corrosion damage. However, experimental results often include both geometric corrosion effects and possible material changes, and the two effects are difficult to separate.

There are also high-fidelity numerical models based on measured corrosion surfaces, such as laser scanning, micro-computed tomography or random-field surface descriptions [11], [12], [23]. These models can reproduce the residual strength and fracture location of specific specimens with greater geometric accuracy. Their limitation is that they are specimen-specific, time-consuming and less suitable for generating broad parametric trends.

Another category consists of idealised-pit numerical models. These models use simplified pit geometries to study how pit depth, aspect ratio, spacing and shape affect stress concentration and mechanical response [13]. They are useful for isolating individual geometric effects, but many such models do not represent the spatial randomness of a corroded surface and should be used as holistically in conjunction with other means of testing and verifications.

The workflow developed in this thesis sits between the high-fidelity surface-reconstruction approach and the idealised-pit approach. It uses parameterised cylindrical pits but places them as stochastic populations across the exposed gauge surface. It also links the generated pit volume directly to a measured mass loss. This gives the method two important advantages: it is reproducible, because each case is seed-controlled, and it is physically auditable, because the achieved mass loss can be checked against the target mass loss.

This positioning supports the two central arguments of the thesis. First, maximum stress alone is an incomplete descriptor of corrosion damage, because deformation capacity can reduce even when UTS remains almost unchanged. Second, mass loss alone is an incomplete predictor of tensile response, because the same total removed volume can produce different mechanical responses depending on where the pits are located and how they interact. The workflow demonstrates these points within one controlled modelling framework.

For engineering assessment, the implication is that corrosion should not be described only by a single average severity measure when ductility or fracture risk is important. A practical assessment should ideally include both an average severity descriptor, such as mass loss or mean thickness loss, and a local morphology descriptor, such as maximum pit depth, pit density or local thickness variation.

The results also indicate that early-stage corrosion may be underestimated by strength-based assessment alone. At the studied corrosion severities, UTS changes only slightly, whereas fracture strain and toughness reduce more clearly. Therefore, assessment criteria for corroded steel should consider residual ductility or toughness in addition to residual strength, particularly where redistribution capacity or warning before fracture is important.

8. Conclusions and Future Work

8.1 Conclusions

This thesis developed and applied a reproducible finite element workflow for studying the tensile response of structural steel coupons affected by pitting corrosion. The workflow was used together with an experimental programme to examine how corrosion severity and pit morphology influence ultimate tensile strength, deformation capacity and toughness. The main conclusions are as follows.

1. A reproducible stochastic pit-generation workflow was developed and implemented. The MATLAB generator creates non-overlapping random pit fields under defined geometric rules and scales the pit depths so that the total removed pit volume matches a target mass loss. The pit fields are seed-controlled and transferred into Abaqus through a scripted pit-cutting procedure. This provides a direct and auditable link between the target mass loss and the finite element pit geometry.

2. The uncorroded Day-0 finite element model provided a suitable baseline for the numerical study. The calibrated model reproduced the experimental Day-0 UTS to within approximately 0.4% and captured the overall baseline elastic and strain-hardening response. Mesh and quasi-static checks indicated that the pre-fracture response was not strongly controlled by numerical artefacts. A representative mass-scaling check from 1×10^{-4} to 1×10^{-6} showed that the pre-fracture load–displacement response was essentially unchanged.

3. The experimental corrosion results did not show a clear mechanical degradation trend within the studied mass-loss range. The maximum corrosion severity was approximately 2.49% when referenced to the exposed gauge-section mass. Within this range, the measured UTS, fracture strain and toughness were strongly affected by coupon-to-coupon scatter. The upward variation in some

experimental UTS values was therefore not interpreted as corrosion strengthening, but as material and testing scatter at low corrosion severity.

4. The geometry-only finite element results indicate that low-level pitting affects deformation capacity more clearly than peak tensile strength. With the material properties held constant, the pitted models showed only a weak and non-monotonic UTS response. The lowest group-mean UTS, obtained at Day 42, was approximately 1.8% lower than the uncorroded FE baseline. In contrast, the FE final strain and toughness decreased by approximately 11% and 14%, respectively. Within the adopted modelling assumptions, this suggests that low-level pitting is more clearly reflected through reduced deformation capacity and energy absorption than through reduced UTS.

5. Mass loss alone was not sufficient to fully describe the tensile response of pitted steel. At the same target mass loss, different random realisations produced different tensile responses because the local pit arrangement changed. The response was influenced by pit depth, spacing, clustering and the position of critical pits relative to the eventual localisation region. This supports the need to consider both average corrosion severity and local pit morphology, especially when deformation capacity or fracture-related response is important.

6. Provisional mass-loss-based trend relationships were developed to link residual tensile properties to corrosion severity. Using the gauge-section mass-loss basis, the fitted relationships suggest that deformation capacity and toughness are more sensitive to increasing mass loss than UTS within the studied numerical range. However, they are not design equations and were not independently checked against additional datasets.

7. A higher-severity numerical projection study extended the modelled range to 12% gauge-section mass loss in 2% increments, with four stochastic cylindrical-pit realisations at each level. In contrast to the near-flat response over the experimentally matched low-severity range, the projected UTS decreased more clearly with increasing mass loss, reaching approximately 19%

below the Day-0 finite-element baseline at 12% gauge-section mass loss. This suggests that the relationship of the low-severity strength response should not be extrapolated to higher corrosion severities. The projection results are numerical and geometry-based only, and should be interpreted within the adopted pit shape, material model, mesh and loading assumptions.

Overall, this thesis contributes a reproducible, seed-controlled and mass-loss-verified workflow for introducing stochastic pitting corrosion into tensile coupon finite-element models. For the low corrosion-severity range investigated experimentally, the geometric influence of pitting was not associated with a large or clearly monotonic reduction in peak tensile strength. The numerical results instead showed a clearer effect on strain localisation, deformation capacity and toughness.

8.2 Future work

The present study developed a reproducible workflow for linking measured mass loss, generated pit geometry and tensile response. The following future work is recommended to extend the scope of the method and strengthen its application to broader corrosion-assessment problems.

1) Additional steel grades, coupon geometries and exposure conditions should be tested using this workflow. The transferability of the proposed relationships could then be examined, showing whether the relative sensitivity of UTS, fracture strain and toughness observed in this study holds consistent across different materials and corrosion environments.
2) Multi-face pitting should be incorporated into the modelling framework in future work, allowing corrosion damage on opposing and adjacent surfaces to be represented more directly. Improved local meshing strategies would be required for this, such as adaptive refinement, partition-based meshing, submodelling or alternative element formulations, to preserve element quality around closely spaced pits and thin remaining ligaments. More realistic pit morphologies should also be considered in further development, including irregular pit profiles, measured surface topography, pit coalescence and spatially varying depth distributions.
3) Experimental validation at higher corrosion severity. The principal remaining need is experimental, namely tensile testing of more severely corroded coupons with much longer

exposure period to verify the projected higher-severity trends, since the projection holds the material card fixed and does not capture any corrosion-induced change in the bulk material. Two further numerical extensions are also recommended. Pit coalescence and strong pit interaction beyond the 12% range should be modelled, where a small number of severe defects rather than the average pit population may control the response. The corrosion severity at which the approximately linear low-severity relationships transition into the nonlinear higher-severity behaviour identified in Section 5.10 should also be defined more precisely.

4) Measured pit morphology should be integrated into future experimental programmes. Direct measurement of pit depth, pit width, pit density and local thickness variation before tensile testing would allow this. Such measurements could refine the stochastic pit generator and support comparison between alternative statistical descriptions of pit size, such as Gaussian, lognormal and Weibull distributions, thereby strengthening the link between generated pit fields and measured corrosion morphology.
5) A comparison between generated and reconstructed surface models would offer a useful extension. Three modelling approaches applied to the same corroded specimen could be compared: a uniform thickness-loss model, a generated stochastic pit model and a reconstructed surface model based on measured corrosion topography. This would quantify the additional accuracy gained by including detailed morphology information and would help determine whether the cylindrical pit idealisation provides a conservative representation of localised corrosion.
6) Controlled comparison of pit-shape idealisations. The robustness of non-cylindrical pit modelling should be improved so that cylindrical, conical, semi-ellipsoidal and hemispherical pits can be compared under matched mass-loss conditions. How pit shape influences strain localisation, fracture strain and toughness would be clarified by this comparison, placing the cylindrical idealisation used in this study within a broader modelling context.
7) The workflow should be extended from coupon-scale tensile models to larger structural components and more complex loading conditions, such as cyclic or combined loading. Mesh-regularised or non-local ductile-damage formulations could be investigated in parallel to improve the prediction of absolute fracture strain to connect the coupon-level findings to the assessment of real corroded steel structures.

References

[1] Y. Wang, C. Chang, S. Xu, and C. G. Soares, "Probabilistic constitutive model for corroded structural steel with stochastic pits under monotonic tension," *Engineering Structures*, vol. 304, p. 117599, Feb. 2024, doi: 10.1016/j.engstruct.2024.117599.

[2] R. Songbo, G. Ying, K. Chao, G. Song, X. Shanhua, and Y. Liqiong, "Effects of the corrosion pitting parameters on the mechanical properties of corroded steel," *Construction and Building Materials*, vol. 272, p. 121941, Dec. 2020, doi: 10.1016/j.conbuildmat.2020.121941.

[3] S. Zeng, S. Gu, S. Ren, Y. Gu, C. Kong, and L. Yang, "A Modeling Method for Finite Element Analysis of Corroded Steel Structures with Random Pitting Damage," *Buildings*, vol. 12, no. 11, p. 1793, Oct. 2022, doi: 10.3390/buildings12111793.

[4] Z. Guo *et al.*, "Contribution of spatially variable pitting corrosion on fatigue life prediction of RC beams," *Structures*, vol. 69, p. 107399, Oct. 2024, doi: 10.1016/j.istruc.2024.107399.

[5] M. Ghasemzadeh, M. Mokhtari, M. H. Bilgin, and A. Kefal, "Pitting corrosion identification approach based on inverse finite element method for marine structure applications," *Ocean Engineering*, vol. 273, p. 113953, Feb. 2023, doi: 10.1016/j.oceaneng.2023.113953.

[6] W. Zhang, Z. Long, and X. Liu, "A constitutive equation and numerical study on the tensile behavior of reinforcing steel under different mass loss ratios," *Materials*, vol. 18, no. 11, p. 2640, Jun. 2025, doi: 10.3390/ma18112640.

[7] M. Biglu, F. Von Bock Und Polach, and S. Ehlers, "Parametric finite element analysis of naturally corroded steel specimens using 3D surface laser scans," *Ships and Offshore Structures*, pp. 1–17, Apr. 2025, doi: 10.1080/17445302.2025.2492429.

[8] J. M. R. S. Appuhamy, T. Kaita, M. Ohga, and K. Fujii, "Prediction of residual strength of corroded tensile steel plates," *International Journal of Steel Structures*, vol. 11, no. 1, pp. 65–79, Mar. 2011, doi: 10.1007/s13296-011-1006-6.

[9] Z. Zhao, W. Wang, R. Yan, and B. Zhao, "Tensile capacity degradation of randomly corroded strands based on a refined numerical model," *Reliability Engineering & System Safety*, vol. 253, p. 110512, Sep. 2024, doi: 10.1016/j.ress.2024.110512.

[10] Z. Zhao, W. Wang, R. Yan, and B. Zhao, "Experimental and numerical investigations on tensile capacity of corroded strands," *Journal of Constructional Steel Research*, vol. 213, p. 108402, Dec. 2023, doi: 10.1016/j.jcsr.2023.108402.

[11] K. Woloszyk and Y. Garbatov, "An enhanced method in predicting tensile behaviour of corroded thick steel plate specimens by using random field approach," *Ocean Engineering*, vol. 213, p. 107803, Jul. 2020, doi: 10.1016/j.oceaneng.2020.107803.

[12] K. Woloszyk and Y. Garbatov, "Random field modelling of mechanical behaviour of corroded thin steel plate specimens," *Engineering Structures*, vol. 212, p. 110544, Mar. 2020, doi: 10.1016/j.engstruct.2020.110544.

[13] M. Cerit, K. Genel, and S. Eksi, “Numerical investigation on stress concentration of corrosion pit,” *Engineering Failure Analysis*, vol. 16, no. 7, pp. 2467–2472, Apr. 2009, doi: 10.1016/j.engfailanal.2009.04.004.

[14] X. Liang, J. Sheng, and K. Wang, “Investigation of the mechanical properties of steel plates with artificial pitting and the effects of mutual pitting on the stress concentration factor,” *Results in Physics*, vol. 14, p. 102520, Jul. 2019, doi: 10.1016/j.rinp.2019.102520.

[15] Y. Xu, “The Corrosion Characteristics and Tensile Behavior of Reinforcement under Coupled Carbonation and Static Loading,” *Materials*, vol. 8, no. 12, pp. 8561–8577, Dec. 2015, doi: 10.3390/ma8125479.

[16] R. Li, C. Miao, and J. Yu, “Effect of characteristic parameters of pitting on strength and stress concentration factor of cable steel wire,” *Construction and Building Materials*, vol. 240, p. 117915, Dec. 2019, doi: 10.1016/j.conbuildmat.2019.117915.

[17] R. Wang, S. Lin, and P. Dou, “Statistical constitutive model of steel in randomly pitted structures,” *Ocean Engineering*, vol. 243, p. 110211, Nov. 2021, doi: 10.1016/j.oceaneng.2021.110211.

[18] Y. Wang, X. Zhou, H. Wang, D. Kong, and S. Xu, “Stochastic constitutive model of structural steel based on random field of corrosion depth,” *Case Studies in Construction Materials*, vol. 16, p. e00972, Feb. 2022, doi: 10.1016/j.cscm.2022.e00972.

[19] W. Zhang, J. Chen, Q.-Q. Yu, Y. Jing, and A. Chang, “Stochastic modeling of corrosion evolution of steel plates under artificial marine atmosphere environment,” *Ocean Engineering*, vol. 310, p. 118565, Jul. 2024, doi: 10.1016/j.oceaneng.2024.118565.

[20] M. Xia, Y. Wang, and S. Xu, “Study on surface characteristics and stochastic model of corroded steel in neutral salt spray environment,” *Construction and Building Materials*, vol. 272, p. 121915, Dec. 2020, doi: 10.1016/j.conbuildmat.2020.121915.

[21] F. Caleyo, J. C. Velázquez, A. Valor, and J. M. Hallen, “Probability distribution of pitting corrosion depth and rate in underground pipelines: A Monte Carlo study,” *Corrosion Science*, vol. 51, no. 9, pp. 1925–1934, May 2009, doi: 10.1016/j.corsci.2009.05.019.

[22] ASTM International, “Standard Guide for Examination and Evaluation of Pitting Corrosion,” *ASTM G46-94 (Reapproved 2018)*, 2018.

[23] K. Van Gaalen, F. Gremse, F. Benn, P. E. McHugh, A. Kopp, and T. J. Vaughan, “Automated ex-situ detection of pitting corrosion and its effect on the mechanical integrity of rare earth magnesium alloy - WE43,” *Bioactive Materials*, vol. 8, pp. 545–558, Jul. 2021, doi: 10.1016/j.bioactmat.2021.06.024.

[24] W. Li, J. Fan, P. Huo, and Y. Zhang, “Analysis of collapse strength and life prediction of casings in formation water service environments,” *Materials*, vol. 18, no. 13, p. 2934, Jun. 2025, doi: 10.3390/ma18132934.

[25] M. Mokhtari, X. Wang, and J. Amdahl, “Numerical analysis of pit-to-crack transition under corrosion fatigue using a stochastic pit generation algorithm,” *arXiv (Cornell University)*, Jan. 2023, doi: 10.48550/arxiv.2301.06408.

[26] Dassault Systemes, *Getting Started with Abaqus*, Version 6.8.

Standards

[S1] International Organization for Standardization, *Metallic materials — Tensile testing — Part 1: Method of test at room temperature*, ISO 6892-1, Geneva, Switzerland, 2019.

[S2] ASTM International, *Standard Guide for Laboratory Immersion Corrosion Testing of Metals*, ASTM G31, West Conshohocken, PA, USA, 2021.

[S3] International Organization for Standardization, *Corrosion of metals and alloys — Removal of corrosion products from corrosion test specimens*, ISO 8407, Geneva, Switzerland, 2021.